

**SYNTHESIS, FORMATION MECHANISM AND CHARACTERIZATION OF
PEROXIDE HOMEMADE EXPLOSIVES**

by

Eduardo A. Espinosa-Fuentes

A dissertation submitted in partial fulfillment of the requirements for the degree of

DOCTOR OF PHILOSOPHY

in

Applied Chemistry

UNIVERSITY OF PUERTO RICO

MAYAGUEZ CAMPUS

Dec, 2013

Approved by:

Samuel P. Hernández-Rivera, Ph.D.
President, Graduate Committee

Date

Félix R. Román-Velázquez, Ph.D.
Member, Graduate Committee

Date

Nairmen Mina-Camilde, Ph.D.
Member, Graduate Committee

Date

Carmen A. Vega-Olivencia, Ph.D.
Member, Graduate Committee

Date

Jorge Almodovar Montanez, Ph.D.
Representative, Graduate Studies

Date

Rene S. Vieta-Rivera, Ph.D.
Chairperson of the Department

Date

ABSTRACT

An important consideration in the area of homemade explosives, which are made from household products, is that it is difficult to control their production and use in terrorist activities. Therefore, security and defense agencies are very interested in getting a handle on this persistent problem. All these contributions can assist directly or indirectly to control the production and use of these explosives materials and improve and expand their spectroscopy based detection, which has been an active area of research. Specifically, knowing their formation mechanism helps to find substances that can inhibit the formation of these explosives. On the other hand, the mass fragmentation pattern is useful in the unequivocal identification in the different ports, among others applications.

This scientific contribution describes a series of studies aimed to improving of homemade explosives (HME) synthesis, proposing of a mechanism for the uncatalyzed formation reaction of the most important HME: triacetone triperoxide, thermal characterization studies of HME, and other physical chemistry characterization studies including mass spectrometry, Raman spectroscopy and infrared spectroscopy. Specifically, it deals with:

(1) Proposing of a viable mechanism for cyclic acetone-peroxide (CAP) formation reaction based entirely on qualitative and quantitative experimental measurements and supported by density functional theory theoretical modeling of the proposed intermediates and transition states. The experimental and theoretical results demonstrated that the proposed mechanism for the uncatalyzed reaction of CAP formation occurs in three steps: monomer formation, polymerization of the 2-hydroperoxypropan-2-ol monomer and cyclization. The temporal decays of the spectroscopic intensities of the tentatively assigned main vibrational bands are in complete agreement with the mechanism proposed.

(2) A novel method to synthesize diacetone diperoxide (DADP) from acetone and hydrogen peroxide without the presence of a catalytic agent. Previously reported syntheses used toluene sulfonic and *m*-sulfonic acid as catalyst. DADP was prepared with a purity of 99.99%; the melting point range (128.5-134.5°C) consistently agreed with this value. The success of the procedure strictly depends on controlling the ratio between acetone and hydrogen peroxide as well as the temperature of the reaction mixture.

(3) Determination of sublimation enthalpies of homemade cyclic acetone-peroxide explosives and homemade amino-peroxide explosives using thermogravimetric analysis and Fourier Transform infrared spectroscopy grazing angle probe measurements. The proposed method is direct because, it results from fitting the mass loss rate constants $K_{\text{sub}}(T)$ vs. temperature without assuming values for associated constants. The enthalpy values obtained were comparable with previously reported values and values of the coefficients of determinations (R^2) of the fittings obtained were all above 0.999+, which have high level of acceptance.

(4) A simple method to isolate both D_3 and C_2 -TATP conformers, which consists of multiple recrystallization steps using different solvent and heating to boiling. Spectroscopic and physical measurements such as: Raman spectra, X-ray diffraction and melting points showed that both clear and opaque crystals are different conformations of TATP. An experimental value of the transition energy between both conformers was also found using the Raman shifts.

(5) Characterization of tetramethylene diperoxide dicarbamide (TMDD) compound was accomplished using DART-MS using ammonia vapor as gas dopant. The DART mass spectra of TMDD showed a strong ammonium adduct peak $[M-NH_4]^+$ at 254 m/z and a more intense protonated molecular mass $[M-H]^+$ at 237.084 m/z corroborating the identity of the sample analyzed. The DART-MS spectra of the TMDD isotopomers successfully corroborated the respective molecular tails.

RESUMEN

Una consideración importante en el área de los explosivos caseros, los cuales son hechos de productos domésticos, es que es muy difícil controlar su uso y producción para planes terroristas; por lo tanto las agencias de seguridad y defensa están muy interesadas en tomar el control absoluto en este problema persistente. Todas estas contribuciones científicas pueden ayudar de forma directa o indirecta en el control de la producción y uso de estos materiales explosivos para mejorar y expandir su detección basado en métodos instrumentales espectroscópicos, lo cual ha sido un activo en esta área de investigación. Específicamente, conocer su mecanismo de reacción ayuda a encontrar sustancias que puedan inhibir la formación de estos materiales energéticos. Por otro lado, los patrones de fragmentación son útiles para identificación inequívoca en puertos terrestres, aéreos y acuáticos, entre otras aplicaciones de gran utilidad en materia de seguridad.

Esta contribución científica describe una serie de estudios dirigidos al mejoramiento en la síntesis de los explosivos caseros (HME por siglas en inglés), proposición de un mecanismo de formación no-catalizada del HME más importante: triperóxido de triacetona, estudios de caracterización térmica y otros estudios de caracterización de HME, incluyendo espectrometría de masas, espectroscopia Raman y espectroscopia infrarroja. Específicamente trata de:

(1) La proposición de un mecanismo viable para la reacción de formación de explosivos cíclicos peroxílicos (CAP, por siglas en inglés) basado completamente en mediciones experimentales cuantitativas y cualitativas y apoyado por el modelaje teórico de teoría de densidad funcional de los intermediarios y estados de transición propuestos. Los resultados demostraron que el mecanismo propuesto para la reacción no catalizada ocurre en tres pasos fundamentales, los cuales son: formación del monómero cuyo nombre científico es 2-hidroperoxipropan-2-ol, polimerización del monómero y ciclación de precursores principales. Los decaimientos temporales de las intensidades de las principales bandas vibracionales tentativamente asignadas están en completo acuerdo con el mecanismo propuesto.

(2) Un nuevo método para sintetizar DADP cerca del 100% de pureza sin el uso de catalizadores ácido base. La ruta sintética de alta pureza pueda ser usada en la preparación de estándares espectrométricos y cromatográficos, para estudios de caracterización, bioensayos entre otros. Síntesis reportadas previamente usan ácido tolueno sulfónico y ácido *m*-sulfónico

como catalizador. El éxito de procedimiento postulado depende de controlar la radio entre los precursores acetona y peróxido de hidrogeno así como de la temperatura de la mezcla reactiva.

(3) Determinación de las entalpias de sublimación de explosivos caseros aceto-peroxílicos (DADP and TATP) y amino-peroxílicos (HMTD and TMDD) usando análisis termogravimétrico (TGA) y espectroscopia infrarroja sobre superficies (FT-IR GA). El método propuesto es directo porque resulta de modelar directamente las constantes de sublimación o pérdida de masa versus temperatura sin asumir constantes arbitrariamente. Los valores de la entalpias fueron comparables con los reportados previamente y los valores de los R cuadrados resultaron estar sobre 0.999, lo cual es un alto nivel de aceptabilidad.

(4) Un método sencillo para aislar los conformeros D₃-TATP y C₂-TATP. Este método consiste en múltiples recristalizaciones con solventes de diferentes polaridades y calentado hasta ebullición. Las mediciones espectroscópicas y de constantes físicas tales como: Raman, difracción de rayos X y puntos de fusión mostraron que los cristales opacos y claros corresponden a cada una de las conformaciones citadas. También se pudo establecer un valor experimental para la barrera energética de la transición usando los desplazamientos del espectro Raman.

(5) Caracterización del compuesto tetrametileno diperoxido dicarbamida (TMDD) por espectrometría de masas directo en tiempo real y usando amonio como gas dopante. El espectro de masas DART mostró un pico fuerte correspondiente al ion aducto molecular $[M-NH_4]^+$ at 254 m/z y un pico base correspondiente ion molecular $[M-H]^+$ at 237.084 m/z corroborando la identidad de las muestras analizadas. Los espectros DART de los isotopomeros enriquecidos con nitrógeno 15 y carbono 13 mostraron coherencia con los distintos residuos moleculares iónicos.

Dedicated to
God, my wife Yorley, Sons Yoryed and
Oliver, and my parents Gladys and José

*Copyright © by
Eduardo A. Espinosa-Fuentes
2013*

ACKNOWLEDGEMENTS

First all thanks to GOD and My Family.

Thanks to: Dr. Samuel P. Hernández-Rivera for his guidance, and for giving me the opportunity to be part of his excellent graduate team.

To Dr. Ricardo Vivas-Reyes for his support in the theoretical part.

To the University of Puerto Rico-Mayaguez for giving me the opportunity to accomplish graduate studies.

To my lab-partners and the graduate committee for their help and important feedbacks.

To the graduate committee for unconditional support in the present thesis.

This contribution was supported by the U.S. Department of Defense, Agreement Number: W911NF-11-1-0152. The authors also acknowledge contributions from Dr. Richard T. Hammond from Army Research Office, DOD. Support from the U.S. Department of Homeland Security under Award Number **2008-ST-061-ED0001** is also acknowledged. However, the views and conclusions contained in this document are those of the authors and should not be considered a representation of the official policies, either expressed or implied, of the U.S. DHS.

TABLE OF CONTENTS

LIST OF TABLES	xi
LIST OF SCHEMES	xii
LIST OF FIGURES	xiii
LIST OF ABBREVIATIONS	xvii
1. INTRODUCTION	1
1.1 GENERAL ASPECTS	1
1.2 PREVIOUS WORK	2
1.3 MOLECULES STUDIED	4
2. A MECHANISM FOR UNCATALYZED ACETONE-PEROXIDE FORMATION REACTION: AN EXPERIMENTAL AND COMPUTATIONAL STUDY	7
2.1 EXPERIMENTAL SETUP	7
2.1.1 Reagents	7
2.1.2 Experimental Details	8
2.1.3 Equipment and Spectral Conditions	9
2.1.4 Density Functional Theory Calculations	10
2.2 RESULTS AND DISCUSSION	11
2.2.1 Description of the CAP formation Mechanism	11
2.2.2 Monomer Formation Step	13
2.2.3 Theoretical Support of the Monomer Formation Step	19
2.2.4 Polymerization Step	20
2.2.5 Theoretical Support of the HPC Steps	23
2.2.6 Cyclization Step and Total kinetic	25
2.2.7 Evidence of Some Intermediates Structures	27
2.2.8 A test of the CAP-mechanism with T-alcohols	30
2.3 CONCLUSIONS	34
3. NOVEL UNCATALYZED SYNTHESIS AND CHARACTERIZATION OF DIACETONE DIPEROXIDE (DADP)	35
3.1 EXPERIMENTAL DETAILS	35
3.1.1 Reagents	35
3.1.2 Procedure	36
3.1.3 Instrumentation	36
3.2 RESULTS AND DISCUSSION	37
3.2.1 Raman and FT-IR Results	41
3.2.2 ¹ H-NMR, ¹³ C-NMR and COSY-NMR Results	42
3.2.3 Direct Analysis in Real Time (DART TM) Mass Results	44
3.2.4 DSC Results	45
3.2.5 Theoretical Analysis	47
3.3 CONCLUSIONS	49
4. THERMAL PROFILE OF HOMEMADE PEROXIDE EXPLOSIVES	50
4.1 THEORETICAL BACKGROUND	50

4.2	EXPERIMENTAL SETUP	51
4.2.1	Reagents	51
4.2.2	Thermal gravimetric analysis (TGA) Measurements	52
4.2.3	FT-IR Grazing Angle Measurements (FT-IR-GA)	52
4.3	RESULTS AND DISCUSSION	53
4.3.1	Thermal Profile of HME Compounds	55
4.3.2	Thermal Profile of HAMPE Compounds	59
4.4	CONCLUSIONS	64
5.	SPECTROSCOPIC AND PHYSICAL EVIDENCE OF ISOLATED D₃-TATP AND C₂-TATP CONFORMERS	65
5.1	EXPERIMENTAL SETUP	65
5.1.1	Reagents	65
5.1.2	Instrumentation	65
5.1.3	Synthesis Details	66
5.2	RESULTS AND DISCUSSION	67
5.2.1	Raman and Computational Results	68
5.2.2	X-Ray diffraction (XRD) Results	74
5.2.3	Differential Scanning Calorimeter (DSC) Results	76
5.3	CONCLUSIONS	77
6.	ANALYSIS OF TETRAMETHYLENE DIPEROXIDE DICARBAMIDE (TMDD) BY DIRECT ANALYSIS IN REAL TIME-MASS SPECTROMETRY	78
6.1	EXPERIMENTAL SETUP	78
6.1.1	Reagents	78
6.1.2	Synthesis	79
6.1.3	Equipment and DART-MS Optimization	79
6.2	RESULTS AND DISCUSSION	80
6.2.3	DART-MS Fragmentation Pattern	80
6.3	CONCLUSIONS	91
7.	ACOMPLISHMENTS AND SCIENTIFIC CONTRIBUTIONS	92
	REFERENCES	92
	APPENDIX-B	112
	APPENDIX-C	115

LIST OF TABLES

Table	Page
Table 1-1. Systematic and common names of the homemade explosives studied.....	5
Table 2-1. Fractional times for different kinetics orders and quotient of fractional times for Acetone and new band decaying.....	22
Table 2-2. Constant rate and Activation Energy for all possible reaction, calculated at DFT level using B3LYP hybrid functional and 6-311g++(d, p) basis set [15]. -- Not calculated.....	22
Table 2-3. Mulliken atomic and NBO charges of hydroperoxyl and alkoxy oxygen atoms of the terminal groups calculated at DFT level using B3LYP hybrid functional and 6-311g++(d, p) basis set. P ₁ , P ₂ , and P ₃ are polymeric structures.....	24
Table 2-4. ¹ H-NMR and ¹³ C-NMR shifts of the reaction mixture in D ₂ O and acetone-d ₆ deuterated solvent.	28
Table 4-1 Sublimation enthalpy of standard nonexplosive compounds at 298.15K. These values were determined considering a linear and nonlinear fitting. Benzoic and <i>m</i> -Nitrobenzoic acid showed a well defined linear trend.....	55
Table 4-2 Sublimation enthalpy of the homemade peroxide explosives at 298.15K. These values were determined considering a nonlinear fitting. --- Not calculated.....	59
Table 6-1 Fragments list of the [TMDD- ¹⁵ N ₄ -NH ₄] ⁺ , [TMDD- ¹³ C ₂ -NH ₄] ⁺ and [TMDD-NH ₄] ⁺ adducts. --- Values don't found.	83

LIST OF SCHEMES

Scheme	Page
Scheme 2-1 Acetone and hydrogen peroxide molecules start interacting at close range by forming a hydrogen bond. This process is very fast and is not included in overall mechanism proposed. First step: monomer formation from intermediary or transition state (TS). Monomer is designed as P ₁ : (2-hydroperoxi, 2-propan-2-ol).....	12
Scheme 2-2 Second step: alkoxy-peroxyl condensation reaction: general scheme for polymerization step.....	12
Scheme 2-3 Dimerization between two P ₁ molecules and formation of P ₂ dimer: (2-[(2-hydroperoxy propan-2-yl) peroxy] propan-2-ol).....	12
Scheme 2-4 Formation reaction of P ₃ (an alkoxy-peroxyl condensation reaction) from P ₂ and P ₁ reacting molecules (trimerization). Trimer is designed as P ₃ (2-({2-[2-hydroperoxy propan-2-yl] peroxy] propan-2-yl} propan-2-ol).....	12
Scheme 2-5 Postulation of details of polymerization step: bonds broken and formed. based on density charges of the terminal oxygen atoms.....	13
Scheme 2-6 Alkoxy-peroxyl cyclocondensation reaction of P ₂ : formation reaction of C ₂ . This cyclic acetone peroxide product is identified as 3, 3, 6, 6-tetramethyl-1, 2, 4, 5-cyclotetroxane or diacetone diperoxide (DADP).....	13
Scheme 2-7 Alkoxy-peroxyl cyclocondensation reaction of P ₃ : formation reaction of C ₃ . This cyclic acetone peroxide product is 3,3,6,6,9,9-hexamethyl-1,2,4,5,7,8 hexoxonane or triacetone triperoxide (TATP).....	13
Scheme 2-8 Competitive inhibition reaction of AP formation with tert-alcohols, these compounds clearly stops AP-formation.....	31
Scheme 3-1 Structures of: (a) General view of DADP formation reaction. This is a two-step reaction: P ₁ -formation (liquid-phase reaction) and DADP-formation (gas-phase reaction); (b) P ₁ precursor of cyclic acetone peroxide dimer (C ₁ , DADP); (c) P ₂ precursor of cyclic acetone peroxide trimer (C ₂ , TATP)	39
Scheme 6-1 Synthetic pathway of TMDD compound. The TMDD- ¹⁵ N ₄ and TMDD- ¹³ C ₂ isotopomer were synthesized from urea- ¹⁵ N ₂ and urea- ¹³ C ₂ respectively.....	79

LIST OF FIGURES

Figure	Page
Figure 1-1 Optimized structures of the homemade explosives studied. a) TATP, b) DADP, c) HMTD, and d) TMDD.....	6
Figure 2-1 (a) Close up view of experimental setup for Raman Spectroscopy daily measurements. (b) Experimental setup for Raman spectroscopy kinetics measurements.....	9
Figure 2-2 (a)Variation of C=O Raman shift location due to the hydrogen bonding formation from normal range of 1690-1740 cm^{-1} to 1600-1700 cm^{-1} . (b) Variation of CH_3 Raman shift due to the hydrogen bonding formation from of 2923 cm^{-1} to 2927 cm^{-1} and formation of a new band corresponding to the first product (P_1 monomer)..	15
Figure 2-3 Variation of Raman shift location during a kinetic run. No significant difference between the starting and acetone spectra is observed.....	16
Figure 2-4 Energy diagram and sequence of atomic movements in the first step at DFT level (B3LYP/6-311++g(d,p)): The atomic motion sequences were: Initial nucleophilic attack of lone electron pair of carbonyl Oxygen atom of acetone to peroxide H atom. The formation of a new O-H bond and decreasing of C=O bond order. Quick interaction between the peroxy oxygen atom and the carbonyl carbon atom. Finally, the formation of new C-O bond is accomplished.....	19
Figure 2-5 (a) O-O-C-O reference plane on which, the charge distribution was sketched (b) Molecular electrostatic potential (MEP) contour map of the O-O-C-O plane: A cross section of the electrostatic spatial distribution at DFT level and B3LYP/6-311++g(d, p) basis set. This picture clearly shows that hydroxyl oxygen atom is the point more suitable for an electrophilic attack.....	24
Figure 2-6 Second-order decay of the new band at 540 cm^{-1} for an uncatalyzed reaction.....	21
Figure 2-7 First-order decay of the C=O---H band intensity for an uncatalyzed reaction.....	17
Figure 2-8 First order decay of the TATP non-overlapping band at 940 cm^{-1} for the uncatalyzed reaction.....	26
Figure 2-9 Intensity decay of $\nu_{\text{C=O}}$ band during a kinetics run of a catalyzed AP-reaction.....	18
Figure 2-10 Intensity decay of others band during a kinetics run of a catalyzed AP-reaction.....	18
Figure 2-11 Electron impact ms-spectrum of P_1 structure; monomer of the proposed mechanism. Molecular weight of this structure is 92g/mol.....	29

Figure 2-12 Gas chromatograph-electron impact mass spectrum of the gas phase AP formation reaction. The two main peaks at 0.86 min and 2.20 min are related to acetone and P ₂ , respectively.....	30
Figure 2-13 Temporal decay of $\nu_{C=O}$ band of the Raman spectra in an AP acid catalyzed reaction and decay of $\nu_{C=O}$ band in an AP-reaction when the t-alcohol is added.	32
Figure 2-14 (a) Visual view of Acetone-Peroxide T-butyl Alcohol Reaction at 5:1, 4:1, 3:1, 2:1 and 1:1 T-butyl Alcohol: acetone ratio. The precipitated TATP is proportional to alcohol amount (b) Acid catalyzed AP-reaction and AP-reaction plus T-alcohol.	32
Figure 2-15 Acetone, T-butyl Alcohol and Acetone-Peroxide-T-butyl Alcohol Mix Raman spectra, the disappearing of (R) ₃ C-OH band is clearly observed, at 900 cm ⁻¹ . The spectra were followed using a 532nm laser line.	33
Figure 2-16 Acetone, T-pentyl Alcohol and Acetone-Peroxide-T-pentyl Alcohol Mix Raman spectra, the disappearing of R ₃ C-OH band and appearing of (HO)C-O(OR) is clearly observed, at 910 cm ⁻¹ and 940 cm ⁻¹ respectively. The spectra were followed using a 514nm laser line.	33
Figure 3-1 Structures of: (a) General view of DADP formation reaction. This is a two-step reaction: P ₁ -formation (liquid-phase reaction) and DADP-formation (gas-phase reaction); (b) P ₁ precursor of cyclic acetone peroxide dimer (C ₁ , DADP); (c) P ₂ precursor of cyclic acetone peroxide trimer (C ₂ , TATP).....	39
Figure 3-2 (a) Gas chromatograph and electron impact mass spectrum of a sample of the gas phase were the DADP formation reaction takes place. The two main peaks at 0.86 min and 2.2 min are related to acetone and P ₁ , respectively. (b) Positive-ion DART™ mass spectrum of an isolated crystal assumed to be DADP. Ammonium hydroxide headspace vapor provided a source of NH ₄ ⁺ to form ammonium adducts in a He gas stream used for open air chemical ionization MS.....	40
Figure 3-3 GC-analysis of the uncatalyzed and catalyzed method. The uncatalyzed is a cleaner chromatogram compared to catalyzed one.....	41
Figure 3-4 (a) Raman spectra of DADP and TATP in the fingerprint region, at a 514 nm excitation line; (b) FT-IR spectra of DADP and TATP.....	42
Figure 3-5 (a) ¹ H-NMR and COSY-NMR spectra of DADP in CDCl ₃ ; (b) ¹³ C-NMR spectrum of DADP in CDCl ₃ solvent.	44
Figure 3-6 DSC thermogram of 5.0 mg of isolated crystals of DADP, at a scan rate of 5 °C/min, using (a) non-hermetically sealed pan and (b) hermetically sealed pan.....	46

Figure 3-7 FT-IR spectra of DADP gas at 170°C and DADP partial decomposition at 250°C compared to (a) DADP solid and (b) acetone.....	47
Figure 4-2 Non-linear thermal fitting of the experimental data for: (a) Benzoic acid and (b) Acetylsalicylic acid (ASA) Temperature range: 60-100°C. Temperature step: 1°C/point.	54
Figure 4-3 Non-linear thermal fitting of the experimental data for DADP using: (a) TGA and (b) FT-IR GA. Temperature range: 60-100°C. Temperature step: 1°C/point.	57
Figure 4-4 Non-linear thermal fitting of the experimental data for TATP using: (a) TGA and (b) FT-IR GA. Temperature range: 40-80°C. Temperature step: 1°C/point.	58
Figure 4-5 Non-linear thermal fitting of the experimental data for: (a) TMDD and (b) HMTD using TGA. Temperature range: 60-100°C. Temperature step: 1°C/point.....	61
Figure 4-6 FT-IR spectra of the solid and vapor phases of: (a) TMDD, (b) HMTD, (c) DADP and (d) TATP. The vapor phase sample was taken at the temperature range studied.	63
Figure 5-1 Microscopic picture of the: (a) square clear crystal, (b) needle clear crystal (D ₃ -TATP structure) and (c) opaque crystal (C ₂ -TATP conformer) at 10X.	67
Figure 5-2 Optimized structure and a cross section of the electrostatic spatial distribution (MEP) of the gem-methyl groups illustrating the chemical environment of: a) C ₂ -TATP and b) D ₃ -TATP at DFT level and B3LYP/6-311++g (d, p) basis set.	70
Figure 5-3 Raman spectra of clear square and opaque amorphous TATP crystals at (a) rings modes, (b) 200-450 cm ⁻¹ range, (c) CCOO shearing. (d) ν _{O-O} vibrations and (e) at ν _{C-H} stretching spectral range. Laser line 785nm.....	71
Figure 5-4 (a) ¹ H-NMR and (b) ¹³ C-NMR spectra of TATP solution of both conformers in CD ₃ Cl.....	72
Figure 5-5 Raman spectra of: A-TATP-3, 6, 9- ¹³ C ₃ , B-TATP-3', 3', 6', 6', 9', 9'- ¹³ C ₆ and C-TATP compounds. The unshifted band at 867 cm ⁻¹ corresponds to the peroxide stretch.....	73
Figure 5-6 XRD Diffractogram of both D ₃ and C ₂ -TATP conformers. In powder mode. X-ray source: CuKα at 44kV/40mA. Data was collected using a Goniometer Ultima θ-θ gonio.	75
Figure 5-7 DSC thermogram of: crystal mix, clear and opaque crystals of TATP at 5°C/min.	76

Figure 6-2 Positive-ion DARTTM mass spectrum of: (a) TMDD, (b) TMDD-¹³C₂ and (c) TMDD-¹⁵N₄ isotopomer. Ammonium hydroxide headspace vapor provided a source of NH₄⁺ to form ammonium adducts in a He gas stream used for open air chemical ionization MS. The DART gas temperature was tested at 250, 350, 450 and 500 °C. The 450 and 500 °C showed the best results for producing an [M-NH₄]⁺ signal.82

Figure 6-3 Higher symmetry structures of TMDD exhibiting the possible intra-hydrogen bonding that may cause the ring breaking to form the residues at 118 and 119 m/z. 84

Figure 6-4 TMDD structure forming multiple hydrogen bonding with ammonium ion. These atomic movements also show the high flexibility of the ring. Several form of the [TMDD-NH₄]⁺ adduct.85

Figure 6-5 (a) Overall fragmentation pattern of [TMDD-H]⁺ adduct considering breaking of C-N and O-O bonds. The electronic pair of the C-H and O-O bonds breaking is used to form the new C=N and N-H bonds. **(b)** Fragmentation pattern of [TMDD-H]⁺ adduct considering breaking of C-O and O-O bonds. The electronic deficiency of carbonyl and methylene carbon atom is balanced by the electronic pair of the nitrogen atoms. The proton atoms are provided by ammonium ion molecule or atmospheric molecules. In general, the cleavages of the heteroatomic bonds are promoted by hydrogen bonding. The electronic pair of the C-H and O-O bonds breaking is used to form the new carbonyl (C=O) and C-O bonds. The blue, green and yellow shaded area correspond to the water loss, C-N and O-O break respectively.90

Figure 6-6 Energy diagram and sequence of atomic movements in the: **(a)** [TMDD-H]⁺ adduct formation reaction, **(b)** [C₃H₇O₃N₂]⁺ adduct formation and **(c)** breaking of O-O bond catalyzed by ammonium ion at Hartree-Fock level of theory and B3LYP/6-311++g (d, p) basis set. First, it were calculated the transitions states, if a TS is found. Then an intrinsic reaction coordinate (IRC) calculation is carried out in order to connect both states: reagents and probable products. The IRC was followed in forward mode only.86

LIST OF ABBREVIATIONS

<i>NS</i>	number of transients in a NMR measurements
<i>AQ</i>	acquisition time
<i>SWH</i>	spectral width
<i>ST</i>	transition state
<i>B3LYP</i>	Becker-Lee-Yang-Parr
<i>DFT</i>	density functional theory
<i>MEP</i>	potential energy map
<i>DSC</i>	differential scanning calorimeter
<i>TGA</i>	thermogravimetry analysis
<i>DART-MS</i>	Direct Analysis in Real Time® mass spectrometry
<i>COSY-NMR</i>	nuclear magnetic correlation spectroscopy
<i>FT-IR GA</i>	fourier transformed infrared with grazing angle
<i>GC-MS</i>	gas chromatography mass spectrometry
<i>HPLC-MS</i>	high performance liquid chromatography mass spectrometry
<i>LC-MS</i>	liquid chromatography mass spectrometry
<i>HAMPE</i>	homemade amino peroxide explosive
<i>HAPE</i>	homemade acetone peroxide explosive
ΔC_p	heat capacity change
<i>FCC</i>	face center cubic
<i>BCC</i>	body center cubic
<i>XRD</i>	X-ray diffractogram
<i>HME</i>	homemade explosives
<i>TATP</i>	triacetone triperoxide
<i>DADP</i>	diacetone diperoxide
<i>TMDD</i>	tetramethylene diperoxide
<i>HMTD</i>	hexamethylene triperoxide diamine
<i>HPC</i>	hydroperoxyl condensation reaction

Chapter 1

1. INTRODUCTION

1.1 GENERAL ASPECTS

The reaction between acetone and hydrogen peroxide results in the formation of cyclic peroxides collectively called as cyclic acetone peroxides (CAP). The first cyclic structure formed is DADP, but the polymerization continues to form the trimer product of cyclization: triacetone triperoxide (TATP) and even the cyclic tetramer, although in very small amounts [1]. The most famous of these CAP is the cyclotrimer or TATP [2]. This compound is a highly unstable explosive and has been used persistently in terrorist attacks around the world. In addition, it was chosen as a detonator by the "shoe bomber" Richard Reid in 2001 [3-5]. TATP is as powerful as ordinary military explosives, such as 2,4,6-trinitrotoluene (TNT), hexahydro-1,3,5-trinitro-1,3,5-triazine (RDX) and pentaerythritol tetranitrate (PETN). However, it is one of the most sensitive explosives known, being extremely sensitive to impact, heat and friction [6-7]. DADP is also classified as a highly unstable homemade explosive (HME) sharing many of its properties with TATP, including its structure. It is also extremely sensitive to the impact and friction [2]. Many researchers have proposed reaction mechanisms for the formation of cyclic acetone peroxide products, agreeing that triacetone triperoxide (TATP) is the main reaction product.

Although DADP does not share the wide spread use of TATP, its study is well justified from fundamental viewpoint, since it is the first stable cyclic moiety formed in low proportions in the important acetone-peroxide reaction [8-9]. One way of preparing DADP in high proportions is by acid-catalyzed isomerization of TATP in organic solvents, dissolving TATP with a catalytic amount of *p*-toluenesulfonic acid in either chloroform or dichloromethane and then allowing the solution to stand at room temperature for one week leads to the formation of

the acetone peroxide dimer. Next, the resulting crystals are collected by recrystallization using hot methanol [5]. An alternative procedure involves the slow addition of hydrogen peroxide (30%) to a cold (-5°C), stirred mixture of acetone and catalytic *m*-sulfonic acid in dichloromethane.

An important consideration in the area of HME preparations is the fact that some of them can be prepared using household or costumer products. Thus, their production and use is extremely difficult to control by security enforcing authorities. As a result, these agencies are highly interested in gaining more control over HME production and use. Information about reaction pathways helps improve two important security aspects. The first, deals with the possibility of inhibiting the formation of HME by adding interfering agents. The second, has to do with devising new methods of forensic analysis that may assist in tracing energetic materials to the perpetrators. Another advantage of elucidating reaction mechanisms is that it could lead to the possibility of substituting household chemicals with passive equivalents that may inhibit the formation of HMEs. The analysis and detection of TATP and other HMEs has increased in recent years. This is motivated in part by the increased use of TATP and other cyclic organic peroxides in terrorist activities [3-5].

1.2 PREVIOUS WORK

Many groups have studied the preparation and characterization of HME as well as possible methods to improve its detection. In 2008, Jensen et al. [10] proposed a mechanism for acetone-peroxide reaction based on Raman and x-ray diffraction measurements, in that research the author doesn't report a relationship between the proposed mechanism and the experimental results. They also assigned the vibrational spectrum of TATP. Matyas and Pachman [9] studied the spontaneous transformation of TATP to DADP using sulfuric, perchloric and

methanesulfonic acid as catalysts; they also reported some physical constants of these compounds. Oxley et al. [11] made a comparative vibrational study of the different peroxide based explosives (TATP, TMDD and HMTD) commonly used by terrorists. This study consisted in the vibrational assignment by comparison of the theoretical harmonic spectra with the respective experimental spectra. Later that year, Armitt, Zimmermann and Ellis [12] analyzed the degradation products of TATP using Gas Chromatography-Mass Spectrometry (GC-MS). They found out that metal ions and salts can also degrade TATP and other peroxides. In 2007, Terent'ev et al. reported a new method to prepare 1,2,4,5,7,8-hexaoxonanes from the reaction of 1,1'-dihydroperoxydicycloalkyl peroxides with acetals and enols catalyzed by Lewis acids. This method allowed the synthesis of new compounds of the type described obtaining higher yields and selectivity. They found that alkoxy-peroxide reactivity is higher than acetone peroxide reactivity. The aim of this research was to propose a viable mechanism for acetone-peroxide formation reaction based entirely on qualitative and quantitative Raman and NMR spectroscopy measurements and supported by DFT theoretical modeling of the proposed intermediate and transition states [13]. Hiyoshi and Nakamura [7] studied the thermal decomposition of HMTD and TATP as functions of temperature and pressure using T-jump/FT-IR spectroscopy. They found that the decomposition products of TATP are dependent of the surrounding media by suggesting that TATP decomposes in gas phase, while HMTD decomposition products are independent by implying that HMTD decomposes previously in condensed phase.

In 2005, Denekamp et al. demonstrated that TATP has two separable conformers and that they coexist at ambient temperature, because the barrier for interconversion between them is relatively high at ambient temperature. They found that an energy barrier of $26.3 \text{ Kcal.mol}^{-1}$ (theoretical result) exists between these two conformers, and that the interconversion process occurs through a flip-flop movement of one of three oxygen atom pairs [14].

In 2003 and 2004, Muller and Dubnikova [5, 15] demonstrated that TATP exhibits two distinctive peaks with the same mass in both GC/MS and HPLC/MS analyses. They reported that the D₃-TATP conformation is the most stable and the energy difference is only 1.85 Kcal.mol⁻¹. It should be noted that above results are DFT theoretical. Previously, in 2002 Widmer et al. [16] had proposed that these two peaks correspond to the D₃ and C₂ conformers of TATP. Others researcher as Peña et al. [17] worked extensively on the differentiation and characterization of HEM (including TATP, DADP, HMTD and TMDD) by Direct Analysis in Real Time® (DART) TOF/MS. In 2000, Oxley et al. [18] analyzed the electron impact (EI) mass spectra of unlabeled and isotopically labeled hexamethylene triperoxide diamine.

In general terms, these substances have been reported extensively in all type of study; in many cases are isolated theoretical or experimental studies. In this manuscript, we are reporting experimental research theoretically-supported with quantum theory and/or other experimental techniques highly accurate.

1.3 MOLECULES STUDIED

All molecules studied in these investigations were highly energetic compounds. They are commonly named as HMEs because their precursors are mainly household or domestic products. These compounds pertain to the peroxide family of organic explosives. HMEs can be easily synthesized, but caution must be employed in doing so due to the high exothermic value of the formation reaction. Other concerns of handling the HME are sensibility to high temperatures and friction. The detection of HMEs has been achieved by techniques such as Raman, gas chromatography, mass spectroscopy, liquid chromatography and others. UV absorption based methods are not candidates for detection because the molecule lacks a chromophore group on its

structure. Table 1-1 summarizes the most probable structure, systematic and common names of these explosives compounds.

Table 1-1. Systematic and common names of the homemade explosives studied

Common name	Systematic Name
TATP -Triacetone triperoxide	3,3,6,6,9,9-hexamethyl 1,2,4,5,7,8-hexoxonane
DADP -Diacetone diperoxide	3,3,6,6-tetramethyl-1,2,4,5-tetroxane
TMDD -Tetramethylene diperoxide dicarbamide	1,2,8,9-tetraoxa-4,6,11,13-tetraazacyclotetradecane-5,12-dione
HMTD -Hexamethylene triperoxide diamine	3,4,8,9,12,13-hexaoxa-1,6-diazabicyclo [4.4.4]tetradecane

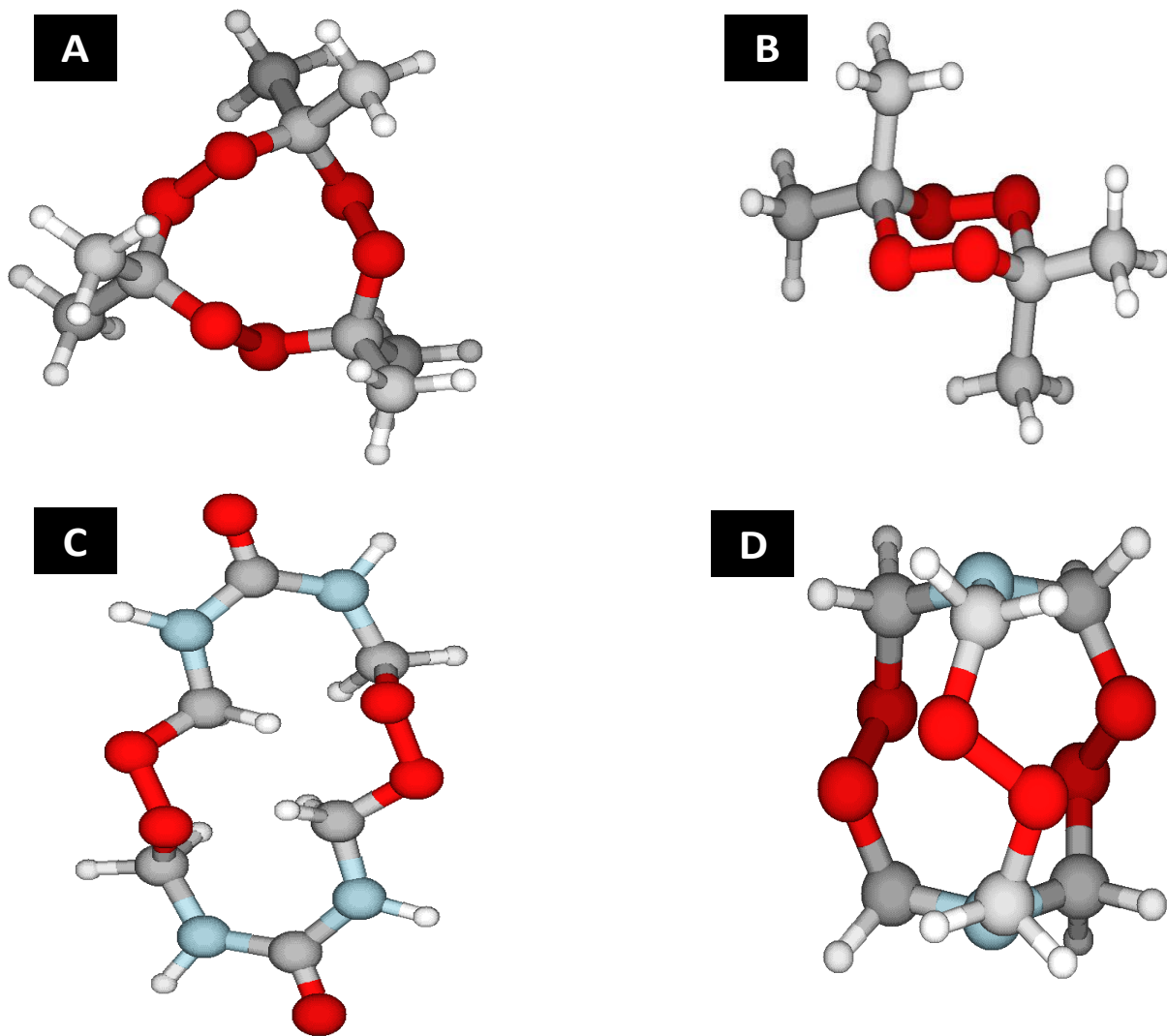


Figure 1-1. Optimized structures of the homemade explosives studied. a) TATP, b) DADP, c) HMTD, and d) TMDD.

Chapter 2

2. A MECHANISM FOR UNCATALYZED ACETONE-PEROXIDE FORMATION REACTION: AN EXPERIMENTAL AND COMPUTATIONAL STUDY

This chapter is focused on proposing a viable mechanism for the uncatalyzed acetone-peroxide formation reaction based entirely on qualitative and quantitative Raman and NMR spectroscopy measurements and is supported by DFT theoretical modeling of the proposed intermediates and transition states. An important consideration in the area of HME preparations is the fact that some of them can be prepared from household or consumer products. So, their production and use is extremely difficult to control by security enforcing authorities. As a result, these agencies are highly interested in gaining more control over HME production and use. Information about reaction pathways helps improve two important security aspects. The first aspect deals with the possibility of inhibiting the formation of HME by adding interfering agents. The second aspect deals with devising new methods of forensic analysis that may assist in tracing HME to the perpetrators. Another advantage of elucidating reaction mechanisms is that it could lead to the possibility of substituting household chemicals with passive equivalents that may inhibit the formation of HMEs.

2.1 EXPERIMENTAL SETUP

2.1.1 Reagents

American Chemical Society (ACS) certified acetone (99.7% purity) and hydrogen peroxide, stabilized and certified (50% aqueous solution) were obtained from Fisher Scientific International (Pittsburg, PA, USA). Reagents were used without further purification. Ultra high

purity water (UHP, 18.2 M Ω) produced by a Nanopure® system, Barnstead International, (Thermo-Fisher Scientific, Dubuque, IA, USA) was used for preparation of aqueous solutions and for washing precipitated TATP crystals after synthesis.

2.1.2 Experimental Details

Raman spectroscopy was employed to monitor the uncatalyzed reaction between acetone and peroxide. Raman spectra were collected on a daily to examine the reaction course (see Figure 2-1a). Spectral acquisitions were terminated when the first TATP crystals began to appear, which is close to thirty days for the uncatalyzed reaction based on the literature [1]. To perform the daily measurements, hydrogen peroxide and acetone were mixed in a 1:1 molar ratio in clear glass vials at room temperature (~22°C). Kinetic runs of the reaction mixtures were temporally recorded using Raman spectroscopy in the temperature range of 30 to 60°C (see Figure 2-1b). To maintain control of the temperature, a rectangular flow cell (model 72-Q-10) obtained from Starna Cells, Inc. (Atascadero, CA, USA) was employed in all experiments. All spectral measurements were obtained at 514.5 and 532 nm laser excitation lines and compared with each other to evaluate the variations in the relative intensity patterns. To corroborate changes in the chemical environment of the carbonyl carbon atom and the methyl group as the reaction progressed, nuclear magnetic resonance measurements of the reaction mixture were obtained every two days because the reaction rate of the uncatalyzed is relatively slow [8].

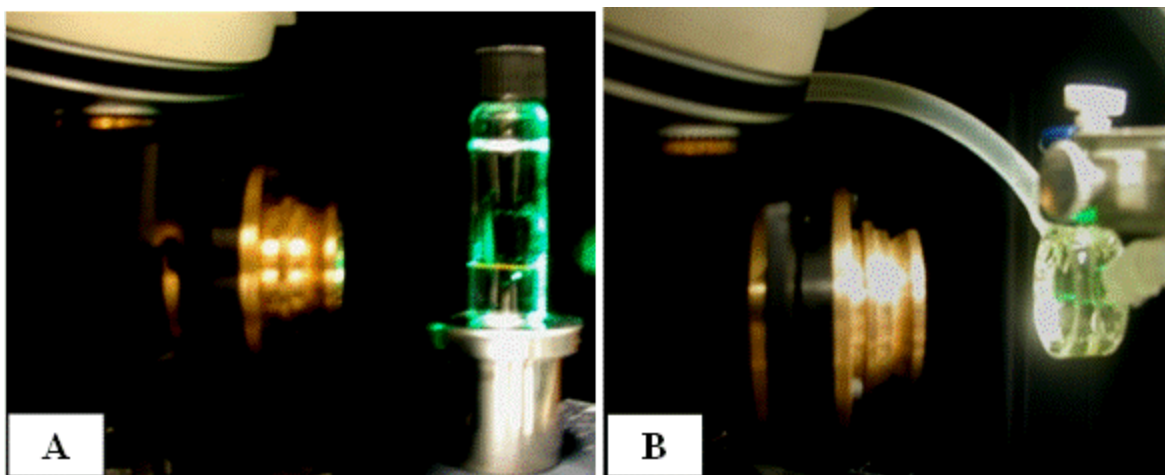


Figure 2-1. (a) Close up view of experimental setup for Raman Spectroscopy daily measurements. (b) Experimental setup for Raman spectroscopy kinetics measurements.

2.1.3 Equipment and Spectral Conditions

The Raman spectra were acquired using the following conditions: Raman shift range: 100-3200 cm^{-1} ; accumulations: 2; acquisition time: 10 s; laser power levels: 10-60 mW; excitation lines: (1) 514.5 nm laser line of an INNOVA 308 argon ion laser line (Coherent, Inc. Santa Clara, CA, USA) and (2) 532 nm laser line of an Excelsior-532 solid state diode laser system (Spectra-Physics, Newport, Corp., Irvine, CA, USA). For these measurements, Renishaw RM2000 and RM1000 Raman Microspectrometers were used.

For the nuclear magnetic resonance experiments, a Bruker FT-NMR Advance 500 MHz Spectrometer (Bruker Instruments, Inc., Billerica, MA, USA) was used. The typical conditions for the nuclear magnetic resonance measurements are described below. For acquisition of the ^1H -NMR spectra, the experimental conditions were: deuterium oxide (D_2O) and acetone- d_6 solvents; number of transients (NS): 16, spectral width (SWH): 10330.578 Hz and acquisition time (AQ): 3.172 s. For the ^{13}C -NMR spectra, the conditions were: D_2O and acetone- d_6 solvents, NS: 32, SWH: 30030 Hz and AQ: 1.09124.

Gas chromatography analysis was performed using an Agilent GC 5890 (Agilent, Inc. NM, USA) equipped with a Supelco SPB-5 (5% biphenyl 95% dimethylsiloxane, C-18 15.0 m, 250 μm x 0.25 μm) column and coupled to a 5790 mass selective detector (Agilent). The GC conditions were as follows: (I) Inlet: Temp. 150 $^{\circ}\text{C}$; splitless mode; constant flow. (II) Oven: Initial Temp. 80 $^{\circ}\text{C}$; Ramp 10 $^{\circ}\text{C}/\text{min}$; final temp. 230 $^{\circ}\text{C}$; carrier gas: He (Praxair-PR, Gurabo, PR).

2.1.4 Density Functional Theory Calculations

To perform the theoretical calculations, the structures of the relevant molecules were drawn using the GaussView[®] software package. Then, the connectivity Z-matrices of the structures were reorganized using the Molden[®] software package taking into account the most likely interaction points. The transition state (TS) geometries were optimized, and frequency calculations were performed to verify that the optimized geometries were transition states prior to their use in the intrinsic reaction coordinate (IRC) calculations. Then, IRC calculations followed in both directions (forward and backward) from the TS. The IRC calculations of the subsequent steps could not be modeled as in the first step, because, it was not possible to find a transition state between two monomer molecules or the reaction occurred rapidly and had no transition state. Thus, the second order kinetic pattern observed and the confirmation of Terent'ev et al. results was proposed considering the atomic charges densities [13]. The activation energy of the dimerization step was estimated scanning the reaction coordinate of the proposed interaction.

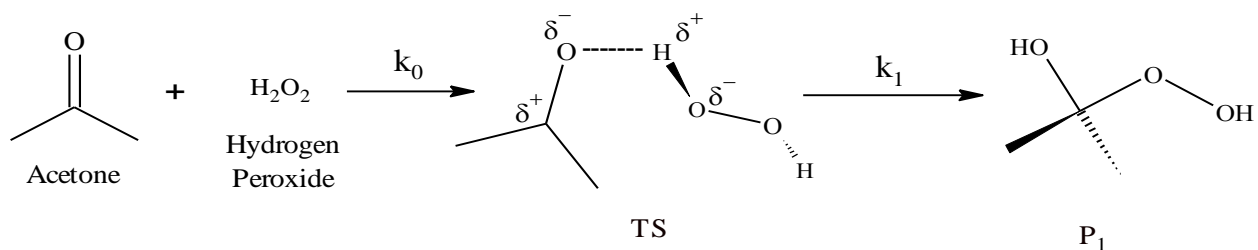
This theoretical analysis was performed at the density functional theory (DFT) level using Becke's three-parameter modification [19] of Lee-Yang-Parr [20] hybrid functional (B3LYP) and the 6-31++g(d,p) [21] basis set. The Gaussian 03TM software package [22] was employed for

these calculations. The properties of the ground states and intermediate states of the reactions were computed, analyzed and compared to the experimental data.

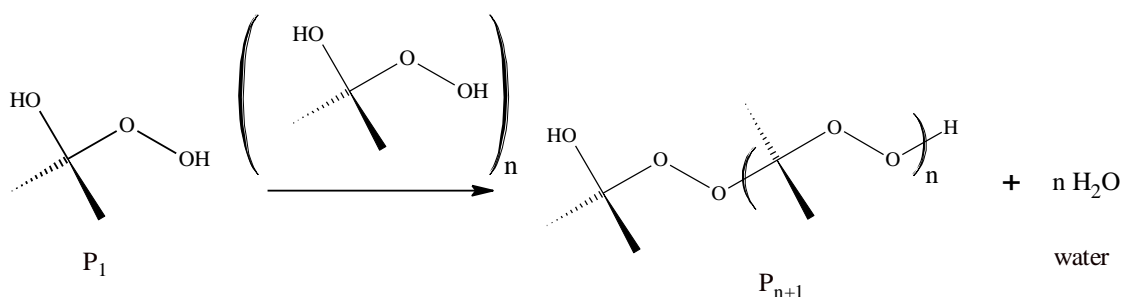
2.2 RESULTS AND DISCUSSION

2.2.1 Description of the CAP formation Mechanism

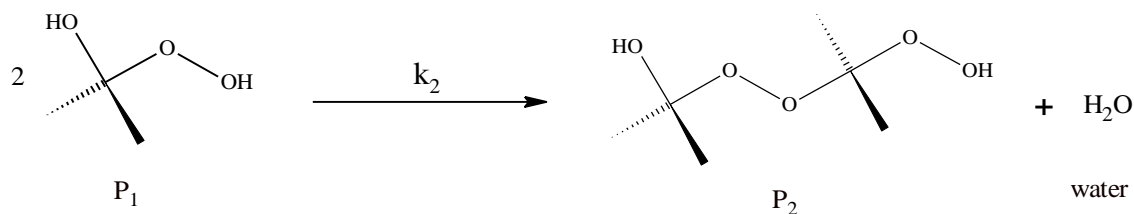
The uncatalyzed acetone-peroxide formation reaction was followed for several days using Raman and NMR spectroscopies, GC-MS, and was theoretically modeled using DFT calculations to characterize the starting materials, the final products, the possible reaction intermediates and transition states in order to propose a mechanism for the formation of TATP. The proposed mechanism was postulated to occur in three steps: monomer formation P_1 (2-hydroperoxi-2-propan-2-ol), polymerization and then cyclization (see Schemes 2-1, 2-2, 2-6 and 2-7). At the onset of the reaction, a hydrogen peroxide molecule interacts with an acetone molecule. In the polymerization and cyclization steps, the hydroperoxyl and alkoxy terminal groups react by eliminating a water molecule via a hydro-peroxyl condensation (HPC) reaction. Scheme 2-2 illustrates the process in general form while Scheme 2-3 shows the process specifically for the formation of the dimer P_2 (2-[(2-hydroperoxyl propan-2-yl) peroxy] propan-2-ol). Scheme 2-4 describes the formation of P_3 . The details of bonds broken and formed are depicted in Scheme 2-5. Schemes 2-6 and 2-7 illustrate the third and final step: cyclization by condensation. Scheme 2-6 illustrates the formation of the dimeric structure (C_2): diacetone diperoxide (DADP). Scheme 2-7 shows the cyclization of P_3 (2-({2-[2-hydroperoxyl propan-2-yl] peroxy] propan-2-yl} propan-2-ol) to form the trimeric cyclic structure (C_3): triacetone triperoxide (TATP). In short, the second and third steps were proposed to occur through a HPC reaction. Other possible reactions such as the reaction between polymers structures (P_n) of different orders were not sketched in the above schemes, but they were considered in the deduction of the total kinetics.



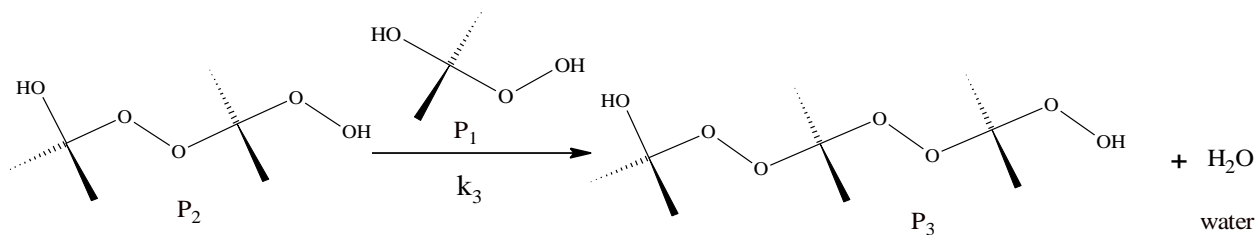
Scheme 2-1. Acetone and hydrogen peroxide molecules start interacting at close range by forming a hydrogen bond. This process is very fast and is not included in overall mechanism proposed. First step: monomer formation from intermediary or transition state (TS). Monomer is designed as P₁: (2-hydroperoxy, 2-propan-2-ol).



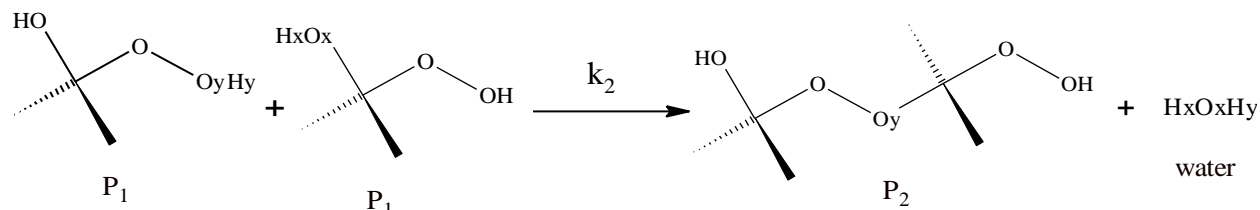
Scheme 2-2. Second step: alkoxy-peroxyl condensation reaction: general scheme for polymerization step.



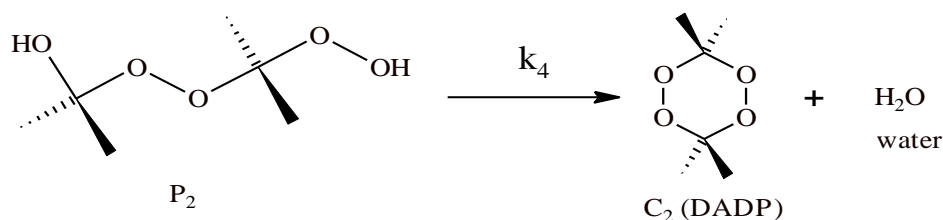
Scheme 2-3. Dimerization between two P₁ molecules and formation of P₂ dimer: (2-[(2-hydroperoxy propan-2-yl) peroxy] propan-2-ol).



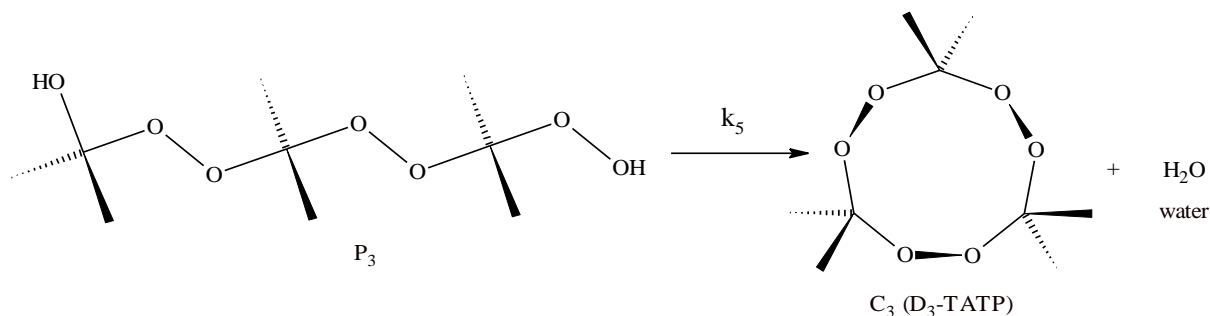
Scheme 2-4. Formation reaction of P₃ (an alkoxy-peroxyl condensation reaction) from P₂ and P₁ reacting molecules (trimerization). Trimer is designed as P₃ (2-[(2-[(2-hydroperoxy propan-2-yl) peroxy] propan-2-yl) peroxy] propan-2-ol).



Scheme 2-5. Postulation of details of polymerization step: bonds broken and formed based on density charges of the terminal oxygen atoms.



Scheme 2-6. Alkoxy-peroxyl cyclocondensation reaction of P_2 : formation reaction of C_2 . This cyclic acetone peroxide product is identified as 3,3,6,6-tetramethyl-1,2,4,5-cyclotetroxane or diacetone diperoxide (DADP).



Scheme 2-7. Alkoxy-peroxyl cyclocondensation reaction of P_3 : formation reaction of C_3 . This cyclic acetone peroxide product is 3,3,6,6,9,9-hexamethyl-1,2,4,5,7,8 hexaxonane or triacetone triperoxide (TATP).

2.2.2 Monomer Formation Step

The two interacting molecules: acetone and hydrogen peroxide were already well oriented for the reaction to occur due to the formation of hydrogen bond. In fact, the hydrogen bond forms readily when acetone is dissolved in water. This was evidenced by band broadening and red-shifting of the band assigned to the C=O bond (carbonyl) in the acetone spectrum as illustrated in detail in Figure 2-2a for the Raman spectra for: neat acetone, acetone/water solution and acetone-

hydrogen peroxide reaction mixture. A significant red-shift can be observed for both the acetone-water solution spectrum (1640-1725 cm^{-1}) and for the spectrum of the reaction mixture (1600-1700 cm^{-1}). This can be contrasted to neat acetone spectrum where the range for the free carbonyl is 1700-1750 cm^{-1} . The reaction mixture shows a larger shift of $\Delta\bar{\omega} \sim -40 \text{ cm}^{-1}$, indicative of a stronger interaction rather than a simple hydrogen bond. This interaction was also evidenced in the methyl stretching region. Specifically a blue-shift was observed for C-H bond symmetric stretching (from 2923 to 2927 cm^{-1}) as result of the strengthening of the C-H bond and a new peak at 2952 cm^{-1} corresponding to the $\nu_{\text{C-H}}^{\text{s}}$ of the first product of the reaction (see Figure 2-2b). Figure 2-3 illustrates the change in the chemical environment of the acetone molecule as the reaction progresses as evidenced from Raman spectra. At the onset of the chemical transformation, the reaction mix and acetone Raman spectra are roughly similar, and only a minimal shift due to hydrogen bonding is observed. Then, the spectra change according to the formation of principal intermediates and cyclic product (TATP), whose splitting and characteristic bands appear specifically at 590 cm^{-1} , 800 cm^{-1} , 1450 cm^{-1} and 960 cm^{-1} . These vibrational bands correspond to the deformation of O-C-O angle ($\nu_{\text{O-C-O}}$) of monomer molecule, symmetric stretching of C-C bond ($\nu_{\text{s,C-C}}$) and deformation CH_3 (ν_{CH_3}) of the acetone molecule and asymmetric stretching of C-O bond ($\nu_{\text{a,C-O}}$) of the TATP molecule, respectively, and they were tentatively assigned using the theoretical vibrational spectra with DFT method at B3LYP level of theory and 6-31++g (d,p) basis set [19-21].

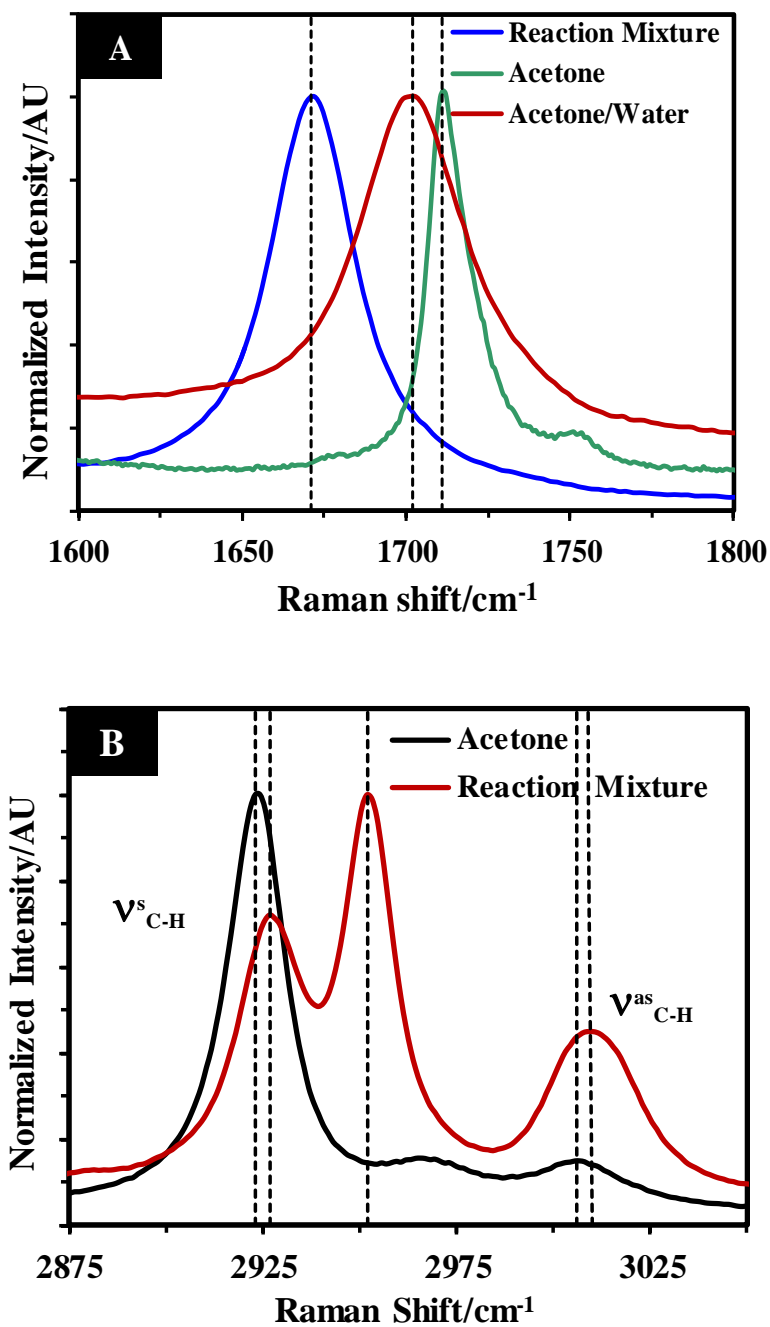


Figure 2-2. (a) Variation of C=O Raman shift location due to the hydrogen bonding formation from normal range of 1690-1740 cm⁻¹ to 1600-1700 cm⁻¹. (b) Variation of CH₃ Raman shift due to the hydrogen bonding formation from of 2923 cm⁻¹ to 2927 cm⁻¹ and formation of a new band corresponding to the first product (P₁ monomer).

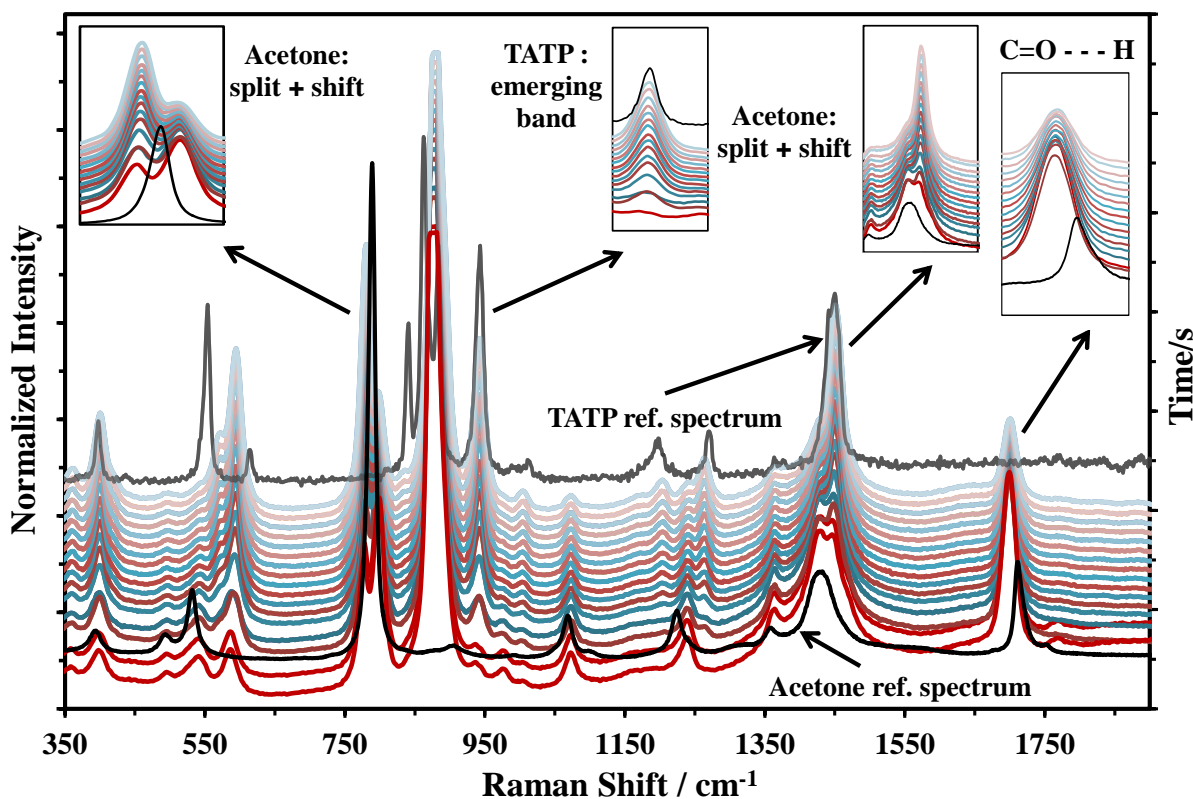


Figure 2-3. Variation of Raman shift location during a kinetic run. No significant difference between the starting and acetone spectra is observed.

On the other hand, carbonyl bonded to the peroxide hydrogen band ($\nu_{\text{C}=\text{O} \cdots \text{H}(\text{peroxy})}$), which appears at 1660 cm^{-1} and spanned a wavenumber range of $1600\text{-}1700 \text{ cm}^{-1}$ due to the formation of the hydrogen bond in acetone is surrounded by hydrogen peroxide and water molecules, and it is completely consumed in the first step. Therefore, this molecule cannot appear in the subsequent mechanism steps as shown in the reaction schemes. Consistently, the Raman intensity related to this band decayed following a first order decay rather than a more complex pattern to form the monomer molecule. These results lead to the first assumption of the proposed mechanism in which acetone is only consumed in a single reaction step (see Figure 2-4).

To analyze the kinetic pattern of acetone until the appearance of the first crystals of TATP, the CAP reaction was catalyzed with sulfuric acid at trace level, because the uncatalyzed reaction

is too slow to obtain meaningful results. It was found that the Raman intensity of the carbonyl band ($\nu_{\text{C=O}\cdots\text{H}}$) initially decays with a kinetic pattern of first order to form the monomer molecule, then it is held constant during the polymerization step and finally when the first insoluble crystals of TATP are formed by Le Chatelier-Braun principle it follows consuming with a first order decay as is shown in Figure 2-5. The final decay was related to Le Chatelier – Braun principle, because the rate constants of the final decay for several bands have the same value. Again, this leads to the first assumption of the mechanism proposed: acetone is consumed in a single reaction step. The same happens with other new bands formed in the spectral range of $532\text{-}620\text{ cm}^{-1}$ (see Figure 2-6).

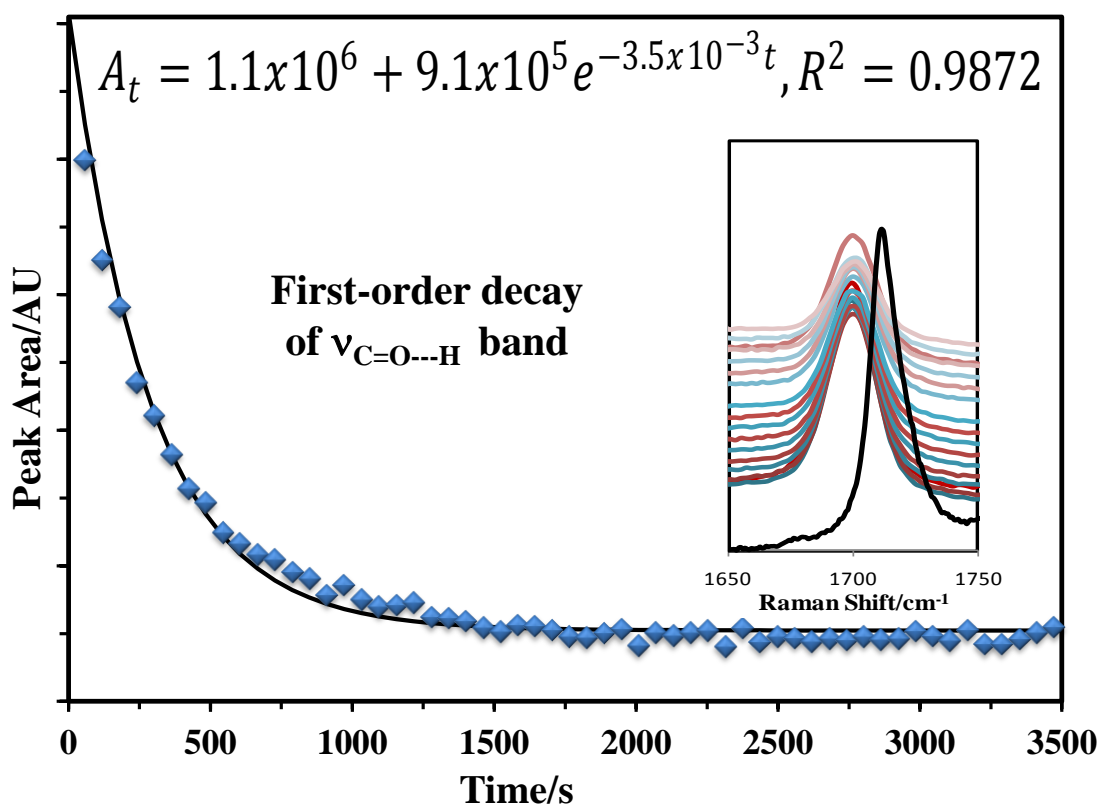


Figure 2-4. First-order decay of the C=O...H band intensity for an uncatalyzed reaction.

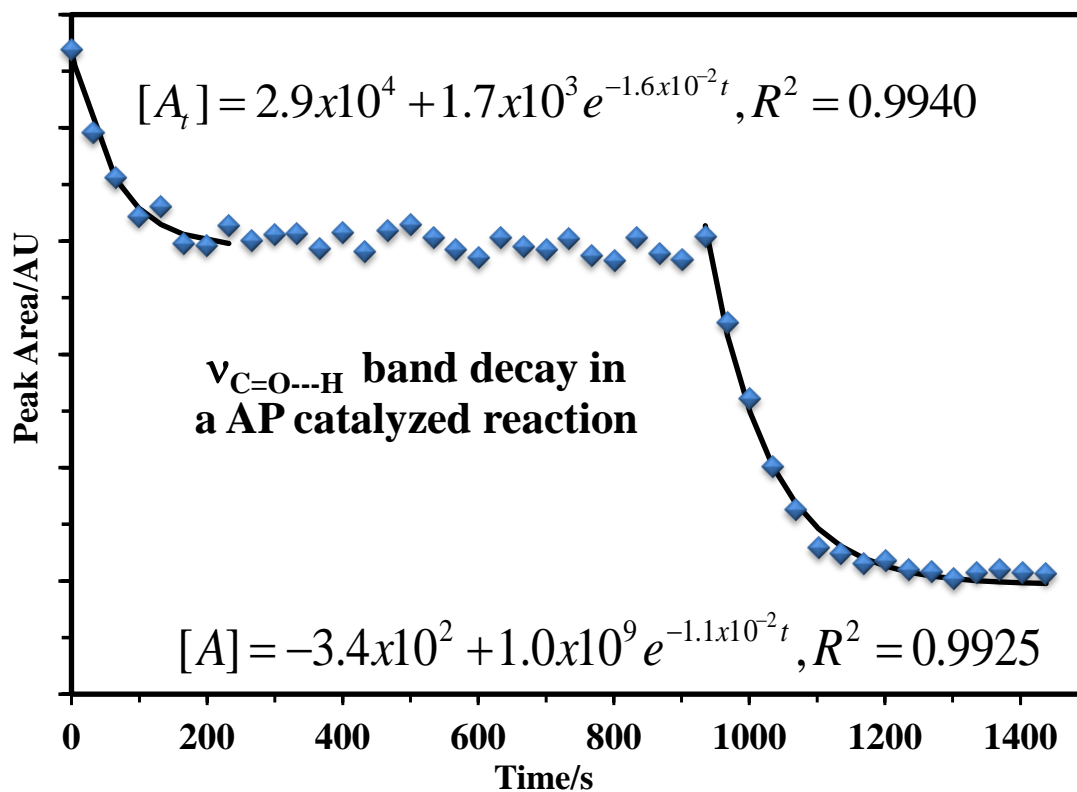


Figure 2-5. Intensity decay of $\nu_{C=O}$ band during a kinetics run of a catalyzed AP-reaction

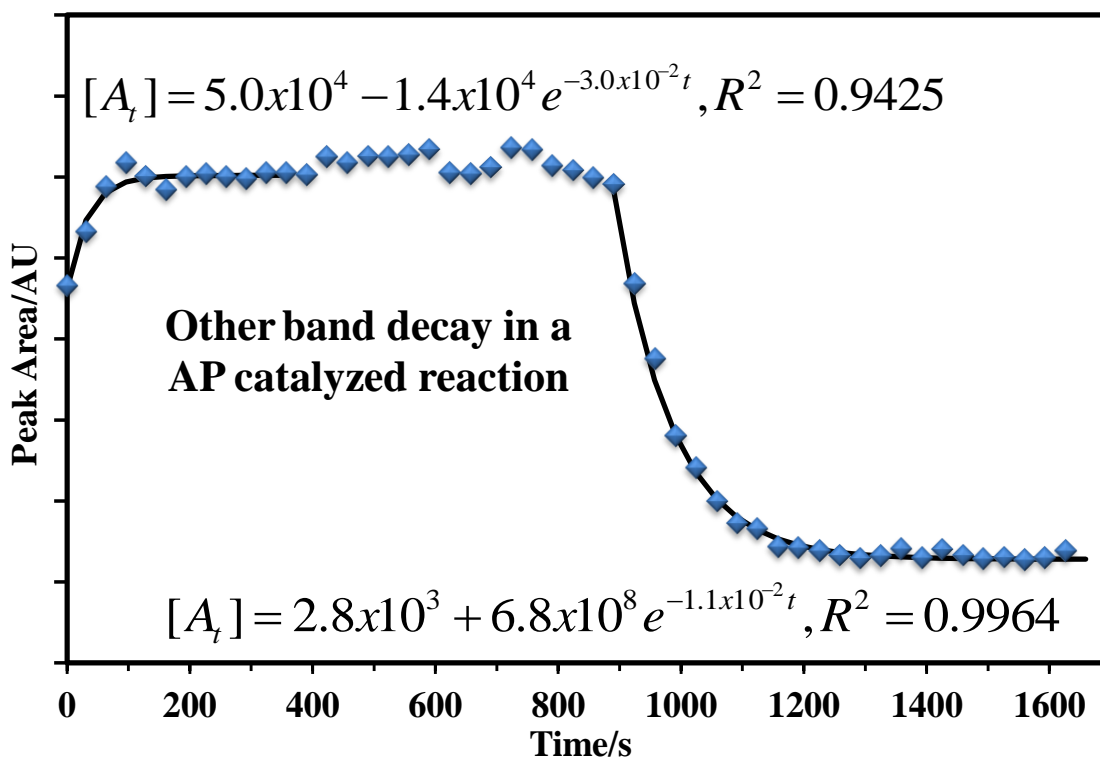


Figure 2-6. Intensity growth and decay of others band during a kinetics run of a catalyzed AP-reaction

2.2.3 Theoretical Support of the Monomer Formation Step

According to IRC theoretical results, the TS of the first step is postulated to proceed via formation of hydrogen bonding between the interacting molecules, in which the hydrogen atom gets closer to the oxygen atom to form the O-H bond and carbonyl bond decreases its bond order from 2 to 1.5, by changing from a triangular planar structure to a nearly tetrahedral structure. The diminished electron density on the carbonyl C atom is then concertedly attacked by the peroxide oxygen atom as illustrated in Figure 2-7. The bond length for a normal H-O bond in an optimized hydrogen peroxide structure is 0.96 Å. The O-H bond lengths in the TS were found to be 1.55 Å for peroxy O-H bond and 1.01 Å for C-O—H bond. Evidently the hydrogen atom of the peroxide molecule is closer to the carbonyl oxygen atom than peroxy oxygen, corroborating the above statement.

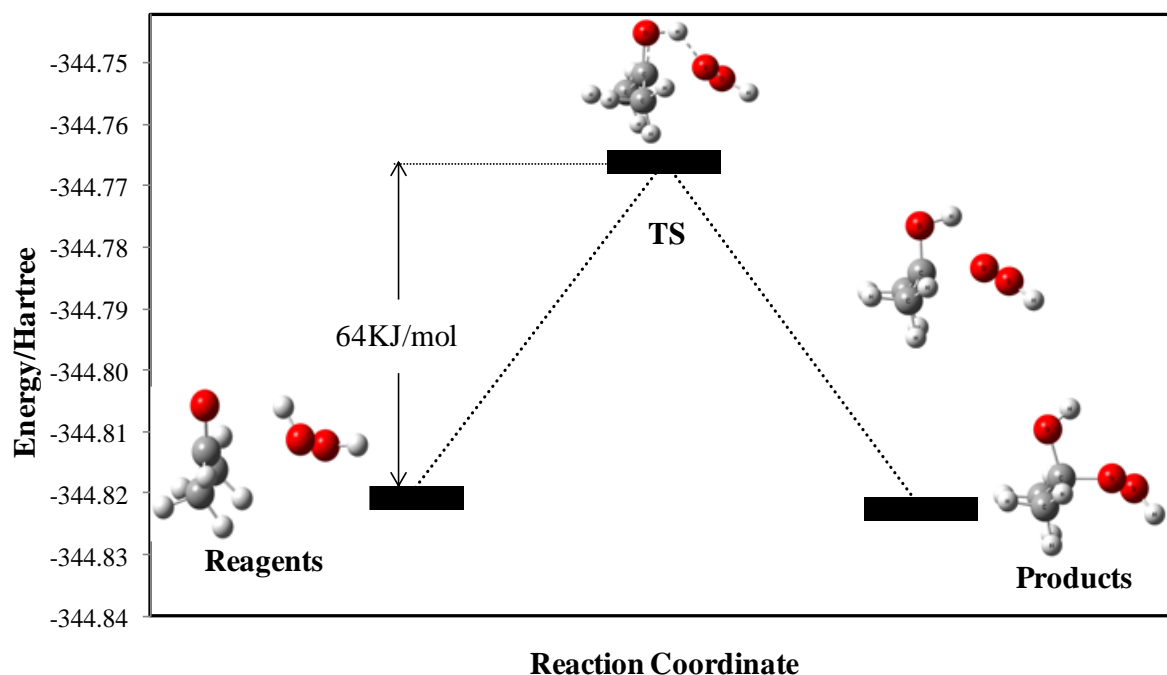


Figure 2-7. Energy diagram and sequence of atomic movements in the first step at DFT level (B3LYP/6-311++g(d,p)): The atomic motion sequences were: Initial nucleophilic attack of lone electron pair of carbonyl Oxygen atom of acetone to peroxide H atom. The formation of a new O-H bond and decreasing of C=O bond order. Quick interaction between the peroxy oxygen atom and the carbonyl carbon atom. Finally, the formation of new C-O bond is accomplished.

2.2.4 Polymerization Step

Figures 2-3 and 2-8 showed key Raman features that resulted to be very important and decisive in the elucidation of the proposed mechanism among which are:

Splitting of the $\nu_{s(C-C)}$ and $\delta_{(CH_3)}$ bands of the acetone structure, which appear at 800 cm^{-1} and 1420 cm^{-1} in the Raman spectrum of acetone and formation of new bands at 590 cm^{-1} and 960 cm^{-1} related to $\delta_{(O-C-O)}$ and $\nu_{a(C-O)}$ vibration mode of the P_1 -monomer and TATP structure respectively, which are indications of a change in the environment of the monomer unit structure as the polymerization progresses and generation of a single bond type. This is consistent with Schemes 2-2, 2-3, and 2-4.

The high similarity found in the Raman spectra of all the mixtures studied taken at different days, particularly in the fingerprint region of the spectra, is evidence that just the C-O bonds have been formed and that the intermediaries have highly similar structures as proposed by the above route. In the proposed mechanism, the bonds formed are of the same type (C-O). Therefore, the Raman spectra of the polymeric structures designated as P_1 , P_2 and P_3 should not differ significantly. In fact, the only variation observed were in the intensity and unfolding of some signals, which indicates the growth of the polymer chain. In other words, the monomeric unit is changing its chemical environmental as the polymer chain increases in length.

To further corroborate the above statements, kinetic measurements were made, resulting in good agreement between the proposed mechanism. The formation of a new band corresponding to ω_{O-C-O} band [23] that rapidly appeared around $\sim 540\text{ cm}^{-1}$ in the Raman shift spectrum and then decayed with a second order kinetics pattern is in complete agreement with the postulation of the dimerization stage (see Figure 2-8 and Scheme 2-2).

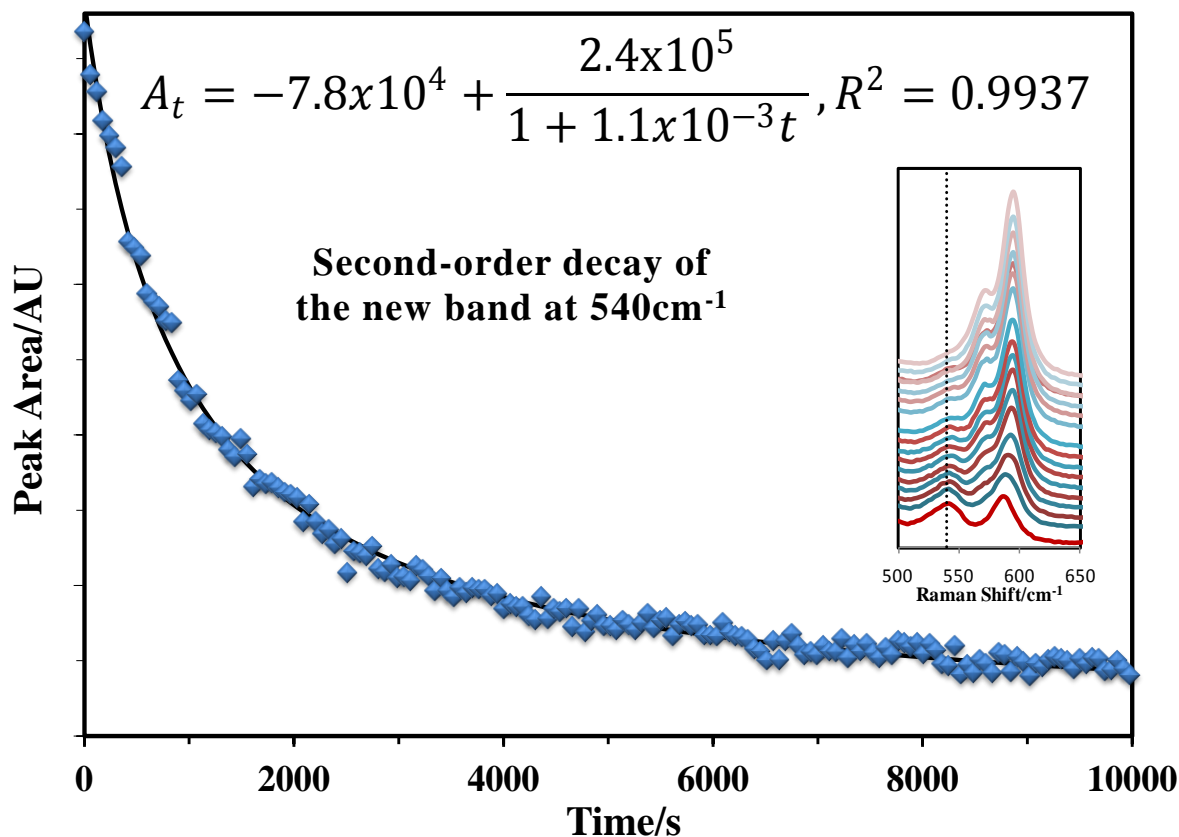


Figure 2-8. Second-order decay of the new band at 540 cm⁻¹ for an uncatalyzed reaction.

The kinetic orders of the different decays were corroborated with the fractional times method. This method is based on the average values obtained for the quotient of $t_{3/4}/t_{1/2}$ [24], in which values of 2 and 3 are confirmatory for first and second order, respectively. The average values found for the kinetics fittings shown in Figures 2-4 and 2-8 were 2.99 and 1.99, respectively, at several points of the decaying intensities, corroborating the key kinetics orders for the proposed mechanism (see Table 2-1). The C-O band decays with first order rate while the new band disappears after forming with second order rate kinetics. All kinetic decays were adjusted using the method of nonlinear least squares, which adjusted well to the respective kinetic behavior, as reflected in R^2 value. The average value of constant k_1 (first step) is lower than the average value for k_2 (dimerization reaction) by about 10^3 times. Therefore, the second

reaction is much faster than first one. Another interesting finding is that the activation energy or energetic barrier of the first step is twice higher than the polymerization step, which reaffirms the results previously reported by Terent'ev et al., that the polymerization reaction is more energy favored than keto-peroxyl reactions [13]. On the other hand, the experimental activation energies (E_a) were consistent with theoretical calculations in terms of order and magnitude. Table 2-2 summarizes all kinetics constants and activation energies at the temperature range studied. The kinetics pattern equations in terms of physical measurements for first and second order were adapted from Espenson [24].

Table 2-1. Fractional times for different kinetics orders and quotient of fractional times for Acetone and new band decaying.

Order	$t_{3/4} / t_{1/2}$ predicted value	$t_{3/4} / t_{1/2}$ value for decaying of carbonyl band	$t_{3/4} / t_{1/2}$ value for decaying for new band formed
0	1.5	1.8	3.0
1	2.0	2.2	2.9
2	3.0	2.0	3.0

Table 2-2. Constant rate and Activation Energy for all possible reaction, calculated at DFT level using B3LYP hybrid functional and 6-311g++(d, p) basis set [15]. -- Not calculated.

T/°C	k_1	k_2	E_{a1} (KJ/mol)		E_{a2} (KJ/mol)	
			Exp.	DFT	Exp.	DFT
30	$(7.8 \pm 0.1) \times 10^{-4}$	$(680.9 \pm 0.3) \times 10^{-4}$	41 ± 5	64	21 ± 3	29
40	$(15.9 \pm 0.4) \times 10^{-4}$	$(650.9 \pm 0.7) \times 10^{-4}$				
50	$(25.0 \pm 0.8) \times 10^{-4}$	$(825.6 \pm 0.3) \times 10^{-4}$				
60	$(35 \pm 1) \times 10^{-4}$	$(1188 \pm 2) \times 10^{-4}$				

2.2.5 Theoretical Support of the HPC Steps

The polymerization and cyclization steps were proposed to occur through a HPC reaction based on the charge densities on the hydroxyl and peroxy oxygen atoms, which are higher and sterically favorable on hydroxyl oxygen atom than the peroxy oxygen. Figure 2-9 shows a cross section of the molecular electrostatic potential distribution (MEP) of the O-C-O-O plane of the P₁ monomer structure. The red and yellow lines represent the electronegative potential and electropositive potential, respectively. This picture clearly shows that hydroxyl oxygen atom has electronegative potential lines more pronounced and extended than peroxy oxygen atoms by covering a higher electronegative area. In other words, the electron cloud of hydroxyl oxygen is mostly delocalized, by converting it in a point more suitable for an electrophilic attack or an interaction with hydrogen atom. Relevant computational values for charge densities of hydroxyl oxygen atoms and peroxide oxygen atoms calculated at DFT level of theory using B3LYP hybrid functional and 6-311g++(d, p) [19-21] basis set are contained in Table 2-2. The HPC reaction also is supported by the results of Terent'ev, et al., which affirms that peroxy-alkoxy condensation reaction is more energetically favorable than a keto-peroxy condensation reaction [13]. On the other hand, several researchers have reported some of the intermediates structures proposed in this manuscript [25-29].

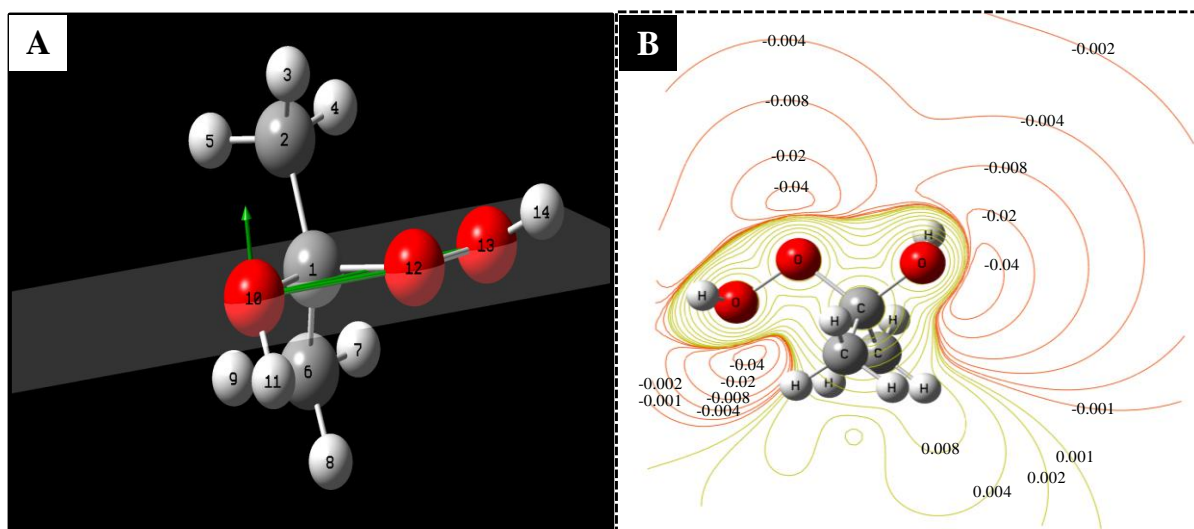


Figure 2-9. (a) O-O-C-O reference plane in which the charge distribution was sketched (b) Molecular electrostatic potential (MEP) contour map of the O-O-C-O plane: A cross section of the electrostatic spatial distribution at DFT level and B3LYP/6-311++g(d, p) basis set. This picture clearly shows that hydroxyl oxygen atom is the point more suitable for an electrophilic attack.

Table 2-3. Mulliken atomic and NBO charges of hydroperoxyl and alkoxy oxygen atoms of the terminal groups calculated at DFT level using B3LYP hybrid functional and 6-311g++(d, p) basis set. P₁, P₂, and P₃ are polymeric structures.

Atom	Charge Density					
	P ₃		P ₂		P ₁	
	Mulliken	NBO	Mulliken	NBO	Mulliken	NBO
Terminal Hydroxyl oxygen atom	-0.7536	-0.6250	-0.6570	-0.6250	-0.6605	-0.6260
Terminal Peroxide	-0.5102	-0.3250	-0.3533	-0.3260	-0.3750	-0.3130
Oxygen atoms	-0.3646	-0.3990	-0.3243	-0.4000	-0.3316	-0.4090

2.2.6 Cyclization Step and Total kinetic

The kinetics pattern of the global and some individual steps were measured through intensity decays of the key Raman active vibrations and were successfully related to the proposed mechanism. The global kinetics was expressed in terms of TATP, and this concentration was monitored using $\nu_{a(C-O)}$ band, which appears at 940 cm^{-1} and it is an important non-overlapping band of this compound. The TATP formation doesn't take thirty days as is reported [2, 8]. What is delayed is the precipitation of crystals from the reaction media.

Although, all HPC reactions have similar energy barriers, in a polymerization reaction the more probable collisions occur between the monomer (P_1) and long-polymer (P_n) molecules or the pre-exponential factor (A) of the Arrhenius law is higher than in others possible encounters, because the monomer molecule has greater diffusivity than other long chain-polymers. Consequently the polymeric chain is elongated by progressive adding monomer molecules [30]. Another important experimental fact it is that TATP is the cyclic product of higher proportion in a catalyzed and uncatalyzed CAP-reaction ($> 90\%$ purity) [2, 8, 27-29], therefore other cyclization reactions are not significant in the overall kinetic when compared to cyclization of P_3 polymer. Taking into account the above physical consideration and experimental facts a total kinetic expression as a function of TATP concentration was found that successfully correlated with the temporal decay of the Raman intensity of TATP non-overlapping band (Eq. 1) with high R^2 acceptance value. This important result demonstrates that the postulated mechanism is a viable route for the TATP formation in an uncatalyzed reaction (see Figure 2-10). The mathematical details of the kinetic law derivation are included as a supplement material.

$$[\text{TATP}] = \frac{1}{2k_8} [\text{AP}]_o - \frac{1}{2k_8} [\text{AP}]_o e^{-2k_1 t} \dots 1$$

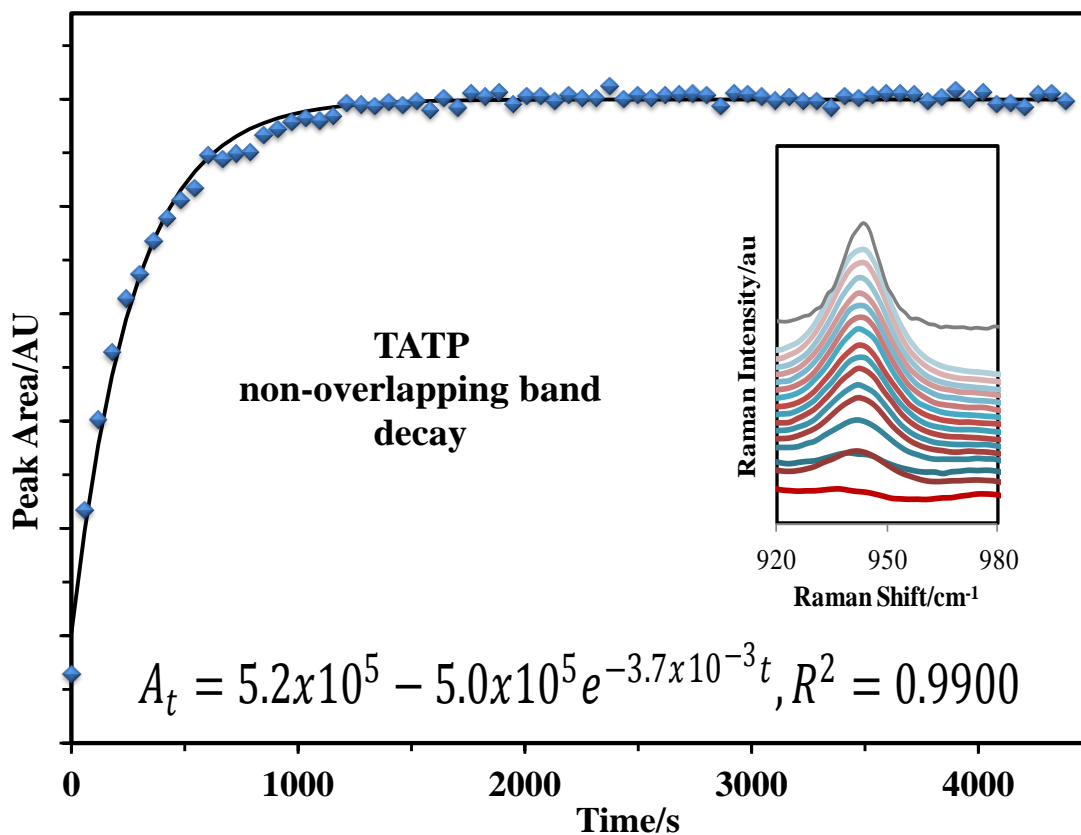


Figure 2-10. First order growth of the TATP non-overlapping band at 940 cm^{-1} for the uncatalyzed reaction.

On the other hand, the acid-catalyzed CAP reaction follows a mechanistic route analogous to the proposed here with some differences in terms of energy. At high acid-concentrations, the CAP-reaction releases a lot of energy, which leads to reactions of higher energetic requirements. Sometimes, this reaction becomes so energetically uncontrollable that causes loud explosions. The remarkable increase in the reaction rate of the acid-catalyzed CAP reaction is due to the alkoxy group is readily protonated by the acid-catalyst releasing a water molecule faster than a uncatalyzed reaction, generating more reactive intermediates and giving rise to a large number of reactions. This assessment explains the presence of several intermediaries such as diperoxy structures proposed in CAP-mechanism previously published [25-29]. In fact, the total kinetics

of the TATP formation in a catalyzed reaction follows the same pattern of the uncatalyzed one (see Figure 2-11).

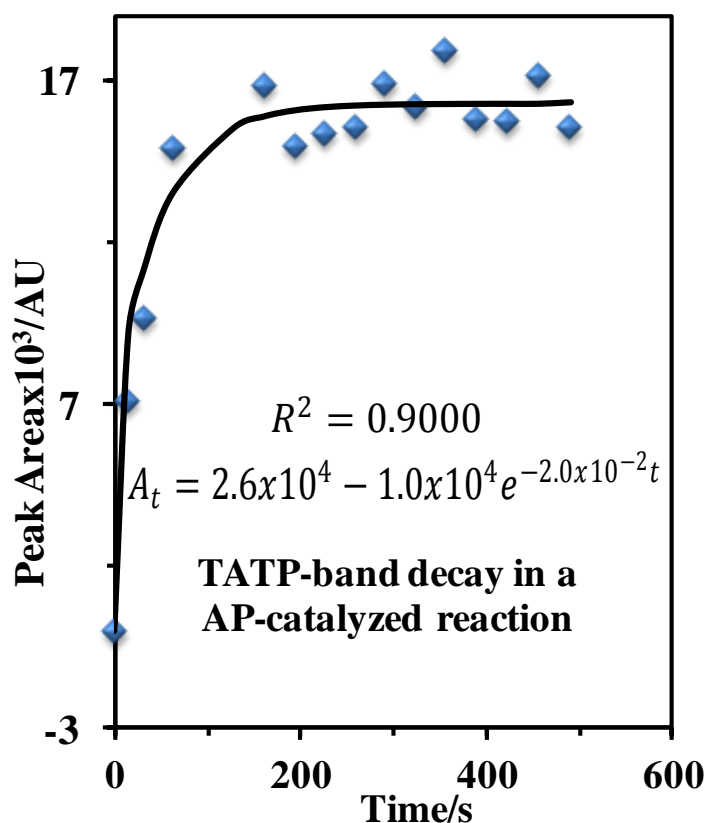


Figure 2-11. Kinetic growth of the TATP non-overlapping band at 940 cm⁻¹ for the acid-catalyzed reaction. The acid concentration was 1x10⁻³M of HCl

2.2.7 Evidence of Some Intermediates Structures

Nuclear magnetic resonance (NMR) measurements are in agreement with the suggested intermediate structures proposed in the mechanism. NMR chemical shifts obtained are summarized in Table 2- 4. ¹H-NMR shifts at 4.5 – 5 ppm and 3 – 4 ppm correspond to the peroxy and hydroxyl proton, respectively. In order to distinguish between them, ¹H-NMR spectra in deuterium oxide were obtained, and it was found that the ¹H-NMR shift at 3 – 4 ppm is related to hydroxyl proton, since the peroxy proton is less exchangeable than the hydroxyl one. On the other hand, consistent results in ¹H-NMR and ¹³C-NMR shifts were found in relation to

the proposed polymeric structures P₁, P₂ and P₃. For each type of carbon atom, one signal was observed, confirming that there are three different monomer environments in high proportion compared to others possible polymer structures. The third ¹³C-NMR shift at 100 – 110 ppm was not observed because either the abundance of ¹³C isotope (1.1%) is too low for its detection or some of them have the same shift. This does not occur with the ¹H-NMR spectra, due to the fact that ¹H abundance is much higher (about 99.8%) [31]. Another possible cause for not being able to detect the third ¹³C-NMR shift is that once the three units polymer (P₃) is formed, cyclization occurs to form TATP.

Table 2-4. ¹H-NMR and ¹³C-NMR shifts of the reaction mixture in D₂O and acetone-d₆ deuterated solvent.

Atom Type		¹ H-NMR Shift/ppm (Observed Signals)	¹³ C-NMR Shift/ppm (Observed Signals)
Hydroxyl hydrogen	(H O)-C(CH ₃) ₂ -(OOH)	3.6 (1)	----
Peroxyl hydrogen	(HO)-C(CH ₃) ₂ -(OO H)	4.5 (1)	----
Acetals carbon	(HO)- C (CH ₃) ₂ -(OOH)	----	100-120 (2)
Methyl hydrogen	(HO)-C(H ₃) ₂ -(OOH)	1.3-1.5 (3)	----
Methyl carbon	(HO)-C(C H ₃) ₂ -(OOH)	----	20-23 (3)

In order to corroborate some structural identities of the proposed mechanistic route and to consider it as a viable pathway of CAP-reaction leading to TATP, DADP and other cyclic products, a GC-MS study done on the reaction mixture, effectively confirming the presence of P₁ and P₂ intermediaries. Figures 2-12 and 2-13 show the electron impact MS spectra of these intermediates. In these, the molecular ions of 92 m/z and 166 m/z, which are the molecular weights of these structures, respectively can be readily identified. Another important result is that

both MS-spectra presented the same fragmentation pattern. P₂ MS-spectrum showed a fragment at 91 m/z, which is related to the 2-hydroperoxi-2-propan-2-ol moiety. The low intensity of respective MS fragments is due to the electron impact sensitivity and thermal instability of these organic peroxide compounds, even after optimizing the GC-MS conditions to reduce thermal breakdown [32-33].

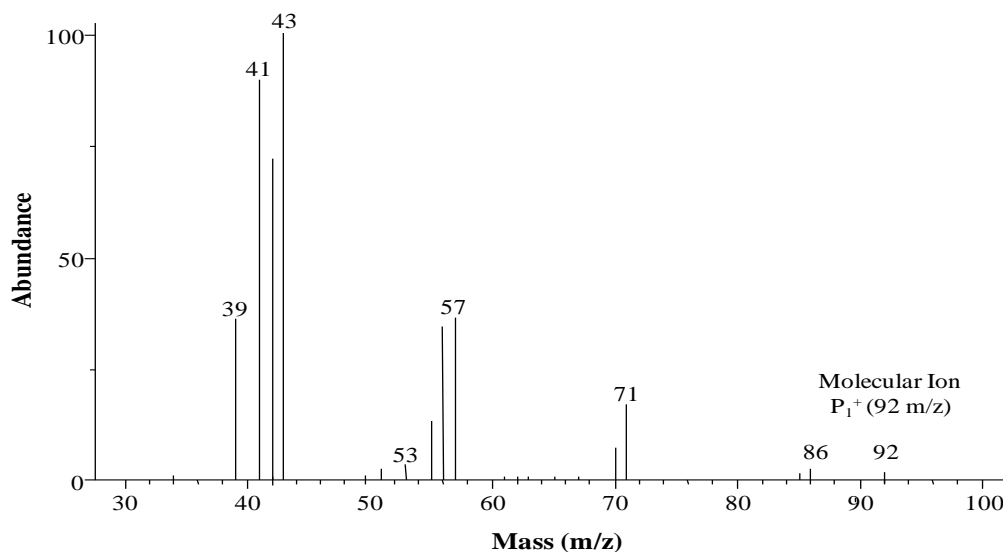


Figure 2-12. Electron impact ms-spectrum of P₁ structure; monomer of the proposed mechanism. Molecular weight of this structure is 92g/mol.

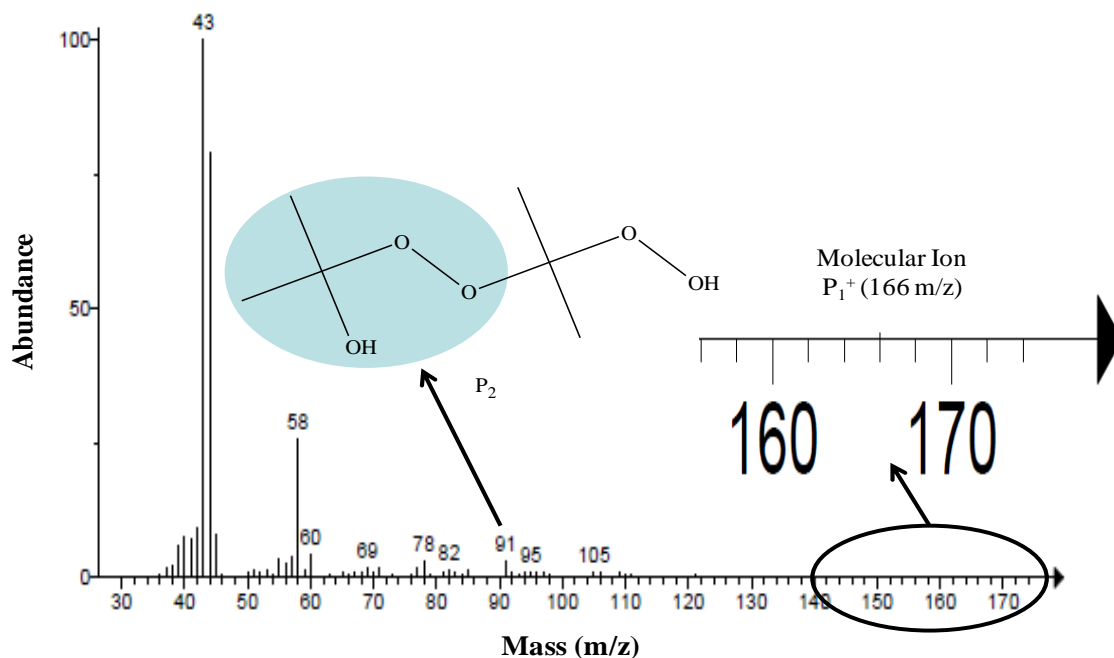
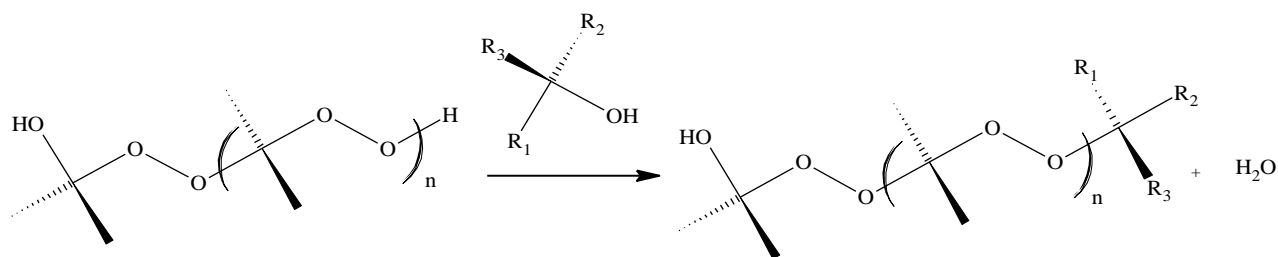


Figure 2-13. Gas chromatograph-electron impact mass spectrum of the gas phase AP formation reaction. The two main peaks at 0.86 min and 2.20 min are related to acetone and P₂, respectively.

2.2.8 A test of the CAP-mechanism with T-alcohols

The mechanism of the TATP formation reaction is proposed to involve successive alkoxy-peroxyl condensation reactions in which the intermediary molecules have both alkoxy and peroxyl terminal groups maintaining the forward progress of the reaction analogous to the condensation polymerization process. If species with hydroxyl tails, such as tertiary alcohols, are added to the CAP-reaction mixture, these molecules could react with the peroxyl tail of the intermediary molecules terminating the reaction and inhibiting TATP formation, which is consistent with the alkoxy-peroxyl and tert-alkoxy-peroxyl condensation reactions having comparable activation energies. This reaction is shown in the Scheme 2-8.



Scheme 2-8. Competitive inhibition reaction of CAP formation with tert-alcohols. These compounds clearly stop AP formation.

The competitive inhibition results from the formation of products that lack terminal groups required for the formation of TATP. A temporal profile of the $\nu_{C=O}$ band in the Raman spectrum shows how the concentration of acetone rapidly declines prior to complete TATP formation in a normal CAP-catalyzed reaction. Figure 2-14 shows how the concentration of acetone in a CAP-catalyzed reaction remains constant when a specific amount of t-alcohol is added. It is obvious that the reaction has terminated. The inhibition reaction is said to be competitive, because the expected amount of TATP formed is proportional to the amount of tert-alcohol added. Figure 2-15 shows in detail how the precipitated TATP varies according to the proportion of tert-alcohol until the TATP formation is null at a 1:1:1 molar ratio. The specific vibrational bands show evidence related to shifting of the $(R)_3C-O(H)$ bond. Specifically, Figures 2-16 and 2-17 show evidence of this chemical change. The O-H vibrational band (ν_{O-H}) of the t-alcohol was not used to follow the competitive inhibition reaction, because the reaction was carried out in aqueous media and the O-H band of the water molecule masks the results. The chemical assay was performed in two different tert-alcohols to corroborate this result. Both tert-alcohols produced the same results.

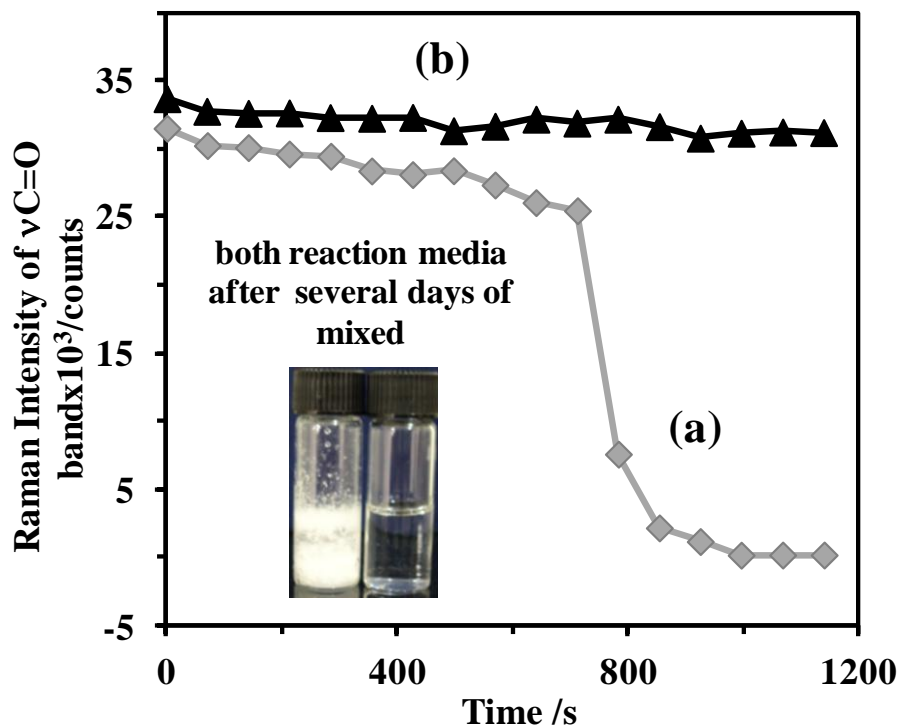


Figure 2-14. Temporal decay of $\nu_{C=O}$ band of the Raman spectra in an AP acid catalyzed reaction and decay of $\nu_{C=O}$ band in an AP-reaction when the t-alcohol is added.



Figure 2-15. (a) Visual view of Acetone-Peroxide T-butyl Alcohol Reaction at 5:1, 4:1, 3:1, 2:1 and 1:1 T-butyl Alcohol: acetone ratio. The precipitated TATP is proportional to alcohol amount (b) Acid catalyzed AP-reaction and AP-reaction plus T-alcohol.

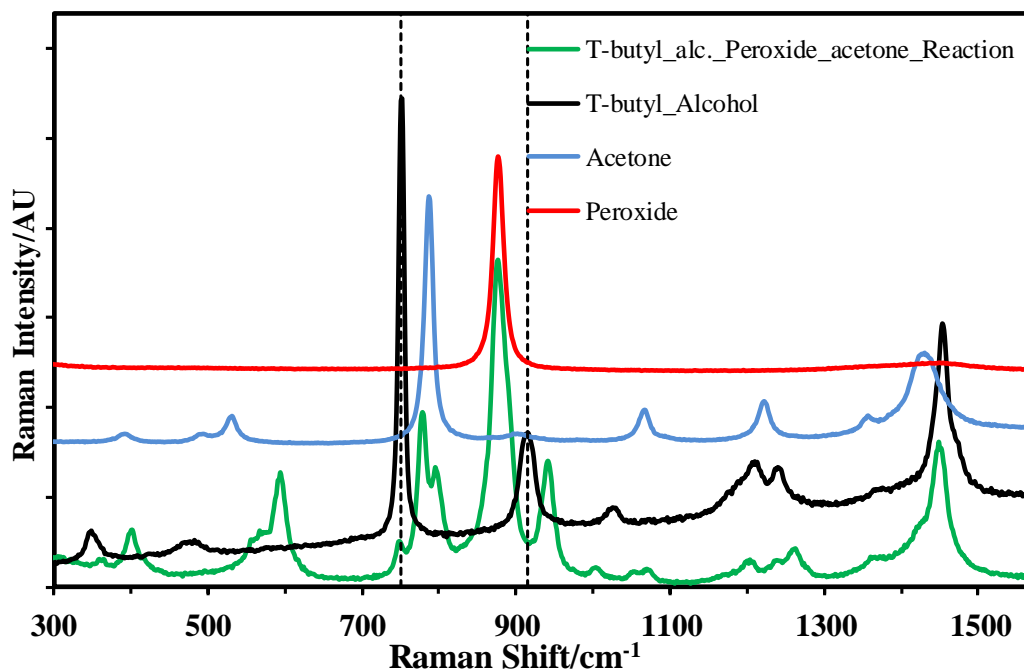


Figure 2-16. Acetone, T-butyl Alcohol and Acetone-Peroxide-T-butyl Alcohol Mix Raman spectra, the disappearing of $(R)_3C-OH$ band is clearly observed, at 900 cm^{-1} . The spectra were followed using a 532nm laser line.

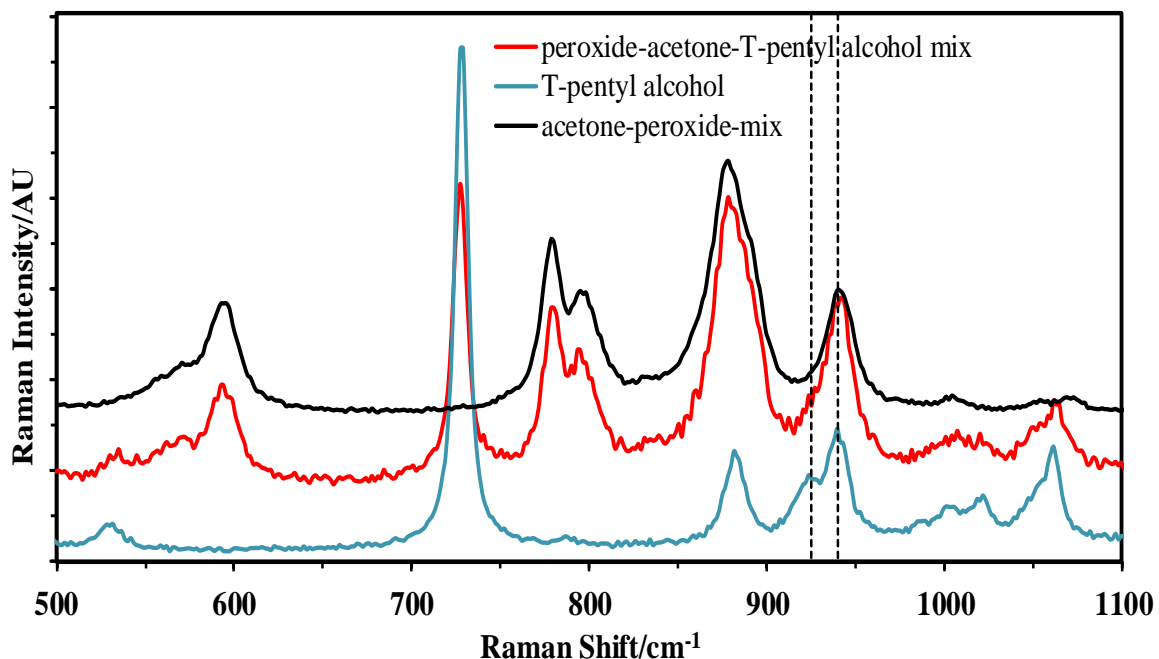


Figure 2-17. Acetone, T-pentyl Alcohol and Acetone-Peroxide-T-pentyl Alcohol Mix Raman spectra, the disappearing of R_3C-OH band and appearing of $(HO)C-O(OR)$ is clearly observed, at 910 cm^{-1} and 940 cm^{-1} respectively. The spectra were followed using a 514nm laser line.

2.3 CONCLUSIONS

A viable mechanism for the cyclic acetone-peroxide reaction, which is supported by Raman and NMR measurements and theoretical calculations, has been proposed. The three independent approaches provide results that are in good agreement with each other. The qualitative and quantitative Raman results confirm key portions of the proposed mechanism, such as the experimental kinetics pattern and its respective kinetic order. The splitting of the Raman vibrations indicates polymer growth in the acetone-peroxide reactions. Independent measurements from $^1\text{H-NMR}$ and $^{13}\text{C-NMR}$ and GC-MS were used to corroborate some intermediate structures in the reaction media, such as P_1 , P_2 and P_3 , which are the precursors of the cyclic products.

Chapter III

3. NOVEL UNCATALYZED SYNTHESIS AND CHARACTERIZATION OF DIACETONE DIPEROXIDE (DADP)

A novel method to synthesize diacetone diperoxide (DADP) from acetone and hydrogen peroxide without the presence of a catalytic agent is described. Previously reported syntheses used toluene sulfonic and *m*-sulfonic acid as catalyst. DADP was prepared with a purity of 99.99%. The melting point range (128.5-134.5°C) consistently agreed with this value. The success of the procedure strictly depends on controlling the ratio between acetone and hydrogen peroxide as well as the temperature of the reaction mixture. Purified crystalline DADP samples were characterized using nuclear magnetic resonance, Raman and infrared spectroscopies, differential scanning calorimetry, gas chromatography and Open Atmosphere Chemical Ionization mass spectrometry. Structural evidence was compared to the well-known cyclic trimer triacetone triperoxide (TATP). The proposed synthetic scheme can be useful for preparing small amounts of the cyclic organic peroxide for characterization and fundamental studies and for formulation of gas chromatography, high performance liquid chromatography and mass spectrometry standards.

3.1 EXPERIMENTAL DETAILS

3.1.1 Reagents

American Chemical Society (ACS) grade acetone (99.7% purity) and hydrogen peroxide (ACS certified, 50% stabilized aqueous solution) were obtained from Thermo-Fisher Scientific International (Pittsburg, PA). Reagents were used without further purification. Ultra high purity

water (UHP, 18.2 MΩ) produced by a Barnstead Nanopure® system (Thermo-Fisher Scientific, Barnstead International, Dubuque, IA) was used for washing the crystals that precipitated during the acetone-hydrogen peroxide synthesis. Dichloromethane (CH₂Cl₂, 99.8%, stabilized for HPLC) was obtained from Acros Organics (Thermo-Fisher Scientific International).

3.1.2 Procedure

In an attempt to reduce the formation of the TATP, which is the predominant product of the reaction between acetone and hydrogen peroxide, and to isolate the linear polymer precursors of cyclic acetone peroxides [34], hydrogen peroxide and acetone were mixed in molar ratios of 1:2, 1:3 respectively giving the same yields in both cases. The temperature and time of reaction were such as is in the Scheme 3-1. To prevent evaporation of the solvent, a reflux condenser was placed over the reaction mixture and was kept at temperatures below room temperature. White crystals formed from direct gas phase condensation were washed and recrystallized using water and dichloromethane. Once purified, samples were characterized using differential scanning calorimetry (DSC), proton nuclear magnetic resonance (¹H-NMR), ambient pressure chemical ionization mass spectrometry (APCI-MS) and infrared (IR) and Raman spectroscopies.

3.1.3 Instrumentation

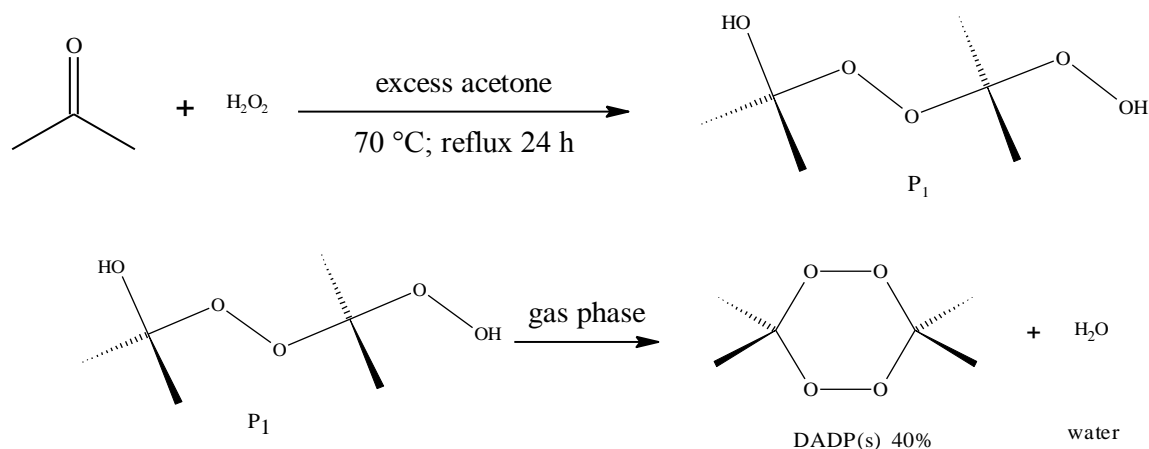
Characterization measurements were taken using various instruments. Vibrational spectroscopy was performed using Renishaw RM2000 and RM1000 Raman Microscope Spectrometer Systems, equipped with 514.5 nm and 532 nm laser excitation lines, respectively (Renishaw, USA, Chicago, IL). The FT-IR spectrometer used was a Bruker Optics model IFS 66v/S, equipped with a DTGS detector and a potassium bromide (KBr) beam splitter (Bruker Optics Inc., Billerica, MA). Nuclear magnetic resonance (NMR) conditions were as follows: For

acquisition of ^1H -NMR spectrum: CDCl_3 solvent, scan number or transients (NS): 16, spectral width (SWH): 10330.578 Hz and acquisition time (AQ): 3.172 s. For ^{13}C -NMR spectrum the conditions were: CDCl_3 solvent, NS: 4023, SWH: 30030 Hz and AQ: 1.09124, for this measurements an unshielded 500-MHz Bruker Avance, 2-channel broadband NMR Spectrometer complete with a 500-MHz Bruker magnet with an Avance DRX500 console (Bruker BioSpin, Billerica, MA). Gas chromatography analysis was performed using an Agilent GC 5890 equipped with a Supelco SPB-5 (5% biphenyl 95% dimethylsiloxane, C-18 column (15.0 m x 250 μm x 0.25 μm , Sigma-Aldrich, St. Louis, MO) and coupled to a 5790 mass selective detector (Agilent Technologies, Santa Clara, CA). The GC conditions were as follows: (I) Inlet: temp. 150°C; splitless mode; constant gas flow. (II) Oven: initial temp. 80°C; ramp 10°C/min; final temp. 230°C; carrier gas: Ultra high purity helium (Praxair Puerto Rico B.V., Gurabo, PR). Mass Spectrometry measurements were taken using an atmospheric pressure ionization mass spectrometer model JMS-T100 DART™ coupled to the AccuTOF-LC™ (JEOL, Peabody, MA). The thermal analysis was performed using a Q10 Differential Scanning Calorimeter (DSC TA Instruments, New Castle, DE). Ultra high purity nitrogen (Praxair Puerto Rico) and the following parameters were used for the DSC experiments: 5.0 mg in high-pressure hermetic pans and a heating rate of 5 °C/min.

3.2 RESULTS AND DISCUSSION

The formation of TATP instead of DADP in the synthesis reported by Wolffenstein [2] and Milas and Golubovic [8] and later modified by Swern et al. and Peña et al. [35, 6] is mainly a result of the low aqueous solubility, low polarity and high vapor pressure of the polymeric precursors (P_2 , P_1) of each acetone peroxide cyclic product, according to the mechanism proposed in the chapter 2. (See Scheme 3-1 and Figures 3-1 and 3-2) [35]. The precursor

structures can form terminal hydrogen bonds, which would prevent the formation of the respective acetone peroxide cycle or the alkoxy-peroxide cyclocondensation reaction. However, as the chain grows, this interaction becomes weaker and the effect on the aqueous solubility is lowered. This makes the P_2 structure curl up favoring the cyclization and formation of TATP rather than DADP. The uncatalyzed synthesis of DADP from acetone and hydrogen peroxide can be possible either by changing solvent polarity or transporting the precursor to the gas phase, then promoting the cyclization reaction [35]. In fact, the formation reaction of DADP reported here occurs in the gas phase. The most probable hypothesis to explain this event entails that P_1 is dragged to the gas phase by the high vapor pressure gas due to the high vapor pressure of acetone and then closes the cycle to form DADP (C_1) in the presence of an excess of acetone. To corroborate this hypothesis, GC-MS analysis of the gas phase (Scheme 3-1 and Figures 3-1) was performed, which effectively showed that acetone and P_1 are the main constituents of the gas phase at an estimated concentrations of 36% and 60% respectively based on the normalization areas of chromatographic peaks [36-37]. These concentrations were calculated based on the ratio of the peak areas. The gas sample to GC analysis was collected directly from gas phase so: sealing the entire system and using a GC-syringe of 100mL was extracted a representative sample of the gas phase of DADP reaction, and then it was injected into the GC-MS.



Scheme 3-1. Structures of: **(a)** General view of DADP formation reaction. This is a two-step reaction: P₁-formation (liquid-phase reaction) and DADP-formation (gas-phase reaction); **(b)** P₁ precursor of cyclic acetone peroxide dimer (C₁, DADP); **(c)** P₂ precursor of cyclic acetone peroxide trimer (C₂, TATP).

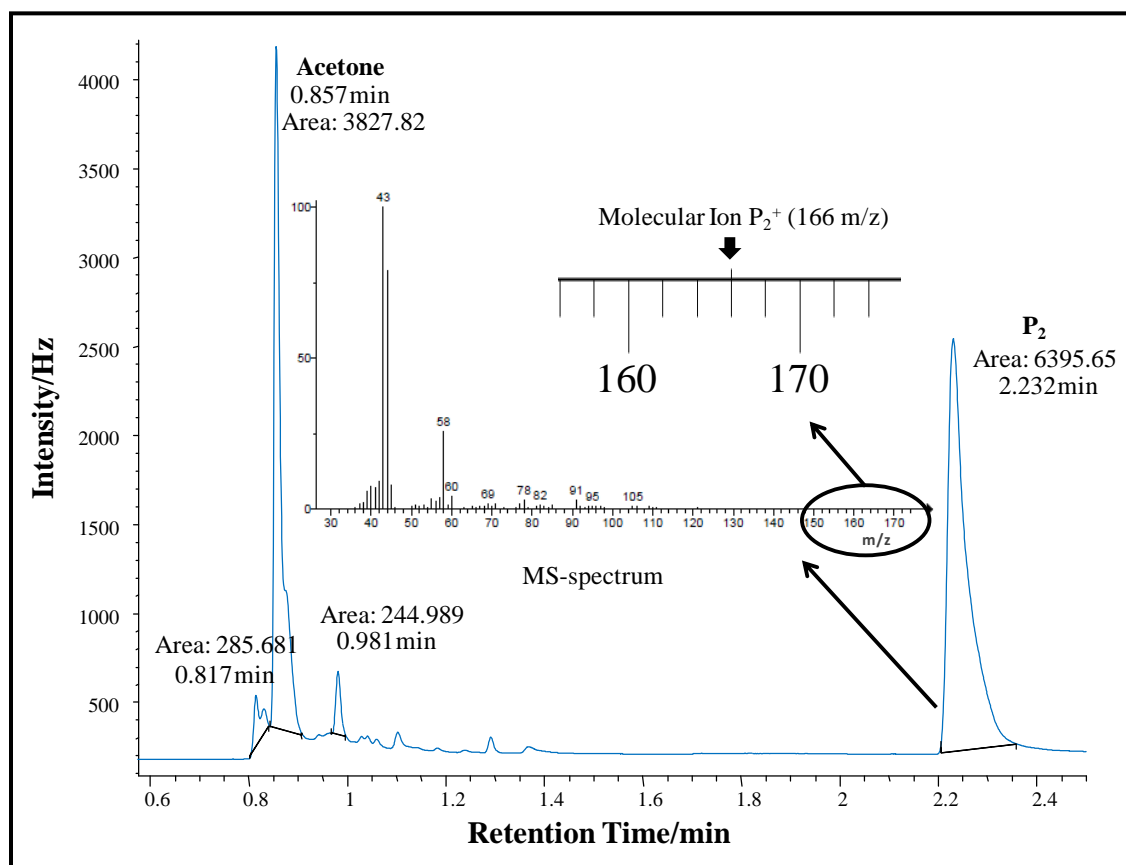


Figure 3-1. Gas chromatograph and electron impact mass spectrum of a sample of the gas phase were the DADP formation reaction takes place. The two main peaks at 0.86 min and 2.2 min are related to acetone and P₁, respectively.

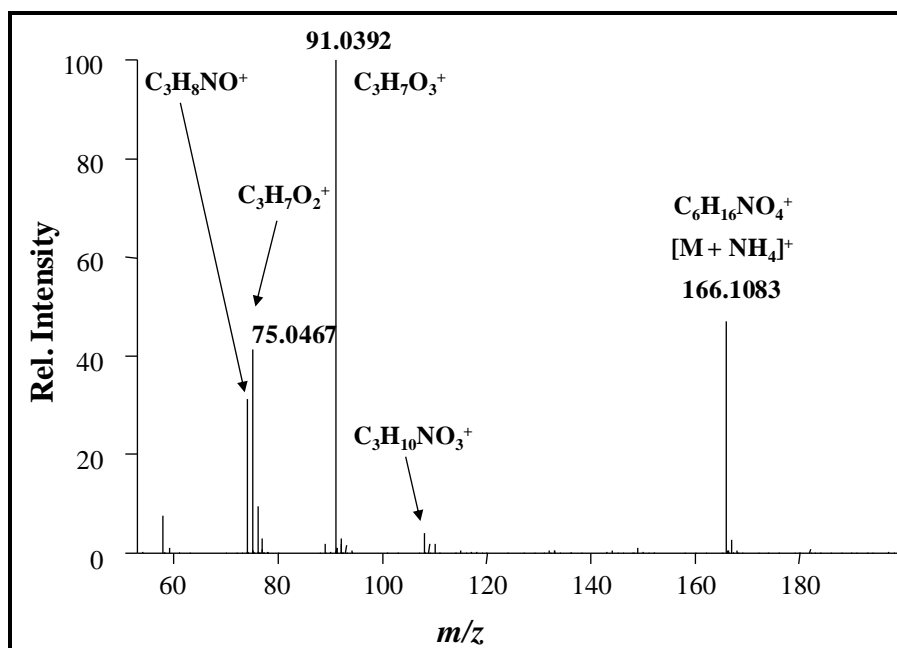


Figure 3-2. Positive-ion DARTTM mass spectrum of an isolated crystal assumed to be DADP. Ammonium hydroxide headspace vapor provided a source of NH₄⁺ to form ammonium adducts in a He gas stream used for open air chemical ionization MS.

The molecular ion intensity showed in the Figure 3-1 is very low due to the fact that these compounds are highly thermally unstable and their using GC/MS detection is very difficult [12]. Acetone, DADP and TATP standards solutions in acetone were previously analyzed to assign the identity of the chromatogram peaks. The reaction efficiency was about 40% with a yield of 80-120 mg in all tested assays. The purity of the obtained crystal was calculated based on the ratio of the normalized peaks areas [36-37], for a 10 min gas chromatographic run under same conditions as shown in Fig. 3-1. The peaks areas were 1.35×10^6 and 1.90×10^2 for DADP and other impurities. These areas are in the ratio of 7100:1 or 0.001%. On the other hand, the presented method was compared to the other recognized catalyzed methods, by showing better results in terms of purity [34]. Another important aspect is that the TATP compound, a principal contaminant in many acetone peroxide syntheses was not formed. It is evident that this uncatalyzed synthesis is cleaner than other reported methods (see Figure 3-3.).

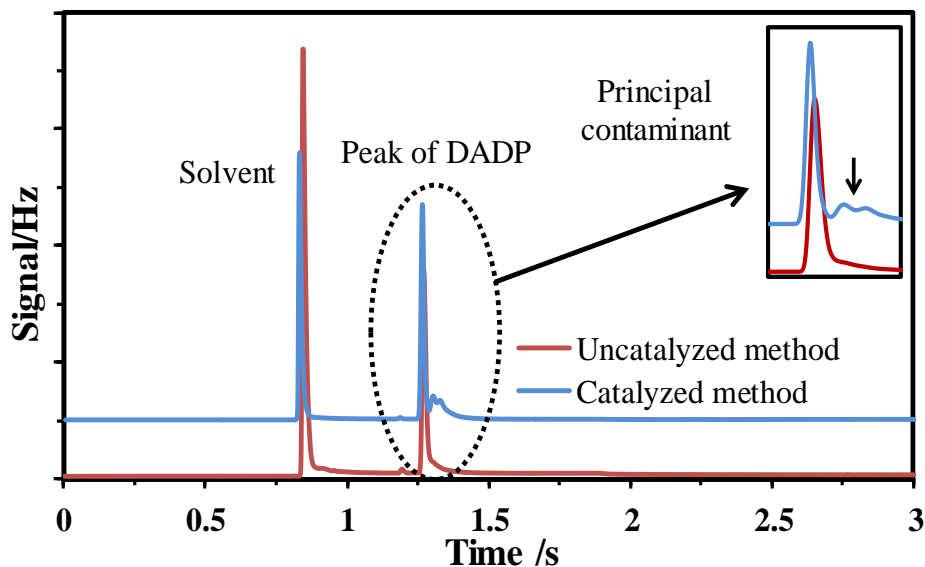


Figure 3-3. GC-analysis of the uncatalyzed and catalyzed method. The uncatalyzed is cleaner chromatogram compared to catalyzed one.

3.2.1 Raman and FT-IR Results

Proposed mechanisms for the acetone peroxide reaction all suggest that the intermediate species of the synthesis are open-chain structures with terminal hydroxide (O-H) and peroxide (-O-O-H) functional groups [11, 17, 32]. The presence of these linear structures in the isolated crystals can be ruled out since FT-IR and Raman spectra do not show O-H stretching vibrations ($\nu_{\text{O-H}}$) between $3400\text{-}3600\text{ cm}^{-1}$ (see Figs. 3-4a and 3-4b). However, the Raman vibrational spectrum obtained resembles that of DADP much more closely than the spectra of other cyclic organic peroxides that were published by Peña et al. In addition, the reaction that forms the compound under study occurs in the gas phase. Formation of TATP and other heterocyclic peroxides of higher molecular weight take place in condensed phase; hence, we discard such the possibility of TATP formation and that of higher oligomers [6, 33].

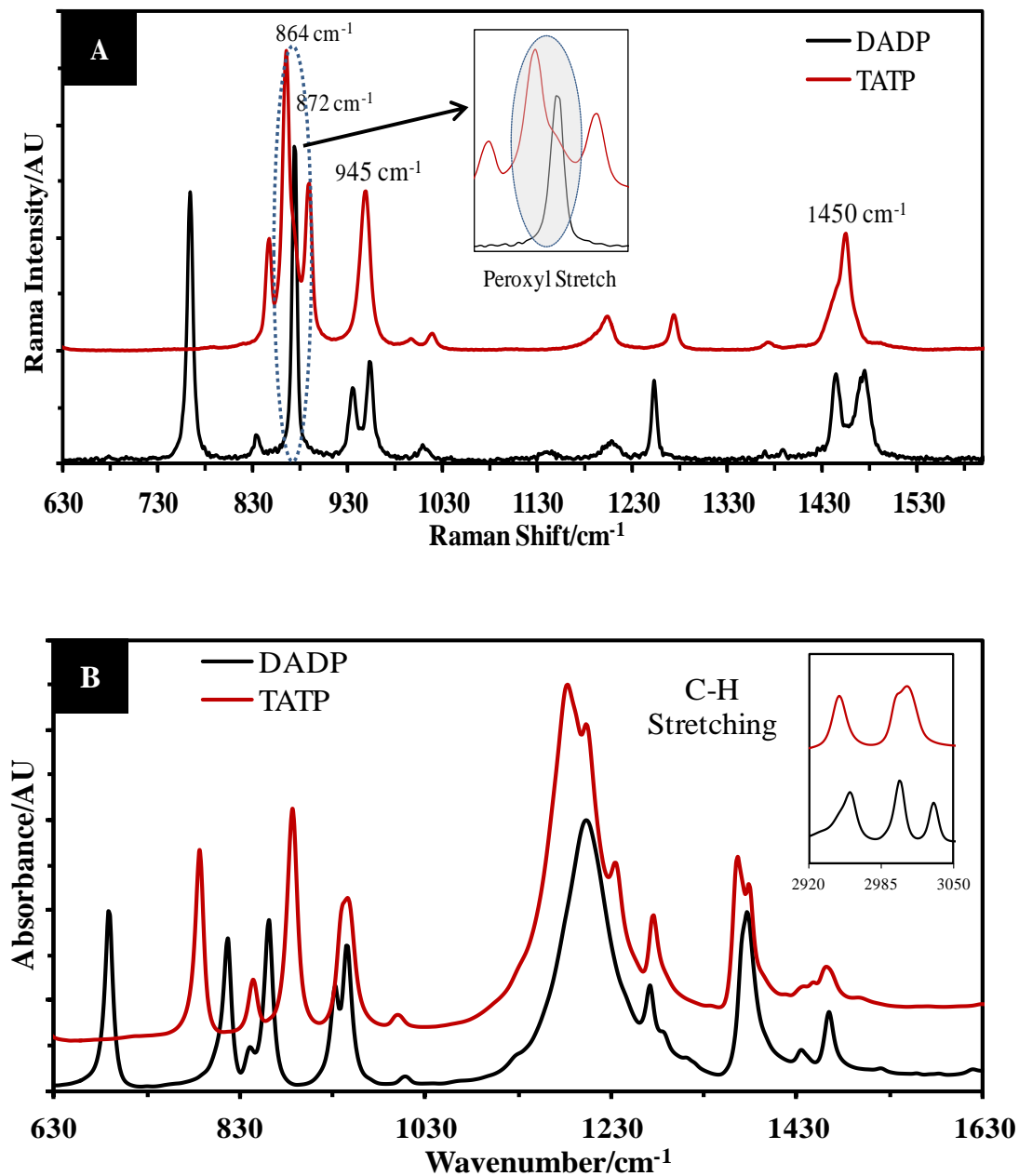
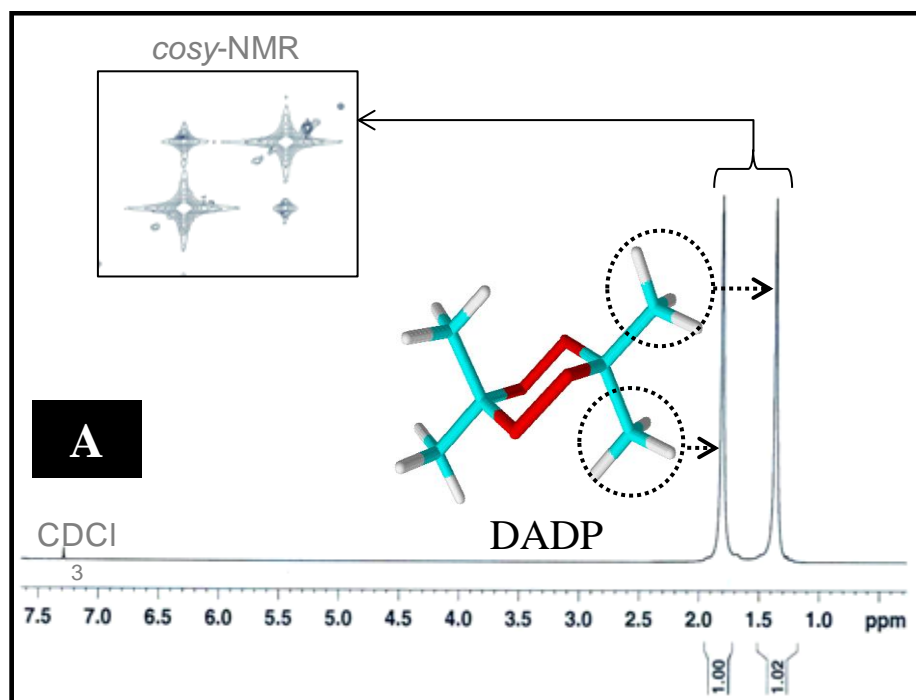


Figure 3-4. (a) Raman spectra of DADP and TATP in the fingerprint region, at a 514 nm excitation line; (b) FT-IR spectra of DADP and TATP.

3.2.2 ¹H-NMR, ¹³C-NMR and COSY-NMR Results

The ¹H-NMR and ¹³C-NMR spectra reveal several resonances that correspond to the methyl groups, proving they exist in different environments in the molecule. The two-

dimensional nuclear magnetic resonance correlation spectroscopy (COSY-NMR) spectra consistently show that these groups are attached to the same type of C-atom. The difference in the environment of the methyl moieties is mainly due to the dissimilar proximities to the oxygen core of the molecule, which contains four peroxide oxygen atoms. The downfield $^1\text{H-NMR}$ shift corresponds to the methyl group closest to the electron cloud of this core (see Figs. 3-4a and 3-5b). In the $^1\text{H-NMR}$ spectrum of TATP a single peak was observed. This is strong evidence that points to the direction that methyl groups in TATP are equivalent while in the DADP structure they are not. The NMR spectra were run both in proton-exchangeable and in non-proton exchangeable solvents. The same spectra were obtained in all cases. This result reaffirms what we previously observed in the FT-IR spectrum of DADP.



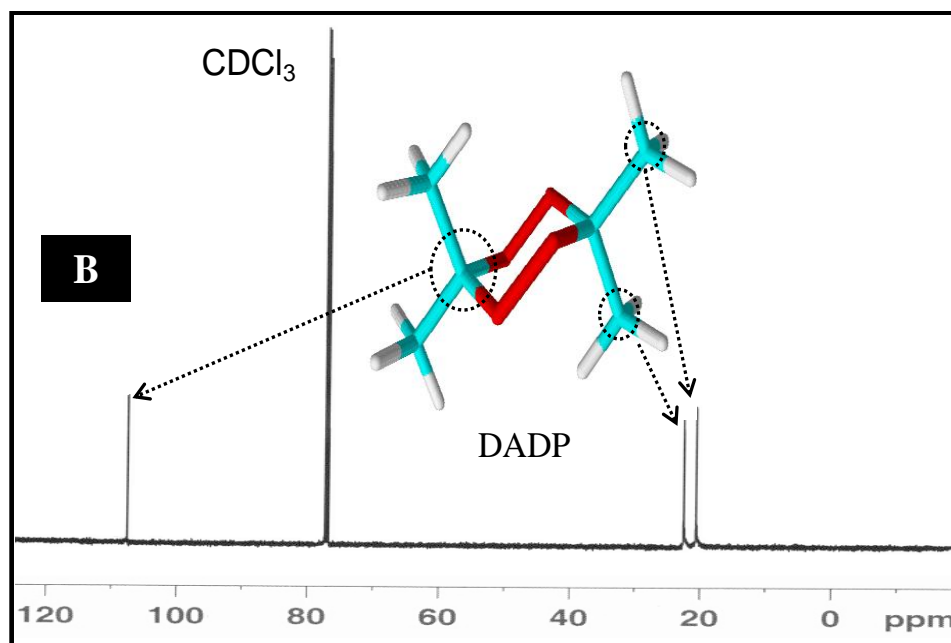


Figure 3-5. (a) ^1H -NMR and COSY-NMR spectra of DADP in CDCl_3 ; (b) ^{13}C -NMR spectrum of DADP in CDCl_3 solvent.

3.2.3 Direct Analysis in Real Time (DARTTM) Mass Results

Several attempts to achieve a successful MS analysis of DADP by conventional MS methods (electron impact ionization) were carried out. Efforts directed to measure the molecular ion were unsuccessful due to the thermal instability of cyclic organic peroxide compounds, even after optimizing the GC conditions to reduce thermal breakdown of DADP. The results were best obtained by Open-Air Chemical Ionization-MS using a JEOL Direct Analysis in Real Time (DARTTM) Time-of-Flight Mass Spectrometer, which can be used for positive ion and negative ion detection of gases and liquids. The sample was analyzed in the positive ion mode. For measurements, a source of ammonium hydroxide was placed adjacent to the DARTTM gas stream to form positive ammonium ion adducts. As shown in the Figure 3-2, it was possible to detect the positive ammonium molecular ion $[\text{M-NH}_4^+]$, and all fragments confirmed the structural identity of the crystals isolated by the synthetic route. The major thermal decomposition fragment

($C_3H_7O_3^+$) was also detected in the analysis of the ammonium TATP adduct using DART™ at higher gas temperatures, which suggests that acetone peroxide heterocycles have similar fragmentation patterns [38].

3.2.4 DSC Results

Another method to confirm the identity of a compound beyond chemical and spectroscopic methods is through physical constant measurements, including the melting point. The melting point was consistently found to be 128.5-134.5°C for crystalline samples of isolated DADP and the boiling range was 153-166°C. This value reflects the high purity of the crystals obtained, when compared to the melting point reported by Matyas et al., which was 130-147°C [9]. An example of the typical thermogram obtained is illustrated in Figure 3-6. To corroborate the boiling point, a sample of evaporated DADP at 170°C was analyzed by FT-IR, effectively confirming that second DSC peak is due to the boiling of DADP and not the decomposition, because at this temperature DADP still preserves its identity after being melted (first DSC-peak). Even, at 250°C the compound decomposes partially in acetone and others unidentified products (See Figures 3-7a and 3-7b).

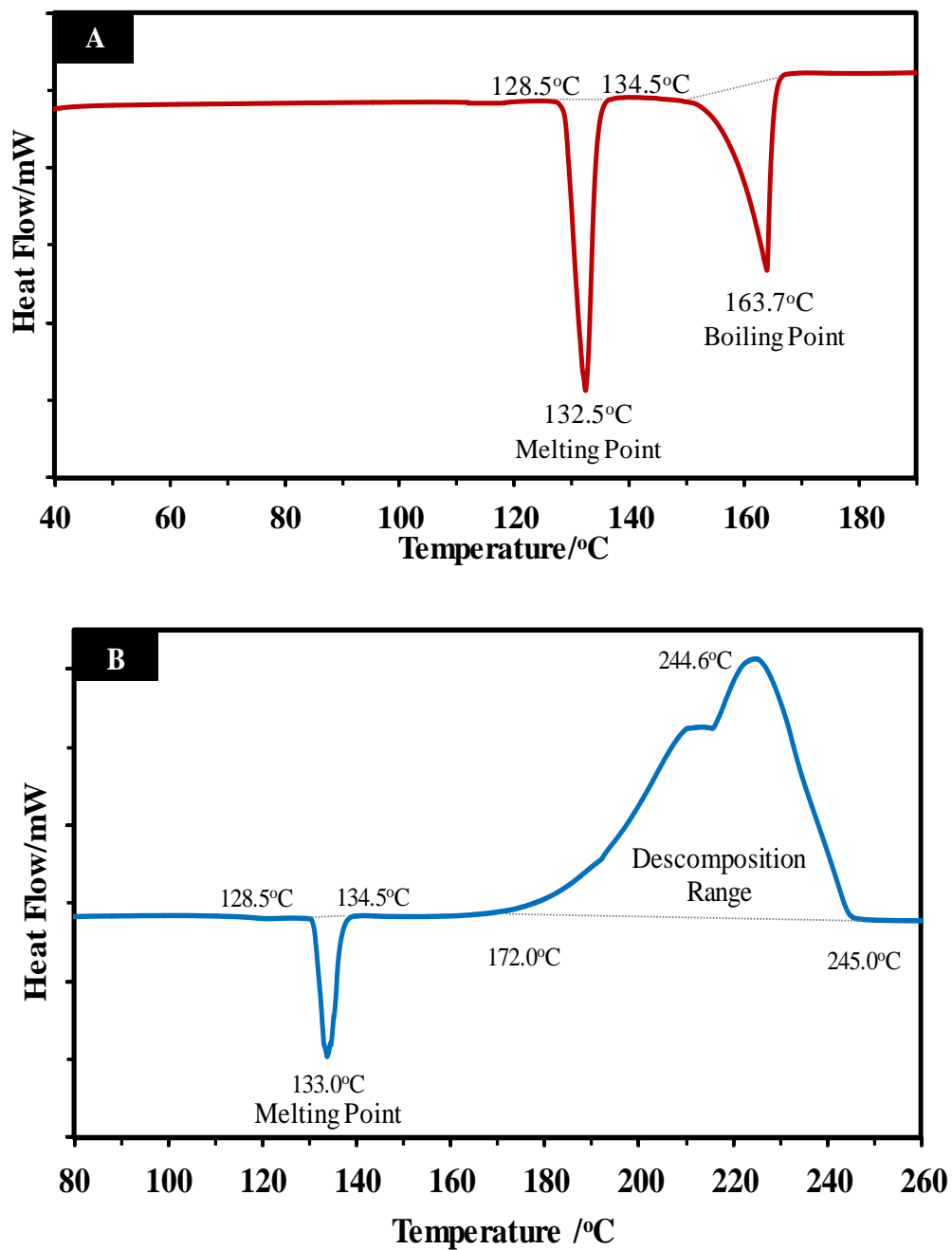


Figure 3-6. DSC thermogram of 5.0 mg of isolated crystals of DADP, at a scan rate of 5 °C/min, using (a) non-hermetically sealed pan and (b) hermetically sealed pan.

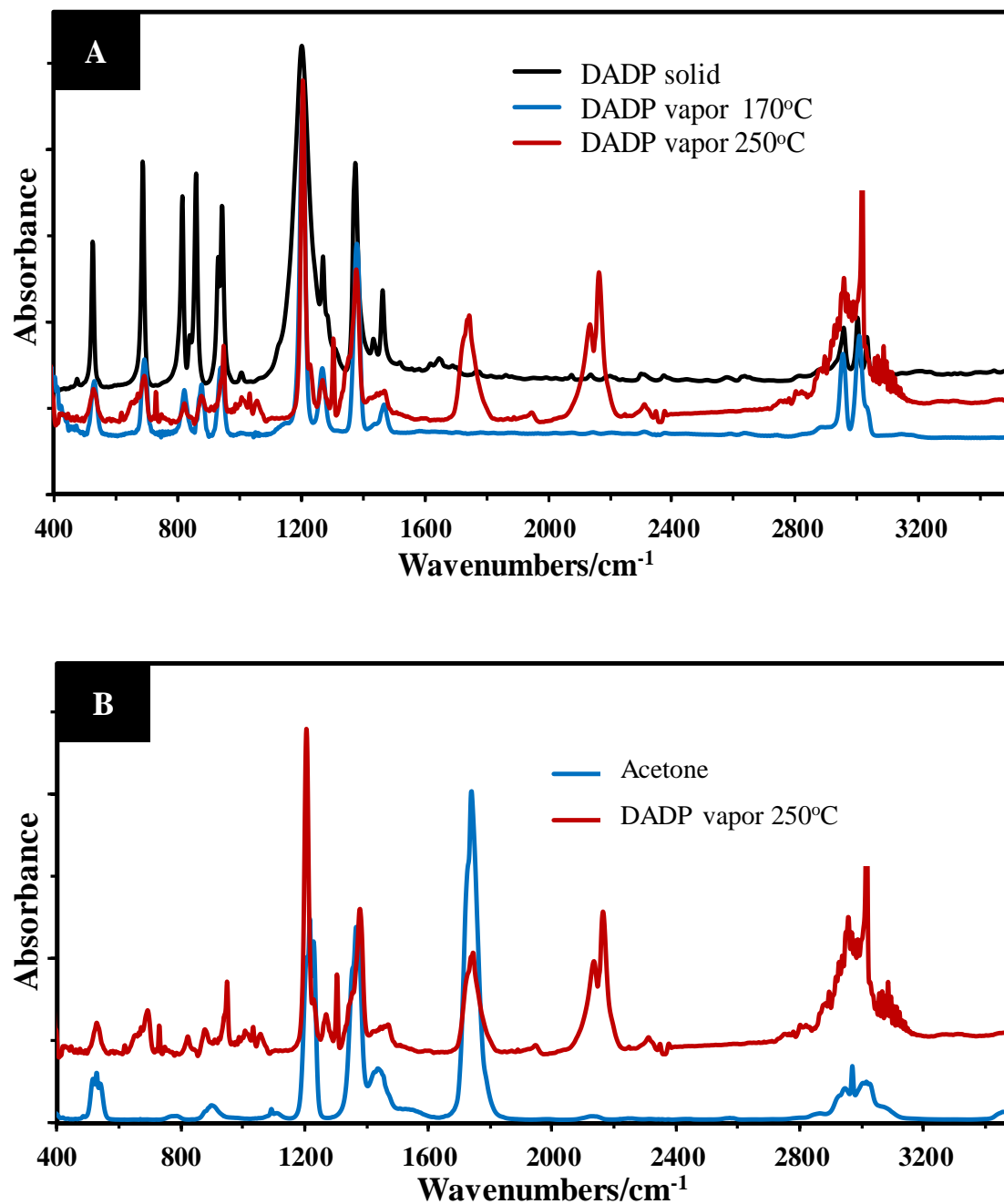


Figure 3-7. FT-IR spectra of DADP gas at 170°C and DADP partial decomposition at 250°C compared to (a) DADP solid and (b) acetone.

3.2.5 Theoretical Analysis

Prior to this work, viable pathways for the acetone-peroxide reaction leading to cyclic products such as DADP and TATP were proposed. In all the mechanisms proposed cyclization

was visualized as occurring via alkoxy-peroxyl condensation reactions. Experimental results were consistent with DFT calculations. These results were the basis for the analysis of the uncatalyzed reaction of DADP presented above [34]. Figure 3-8 shows the optimized structure and molecular electrostatic potential (MEP) contour map for DADP and The Figure 5-6 shows the MEP contour map for TATP. The MEP was calculated in order to visualize differences on the adjacent methyl groups in both structures. The molecular geometries were optimized at density functional theory (DFT) level of theory using the Beck's three-parameter modification [19] of Lee-Yang-Parr [20] hybrid functional (B3LYP) and 6-311g++(d, p) [21] basis sets. Gaussian 03™ software package [22] was used for these calculations. The MEP was calculated using Hyperchem for Windows software (Hypercube, Inc., Gainesville, FL) [39]. Large differences in the chemical environment among the adjacent methyl groups bonded to the same carbon atom are noted in the eclipsed-DADP structure, because one of them interacts stronger than the other with the four-oxygen core atoms (i.e., electric field line numbers one and three, moving from the outside in toward the nucleus). In others words, one of CH₃ groups is more influenced by the negative electrostatic potential of either the peroxyl electronic cloud or the four-oxygen core atoms. This theoretical result is in agreement with experimental results as the two ¹H-NMR shift by 1-2 ppm for the adjacent methyl groups (Figures 3-5a and 3-5b). The vibrational signals observed at 945 cm⁻¹, 1450 cm⁻¹ and 3000 cm⁻¹ (Figures 3-4a and 3-4b) in TATP are singlets [40] while they split into doublets for DADP, evidencing once more that in the TATP structure, all the adjacent methyl groups are equivalent (Figure 3-8) and in DADP the chemical environment is different for the two sets of CH₃. The negative and positive potential lines are illustrated by the minus and plus symbols, respectively.

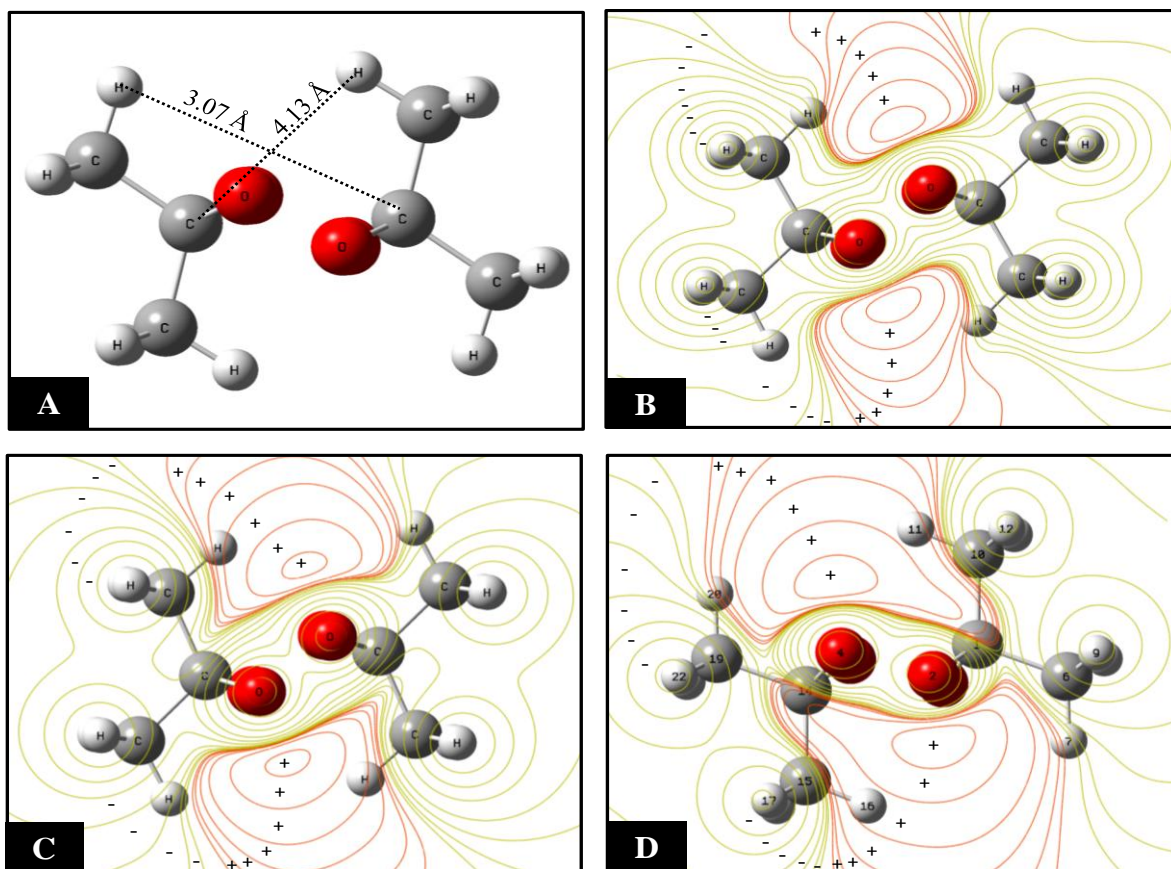


Figure 3-8. (a) Optimized structure of DADP at DFT level of theory and B3LYP-6-311-g++(d, p) basis set. (b), (c) and (d) MEP or cross section of potential electrostatic distribution from inner to outer four oxygen core, these MEP's were calculated using GaussView® 5.0.8

3.3 CONCLUSIONS

All previously reported syntheses of DADP involve the use of a catalytic agent. In this work, it was possible to prepare DADP at 99.99% purity without a catalyst, which is a promising result to advance in the field of analytical standards for GC, HPLC and MS calibrations. Characterization studies were successfully completed and the high-purity crystals were successfully identified as DADP. Theoretical calculations and experimental results strongly agree with each other. The proposed synthetic route can be used to prepare very small amounts of high-purity DADP that can be used for the preparation of standards or for trace method development for applied studies.

Chapter IV

4. THERMAL PROFILE OF HOMEMADE PEROXIDE EXPLOSIVES

This chapter deals with theoretically-supported non-linear thermal fittings, to determine sublimation enthalpies of cyclic organic peroxides explosives using thermogravimetry analysis and FT-IR grazing angle techniques. TGA and FT-IR-GA experiments consisted in the determination of mass loss rate at several isothermal points. The sublimation and decomposition enthalpies values were comparable with previously reported and calculated other methods. Amino peroxide explosives showed a different profile from acetone-peroxides explosives. In this field of study, it is typical to calculate the vapor pressure from rate constant values using the Langmuir equation and then fit the obtained values according to Clausius-Clapeyron equation to find standard enthalpy values. The proposed method is direct because, it resulted from fitting rate constant of sublimation (K_{sub}) vs. temperature without assuming values for certain constants of the Langmuir equation. R^2 values of the fittings obtained were all above 0.999+, which indicates a high level of acceptance. This thermal analysis was done in a wide range of temperature and at a temperature step of 1°C/point generating remarkable tendencies with many points.

4.1 THEORETICAL BACKGROUND

This section describes the mathematical derivation of the equation used in the fitting of the experimental thermal data. In detail, it was converted the Langmuir equation (Eq.4-1) in an equation similar to Clausius-Clapeyron equation in its differential form. Then, it was resolved for

the pressure, applying natural logarithm to both sides, and finally differentiating the resultant expression with respect to the reciprocal temperature equation 4-2 was obtained.

On the other hand, replacing the enthalpy as a function of temperature the previously studied by Chickos et al. [41] in the Clausius-Clapeyron equation, and then equating the resulting expression to the differential equation 4-2 a differential equation was obtained in terms of the sublimation constants and temperature (Eq. 4-3). Finally, solving this differential equation the final equation was obtained to be used in the fitting of the experimental data (Eq. 4-4). The enthalpies values were calculated using Equation 4-5.

$$k = \frac{dm}{dt} = p\alpha \sqrt{\frac{M}{2\pi RT}} \quad 4 - 1$$

$$R \frac{\partial \ln p_{(T)}}{\partial (1/T)} = R \frac{\partial \ln k_{(T)}}{\partial (1/T)} - \left(\frac{R}{2}\right) \left(\frac{1}{T}\right)^{-1} \quad 4 - 2$$

$$R \frac{\partial \ln k_{(T)}}{\partial (1/T)} = -(\Delta H_0 - 298.15\Delta C_p) - (\Delta C_p + 0.5R) \left(\frac{1}{T}\right)^{-1} \quad 4 - 3$$

$$R \ln k_{(T)} = -a \left(\frac{1}{T}\right) - b \ln \left(\frac{1}{T}\right) + c \quad 4 - 4$$

$$\Delta H_T = a + (b - 0.5R)T \quad 4 - 5$$

Where, ΔH is the enthalpy, R is the gas constant, $k_{(T)}$ is sublimation constant, C_p is the constant of absorption energy, M is the molar mass, and p is the pressure.

4.2 EXPERIMENTAL SETUP

4.2.1 Reagents

Solid samples of homemade peroxides explosives studied (TATP, DADP, HMTD and TMDD) were synthesized and purified in our laboratory at 99+% of purity. Reagents used for the

HME synthesis were obtained from Fisher Scientific International. UHP water (UHP, 18.2 MΩ) produced by a Nanopure® system, Barnstead International, Dubuque, IA (Thermo-Fisher Scientific) was used for washing precipitated HME crystals after synthesis.

4.2.2 Thermal gravimetric analysis (TGA) Measurements

The sublimation study consisted in the determination of mass loss rate at several isothermal points under the sample melting point and/or decomposition point. These measurements were carried out using a TA Instrument Q-500 Thermal Gravimetric Analyzer (TGA). The thermal conditions were as follow: (1) temperature range: 22.00 °C to 70.00 °C (for DADP and TATP) and 60.00 °C to 120.00 °C (for TMDD and HMTD). The temperature ranges were chosen according to melting and decomposition points for each explosive and non-explosive compounds in order to get meaningful results; (2) temperature programming: ramp 1.00 °C/min and then Isothermal for 20.00 min. A constant nitrogen purge of 60 mL/min was maintained through the TGA furnace. The TGA was calibrated for temperature using the nickel Curie point (630 K) and for weight according to manufacturer's optimized procedures. All HME samples were successfully analyzed by TGA at different temperature ranges. To minimize the effect of the area in the mass loss rate constant, the crystalline samples were well macerated.

4.2.3 FT-IR Grazing Angle Measurements (FT-IR-GA)

Mid-IR spectroscopy operating at the grazing angle of incidence is the most sensitive optical absorption technique available for measuring low chemical concentrations on surfaces [42]. The following experimental setup was used to determine the spectral area loss rate for each HME sample smeared on stainless steel metal surface thermally controlled at several isothermal points. The area covered by HME film was 52 cm². The FT-IR-GA measurements were performed with a Bruker Vector 22 infrared spectrometer coupled to a MIR-optic fiber. Grazing-

angle probe used carefully aligned mirrors to deliver the mid-IR beam to the sample surface at the grazing angle (approximately 80° from normal), to collect the reflected beam and to return it to a mid-IR detector (a cryo-cooled, MCT detector). The experimental conditions were: **(1)** spectral range: 4000-700 cm⁻¹, **(2)** spectral resolution: 4-cm⁻¹, temperature range: 16-40°C and **(3)** the spectral ranges analyzed were: 1389-1290 cm⁻¹, 1224-954 cm⁻¹ and 955-902 cm⁻¹. HMTD and TMDD were not analyzed by FT-IR GA, because their solubility in organic solvents is too low to obtain a smeared film detectable by this method.

4.3 RESULTS AND DISCUSSION

The methods based on thermogravimetry analysis and Langmuir and Clausius-Clapeyron thermal expression to determine thermodynamic properties have demonstrated to be accurate for many ideal materials and proof of this are the countless publications that report consistent thermodynamic data based on this technique [43- 46]. However, it was necessary to evaluate and standardize the experimental setup using standard materials previously studied, while ensuring the accuracy and reliability of our results. For this purpose, benzoic acid and *m*-nitrobenzoic acid compounds were used, by showing excellent results, in terms of, the coefficients of determination (R^2) values of the fittings, which were over 0.999+ and accurately of the respective sublimation standard enthalpies values, which were highly comparable to previously reported [46-50] (Figures 4-1a and 4-1b and Table 4-1). The thermal analyses were done in a wide range of temperature and short temperature step of 1 °C/point in order to generate accurate trends.

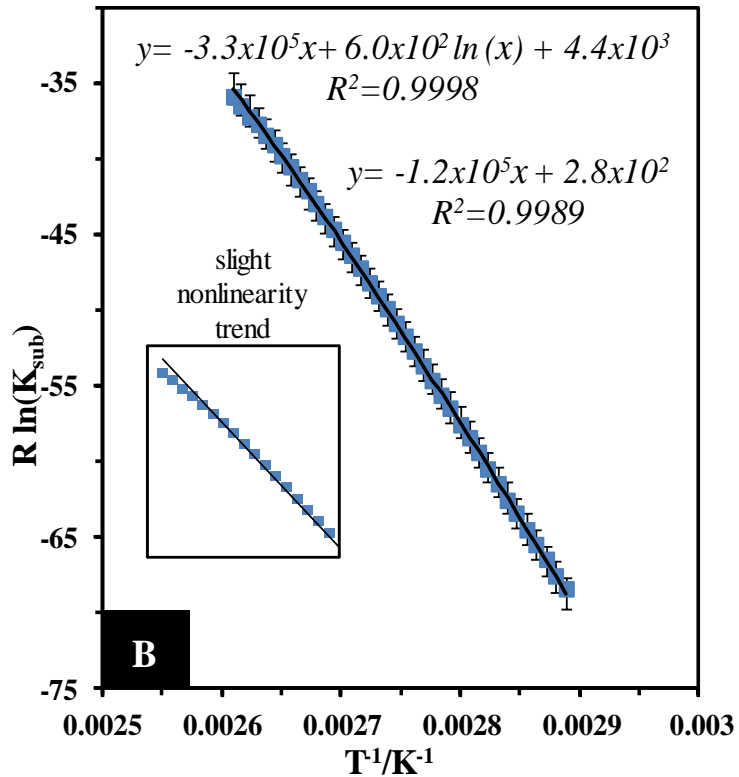
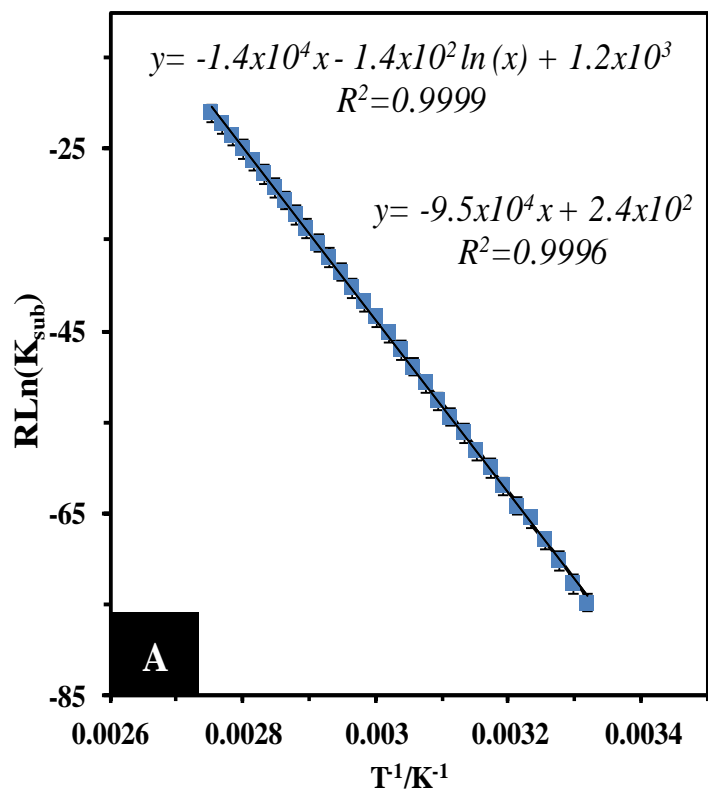


Figure 4-1. Non-linear thermal fitting of the experimental data for: (a) benzoic acid and (b) acetylsalicylic acid (ASA). Temperature range: 60-100°C. Temperature step: 1°C/point.

Table 4-1. Sublimation enthalpies of standard nonexplosive compounds at 298.15K. These values were determined considering a linear and nonlinear fitting. Benzoic and *m*-Nitrobenzoic acid showed a well-defined linear trend.

Author/Method		$\Delta H_{\text{SUB}}/\text{KJmol}^{-1}$ (At 298.15K)	
		Benzoic acid	<i>m</i> -Nitrobenzoic acid
Our work	Linear fitting	94.8 ± 0.3	113.7 ± 0.5
	Non-linear fitting	93 ± 6	110 ± 5
Santos et al [44]		94 ± 3	----
Monte et al [43]		90 ± 2	----
Ribeiro da Silva et al [45]		----	110.0 ± 0.4

4.3.1 Thermal Profile of HME Compounds

In this field of study, it is typical first, to calculate the vapor pressure from rate sublimation constant values using the Langmuir equation and then to fit the pressure values according to Clausius-Clapeyron equation in order to determine standard enthalpy values, assuming that the enthalpy change (ΔH) is a thermodynamic property independent of the temperature. Sometimes this approach works well for ideal compounds and in narrow ranges of temperature. However, in cases such as that of Rojas-Aguilar et al., in which they reported several ΔH_{sub} values for benzoic acid at different temperatures, specifically $86.8 \pm 0.5 \text{KJmol}^{-1}$ at 333.15K and $88.5 \pm 0.5 \text{KJmol}^{-1}$ at 298.15K [48] demonstrates that the enthalpy change is a temperature-dependent function. Well-defined, non-linear thermal behavior of HME, both for homemade acetone-peroxide explosives (HAPE) such as TATP and DADP and for homemade amino-peroxide explosives (HAMPE) such as HMTD and TMDD are reported. Some non-explosives compounds such as *m*-nitrobenzoic acid also showed a slight nonlinearity trend with R^2 values higher than linear fittings, similarly to the results reported by Chatterjee et al. for hydroxy-benzoic acid (see Fig. 4-

1b) [51]. Even, linear trends well defined showed either equal or better R^2 values when they were fitted according to equation 4-4 (see Fig. 4-1a). The non-linear method is direct because, it results from thermal fitting of the sublimation constants (K_{sub}) without assuming arbitrary values for some adjustment constants. The remarkable nonlinear behavior of the HAPE compounds may be due to significant changes in the heat capacity values (ΔC_p) of the studied transition, given that these compounds are more energetic than non-explosive materials. Figures 4-2a-b and 4-3a-b clearly show the curvature of the experimental data. Indeed, the mathematical result states that the curvature of this thermal function is due to the logarithmic term, and this term is proportional to ΔC_p , value. So that physically, the nonlinearity behavior seems to depend on the heat capacity change [24]. Even straight lines showed significant values of ΔC_p , when they were fitted according to nonlinear equation. In general, this behavior becomes more prominent when considering wider temperature ranges. On the other hand, the FT-IR GA results were consistent with thermal trend found with TGA. The R^2 values found with the spectroscopic method were lower than TGA method, because the methods based on thermogravimetry (with four significant figures in mg units) are more precise and accurate than sample smearing followed by fiber optic coupled grazing angle probe FT-IR measurements (Figs 4-2b, 4-3b and Table 4-2). HMTD and TMDD were not analyzed with the FT-IR GA method, because detectable film could not be prepared using sample smearing due to their low solubility in organic solvents.

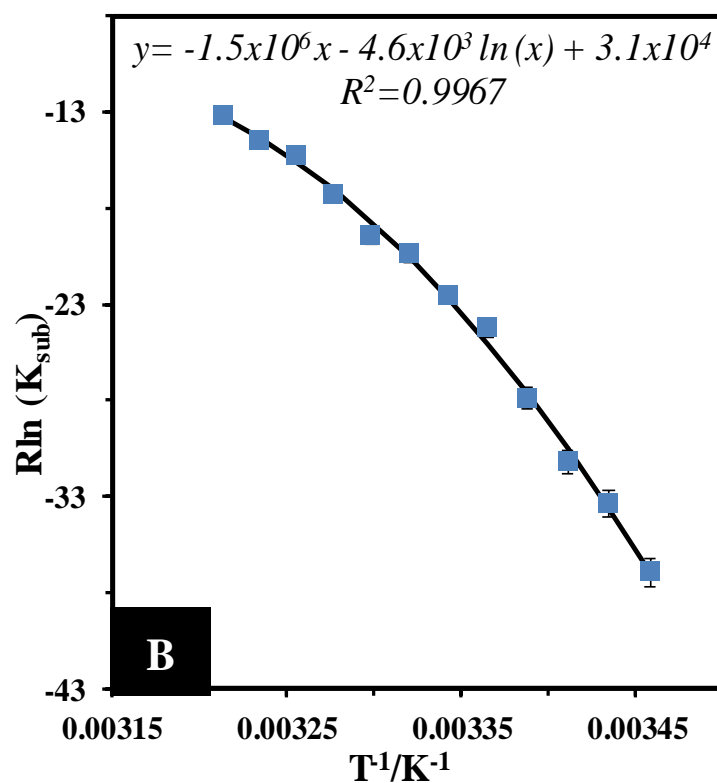
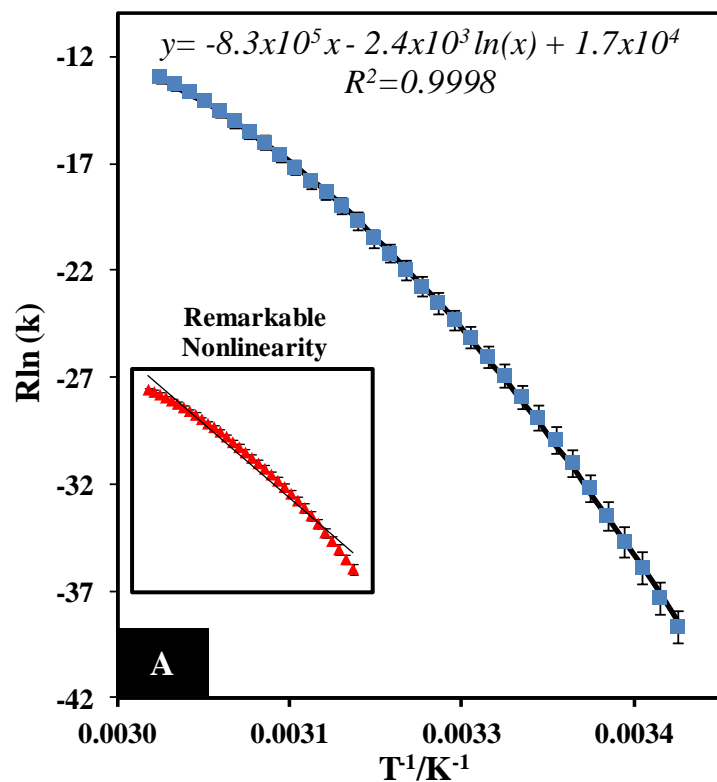


Figure 4-2. Non-linear thermal fitting of the experimental data for DADP using: (a) TGA and (b) FT-IR GA. Temperature range: 60-100°C. Temperature step: 1°C/point. The experiments were run several times in order to ensure the marked trends.

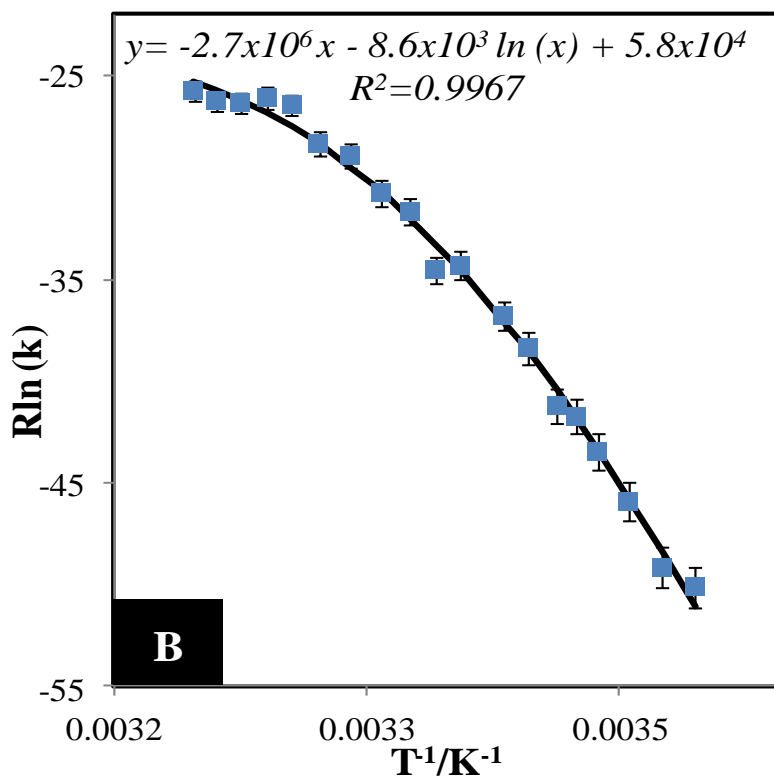
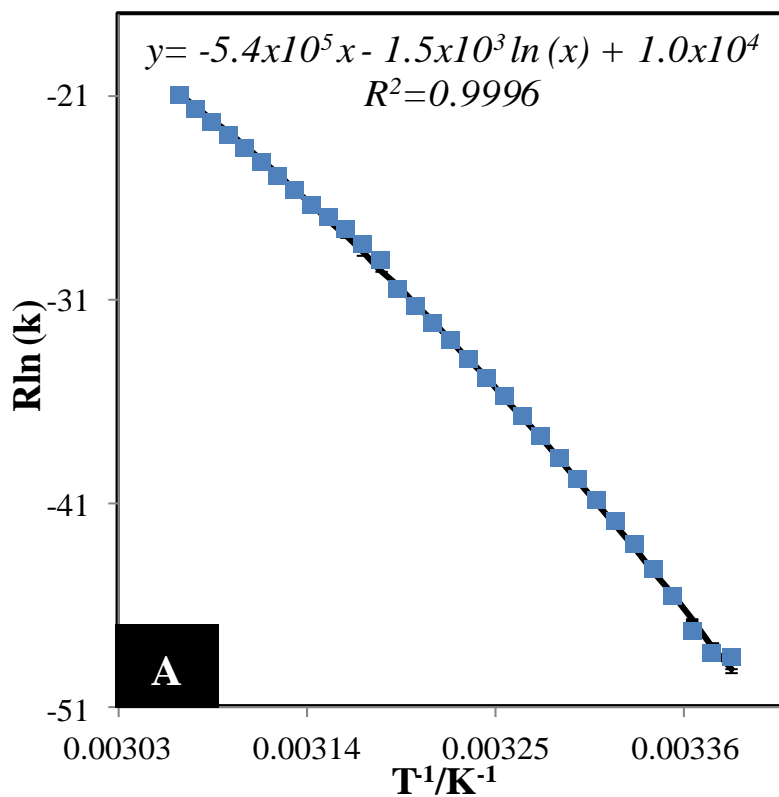


Figure 4-3. Non-linear thermal fitting of the experimental data for TATP using: (a) TGA and (b) FT-IR GA. Temperature range: 40-80°C. Temperature step: 1°C/point. The experiments were run several times in order to ensure accurate trends.

Table 4-2. Sublimation enthalpies of the homemade peroxide explosives at 298.15K. These values were determined considering a nonlinear fitting. --- Not calculated

Author/Method		$\Delta H_{\text{SUB}}/\text{KJmol}^{-1}$ (At 298.15K)		$\Delta H_{\text{Decomp}}/\text{KJmol}^{-1}$ (At 298.15K)	
		DADP	TATP	HMTD	TMDD
Our work	TGA	106.2 ± 0.2	103.8 ± 0.3	-290.9 ± 0.8	-283.9 ± 0.9
	FT-IR GA	105 ± 2	102 ± 2	----	----
Oxley et al [50]		82	104	----	----
Ramírez et al [52]		----	85	----	----
DSC		----	----	-325	-332

4.3.2 Thermal Profile of HAMPE Compounds

Although, the mass loss rates of HMTD and TMDD compounds showed a thermal profile different from those of TATP and DADP, their rate constants could be fitted according to the equation 4-4, giving exothermic enthalpy rather than endothermic. This result suggests that the mass loss of these compounds is due to two processes: decomposition and evaporation and that the rate constant relating both thermal events can be calculated (see Figures 4-4a-b). In order to confirm this hypothesis, a FT-IR spectrum of the vapor phase was taken at the temperature range studied, by corroborating that the mass loss is not only through sample evaporation. In fact, Oxley et al. previously reported that the vapor pressure of HMTD could not be determined due to its reduced thermal stability in vapor phase. As a confirmatory note, in the GC chromatogram of the HMTD vapor phase some peaks related to decomposition products rather than neat HMTD were observed [52]. On the other hand, Hiyoshi and Nakamura proposed that HMTD decomposes in condensed phase, figures 4-5a-d show the FT-IR spectra of the vapor and the solid phase of HME. Large differences are appreciable in the spectra of TMDD and HMTD compounds, while the DADP and TATP compounds retained their identity in the vapor phase.

Identification of the decomposition products is beyond the scope of this research and will be considered in future work. To establish a reference point, the decomposition enthalpy value obtained with the TGA method was compared to the determined with differential scanning calorimeter (DSC) method showing acceptable and comparable results in terms of magnitude order (for more details see Table 4-2). The discrepancy in the enthalpy values for TMDD and HMTD may be due to that, in the TGA experiment, decomposition and sublimation processes occur, while the DSC method only measured the decomposition enthalpy. In short, amino-peroxides compounds followed a coherent thermal behavior different from acetone-peroxide group. Each experiment was carefully measured several times and in short temperatures steps ($1^{\circ}\text{C}/\text{measurement}$) to avoid reporting erroneous data.

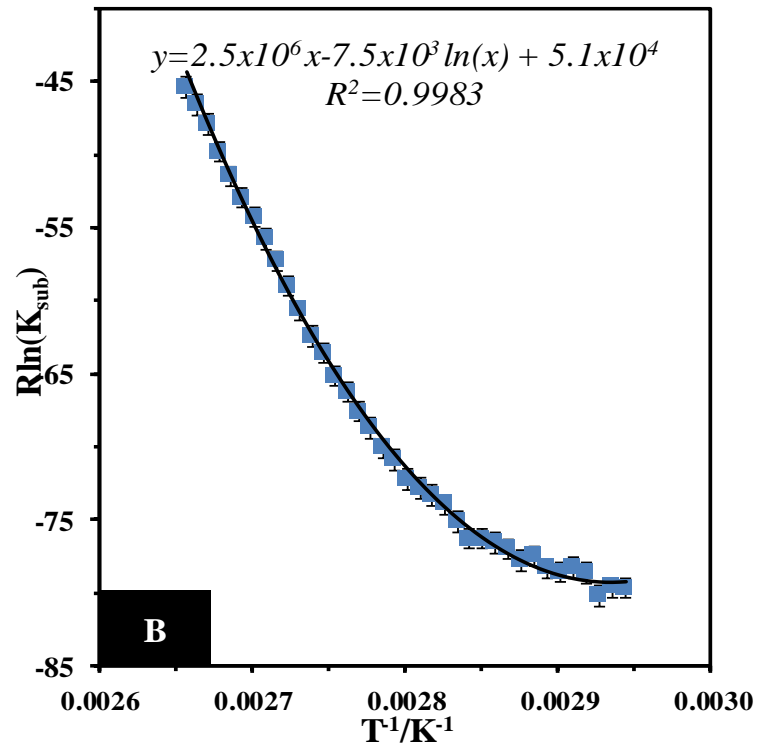
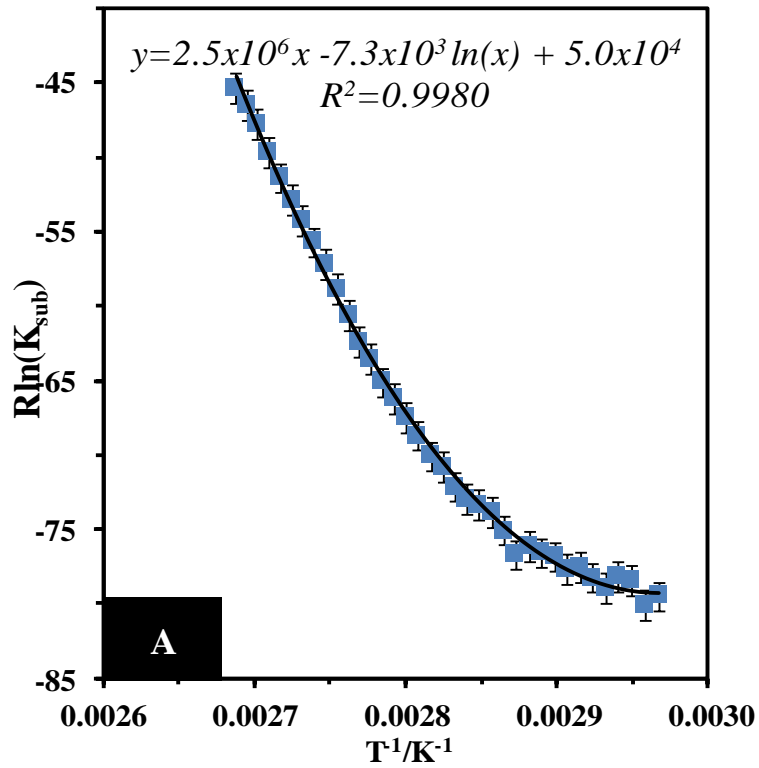
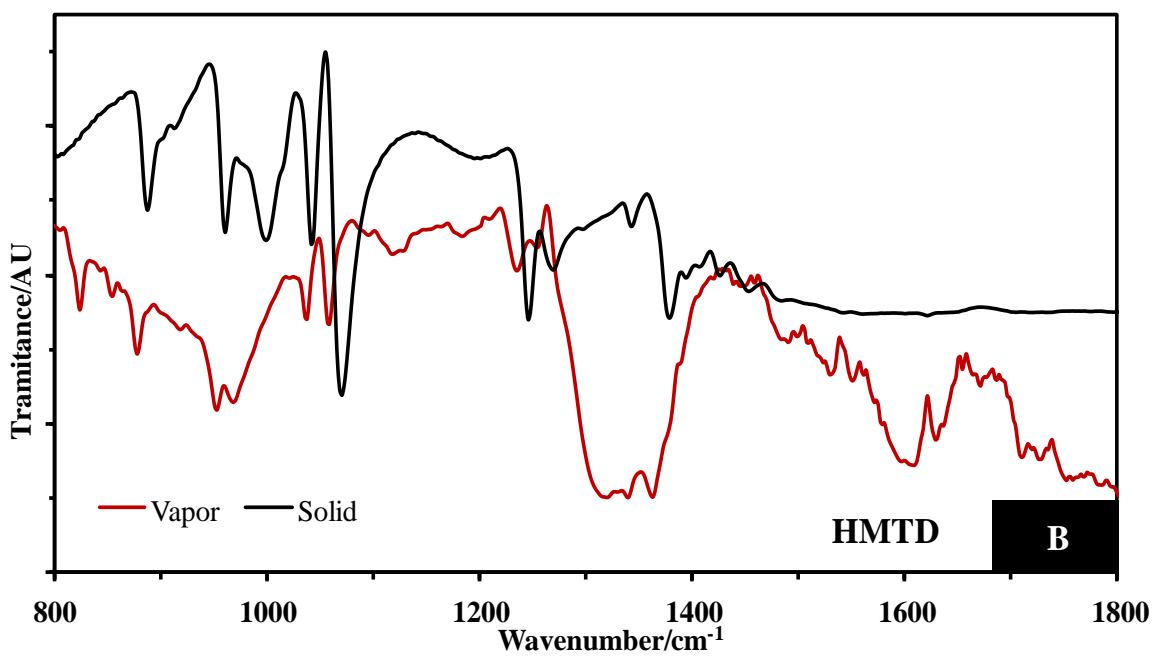
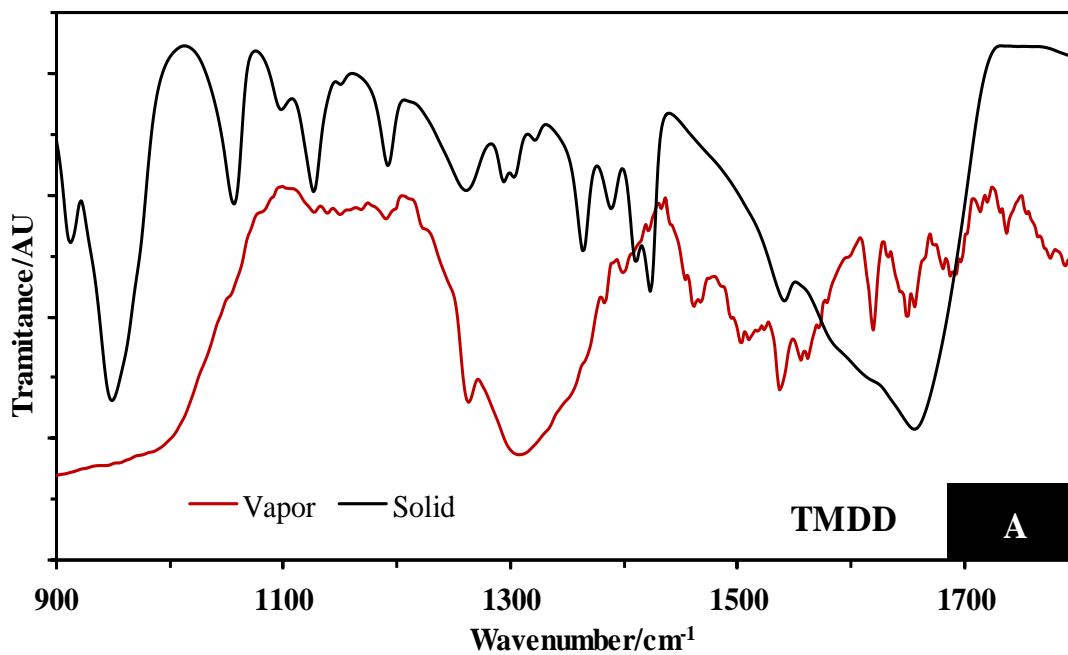


Figure 4-4. Non-linear thermal fitting of the experimental data for: (a) TMDD and (b) HMTD using TGA. Temperature range: 60-100°C. Temperature step: 1°C/point. The present trends are truly marked.



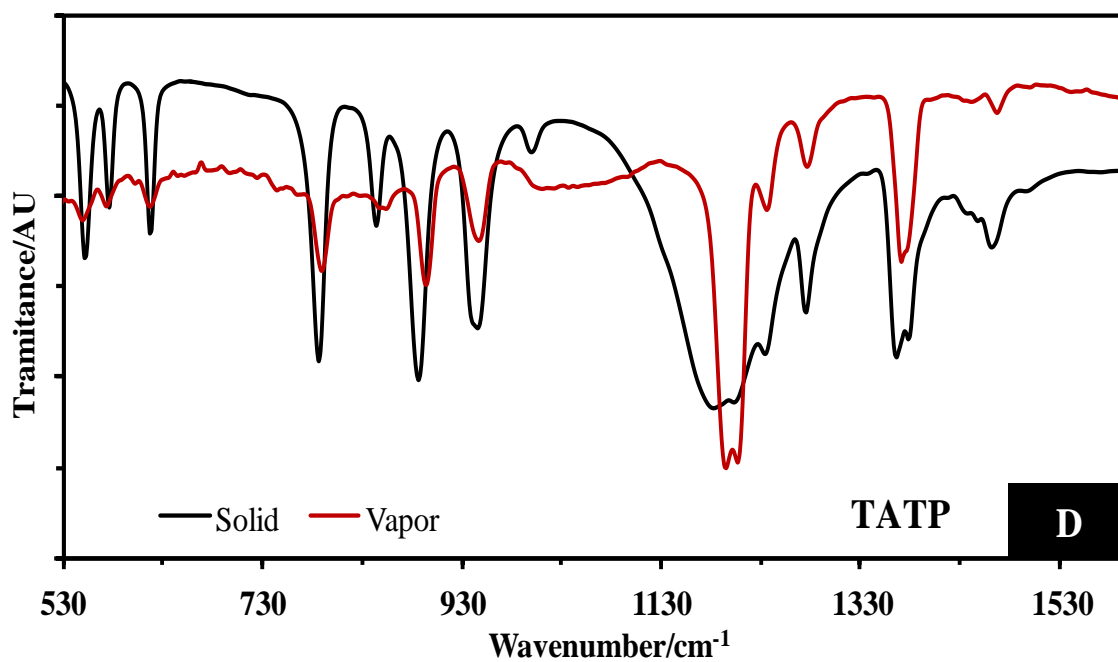
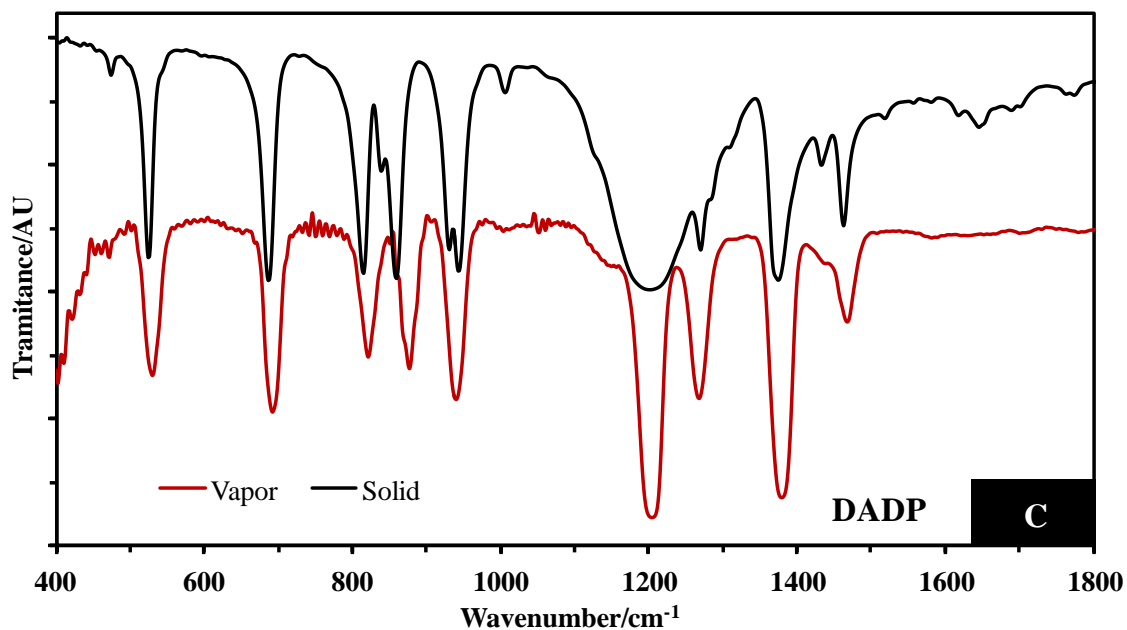


Figure 4-5. FT-IR spectra of the solid and vapor phases of: (a) TMDD, (b) HMTD, (c) DADP and (d) TATP. The vapor phase sample was taken at the temperature range studied. HMTD and TMDD effectively decomposed in the vapor phase while DADP and TATP not.

4.4 CONCLUSIONS

The results demonstrate that experimental setup was in optimal conditions to perform the thermogravimetry measurements, so that the reported data is reliable. HAMPE compounds showed thermal profiles different from HAPE because, HAMPE are decomposing while evaporating. The experimental thermal trends were measured several times showing consistent data with high R^2 values. Even, linear trend could be fitted according to the equation 4 with R^2 higher or equal to the linear fit. The sublimation and decomposition enthalpies values were comparable with previously reported and calculated by other groups and different experimental approaches. FT-IR spectra of the implied phases in the physicochemical change proved that HAMPE compounds decomposed and evaporated at the same time, while HAPE compounds only sublimated.

Chapter V

5. SPECTROSCOPIC AND PHYSICAL EVIDENCE OF ISOLATED D₃-TATP AND C₂-TATP CONFORMERS

A simple method to isolate both D₃-TATP and C₂-TATP conformers is presented. The proposed method involves multistep recrystallizations using solvents of different polarities and heating to boiling. The solvents used were methanol, cyclohexane and acetonitrile, all at high levels of purity. Spectroscopic and physical measurements such as: Raman spectra, X-ray diffraction and melting point showed that both clear and opaque crystals are different conformations of TATP. An experimental value for the transition energy between both conformers using the Raman shifts was calculated.

5.1 EXPERIMENTAL SETUP

5.1.1 Reagents

Certified ACS acetone, 99.7% purity, hydrogen peroxide stabilized and certified in 50% aqueous solution, HPLC grade acetonitrile, cyclohexane and methanol and sulfuric acid certified ACS-Plus 90-98% purity were obtained from Fisher Scientific International. Ultra high purity water (UHP, 18.2 MΩ) produced by a Nanopure® system, Barnstead International (Thermo-Fisher Scientific) was used for washing precipitated TATP crystals after synthesis.

5.1.2 Instrumentation

Raman spectra were acquired using the following conditions: spectral range: 100- 3200 cm⁻¹; accumulations: 2; acquisition time: 10 s; laser power levels: 10-60 mW; excitation lines: 532 nm laser line of Spectra-Physics, solid state diode laser system. For these measurements

Renishaw RM2000 and RM1000 Raman microspectrometers were used. IR spectra were acquired in an IFS 66v/S Bruker Optics interferometer, equipped with a DTGS detector and a potassium bromide (KBr) beam splitter. Nuclear magnetic resonance (NMR) spectra were collected using an unshielded 500 MHz Bruker Avance, 2-channel broadband NMR Spectrometer complete with an Avance DRX500 console (Bruker BioSpin, Billerica, MA). The thermal analysis was performed using a Q10 TA Instruments differential scanning calorimeter (DSC). Ultra-high-purity nitrogen and high-pressure hermetic pans were used for the DSC experiments (TA Instruments, New Castle, DE). The X-ray diffraction spectra of crystal samples were collected using a Bruker D8 diffractometer with an X-ray source: $\text{CuK}\alpha$ at 44 kV/40 mA. The sample was in polycrystalline state.

5.1.3 Synthesis Details

TATP was synthesized using the modified synthesis of Milas and Golubovic [8], which consists of an acid-catalyzed reaction of ketones with hydrogen peroxide at low temperature. In detail, acetone and hydrogen peroxide (1:1 molar ratio) are separately cooled between 0 °C and -5 °C. Then, a small amount of a strong acid: HCl, H_2SO_4 or $\text{CH}_3\text{SO}_3\text{H}$ was carefully added to acetone as a catalytic agent. Finally, hydrogen peroxide was added dropwise to prevent uncontrolled violent reactions that liberate high amounts of energy. Afterwards, the white powder of TATP was washed, recrystallized and dried several times using different solvents such as: cyclohexane acetonitrilo, methanol, dichloromethane among others up to get well-defined clear or opaque crystal (see Figure 5-1). The multistep recrystallizations were done by dissolving and then heating to boiling. In some cases, it was not possible to obtain well-defined crystals due to low solubility. Another method to obtain different TATP conformers is using different

acids as catalyst in the formation reaction, but the obtained crystals samples are not pure enough to characterize them by reported methods [53].

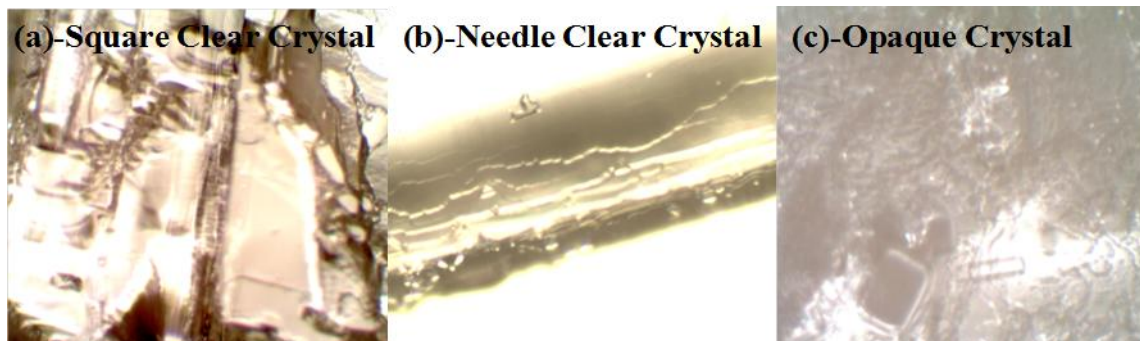


Figure 5-1. Microscopic picture of the: (a) square clear crystal, (b) needle clear crystal (D_3 -TATP structure) and (c) opaque crystal (C_2 -TATP conformer) at 10X.

5.2 RESULTS AND DISCUSSION

The uncatalyzed CAP reaction generally yields the D_3 -TATP conformer, which is a structure of lower energy than C_2 -TATP conformer and its crystalline appearance is assumed to be clear [54]. However, when using strong acid in the synthesis, an opaque crystalline precipitated is obtained, which is assumed to be the C_2 -TATP conformer. This result may be caused by large amount of energy released with strong acids, which gives way to the products of higher energy. The recrystallization process with methanol produced C_2 -TATP crystal because this solvent dissolves partially the TATP powder and the molecular interaction is weaker than with other solvents, by causing that TATP molecules do not assume the more stable and symmetric form (D_3) in solution previous to precipitation process. With solvents such as: dichloromethane, ACN and cyclohexane in which, the solubility is higher, TATP powder is easily dissolved and the formation of D_3 -TATP conformer is favored.

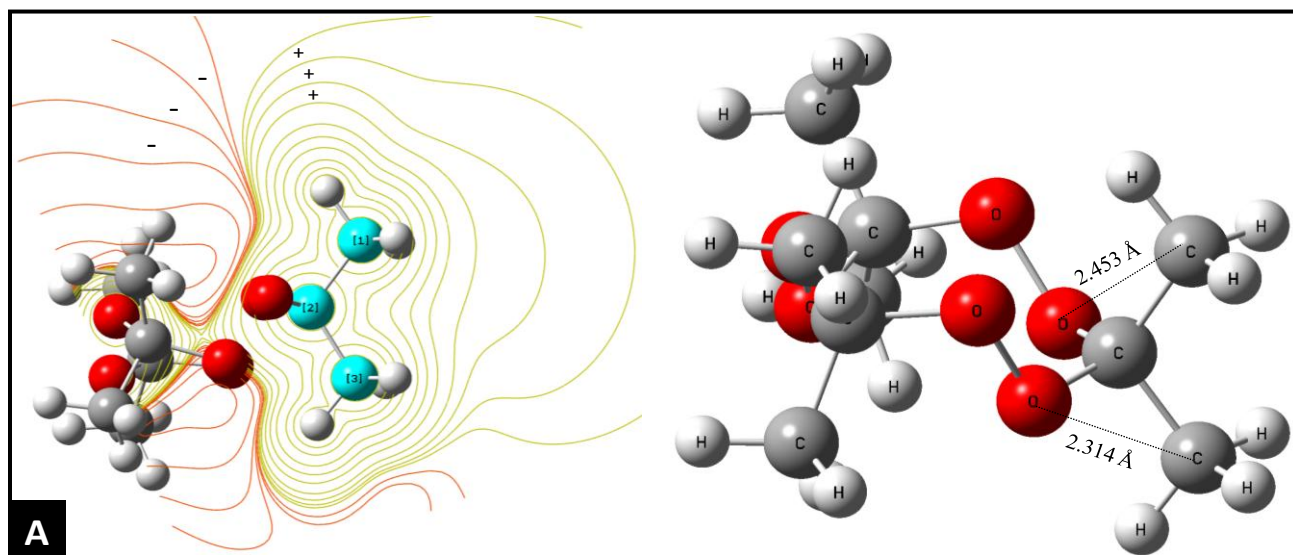
5.2.1 Raman and Computational Results

Significant differences are observed at first glance in the Raman spectra of the clear and opaque crystals, specifically in the bands that appear at 240 cm^{-1} , $300\text{-}320\text{ cm}^{-1}$, 550 cm^{-1} and 867 cm^{-1} . In the asymmetric stretching range of the C-H bond at 3018 cm^{-1} ($\nu^{as}_{\text{C-H}}$) a slight shift was observed which agrees to a minimal difference in the geminal methyl group environments of the C_2 -TATP structure compared to high symmetry D_3 -TATP structure.

Conformer structures were optimized at B3LYP/6-311g++ (d, p) [19-21]. The MEP cross section of the methyl groups clearly showed the similarity of the methyl tails in the D_3 -TATP structure, while in the C_2 -TATP structure are slightly different (see Figures 5-2a and 5-2b). In the symmetric stretching band at 3015 cm^{-1} no differences were observed. In general, these bands are not significantly affected by ring configurations (Figures 5-3a to 5-3e) [32]. In fact, the methyl region of the $^1\text{H-NMR}$ spectra only showed a single broadened peak (Figure 5-4) agreeing with Raman results.

At 300 cm^{-1} a larger shift was registered, since this spectral range is related to the ring torsion and breathing modes [55] and although, the bond connectivity is the same, the ring conformations are widely different in terms of energy for both conformers. In the O-O, C-C and C-O bond stretching regions were observed different patterns for each conformer spectra specifically at $864\text{ - }872\text{ cm}^{-1}$ range, C_2 -TATP spectrum showed three peaks while, D_3 -TATP showed four. Low vibrational shift ($\Delta\omega \sim 3\text{ cm}^{-1}$) was observed at peroxy stretching, because the peroxide bond is slightly polarizable, when compared to others chemical bonds. In fact, the difference observed between the DADP and TATP peroxy band is only 8 cm^{-1} being peroxy bonds stretching of different molecules (Figure 3-4a). The peroxy stretching band was corroborated using isotopic labeling compound. In detail, Figure 5-5 shows the Raman spectra of the TATP, TATP- $^{13}\text{C}_3$ and TATP- $^{13}\text{C}_6$ isotopomer. In them we can see that just one band was

unshifted, which appears at 867 cm^{-1} , because the oxygen atom was not isotopically labeled. In general, the bond energies are slightly affected by the conformational changes in the TATP oxoring, the bond energy displacement values were calculated based on the band shifts and the respective anharmonicity constant. On the other hand, a vibration at 817 cm^{-1} was found that is not common in both spectra (Figure 5-2c), which can be related to crystal lattice movement. Multiple measurements were done in order to corroborate these statements. The Raman spectra were run using two laser lines: 532 nm and 785 nm, by getting better resolved spectra with 785 nm one. The $^1\text{H-NMR}$ and $^{13}\text{C-NMR}$ spectra of a TATP solution, which is a mix of conformers, consistently showed a single wide peak corresponding to the two geminal methyl groups of both conformers, which have similar chemical environment (Figure 5-2 and 5-4).



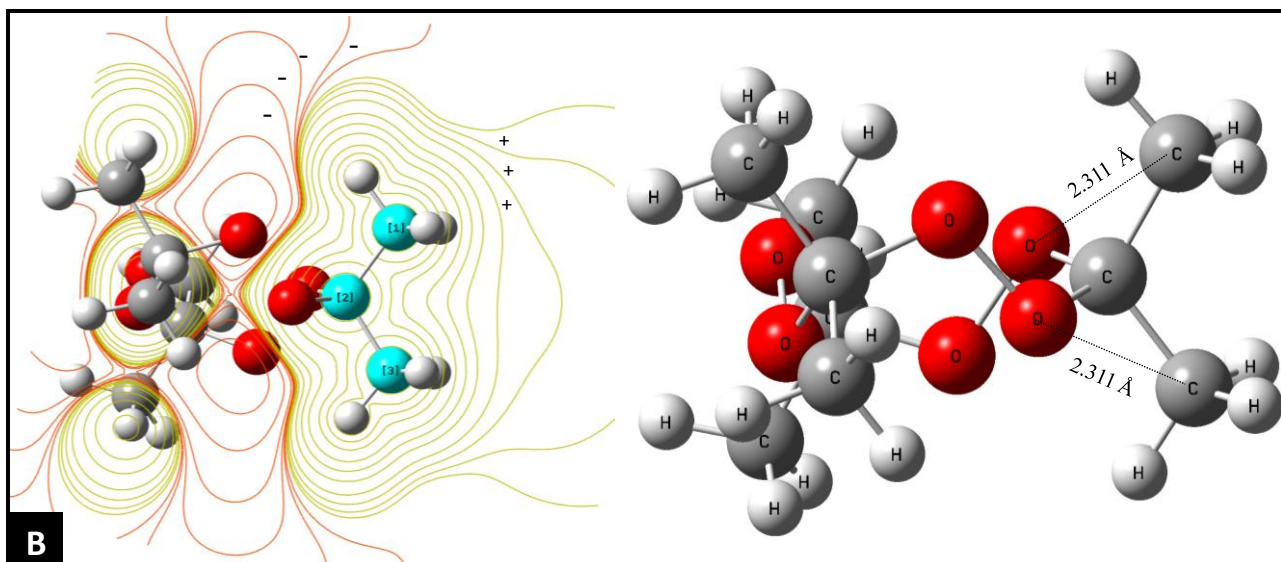
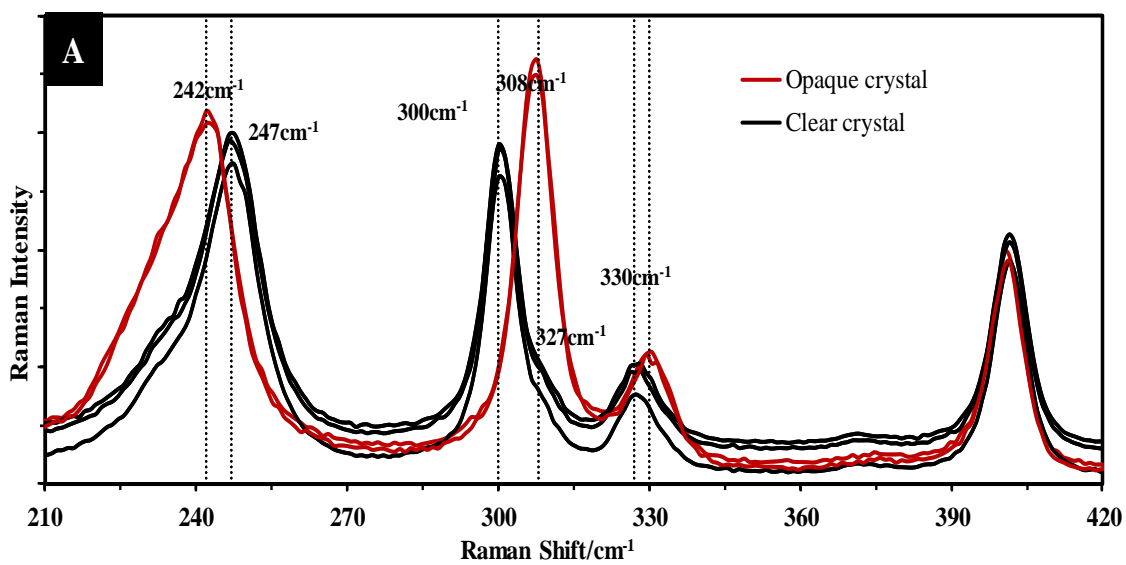


Figure 5-2. Optimized structure and a cross section of the electrostatic spatial distribution (MEP) of the gem-methyl groups illustrating the chemical environment of: **a)** C₂-TATP and **b)** D₃-TATP at DFT level and B3LYP/6-311++g (d, p) basis set.



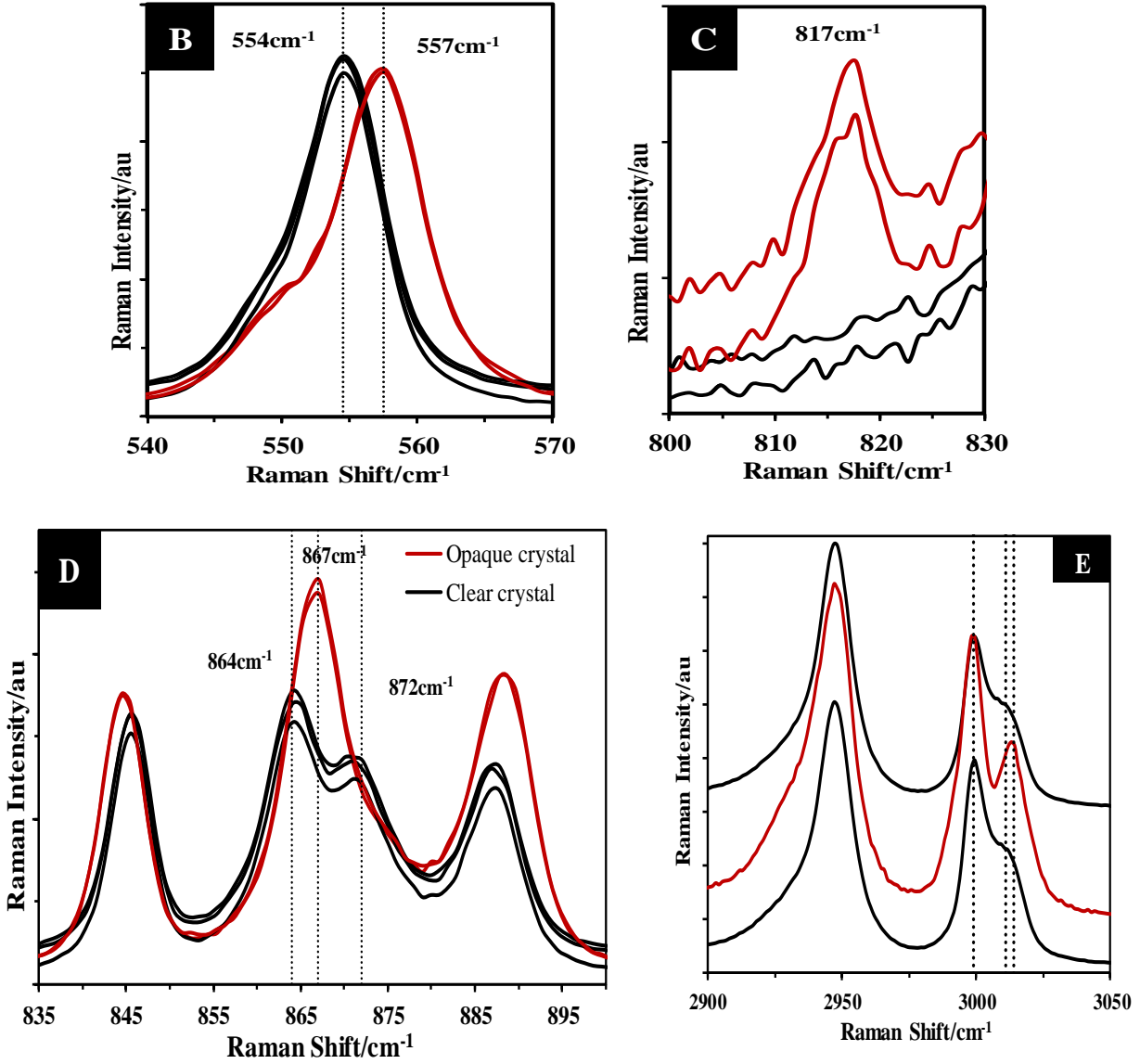


Figure 5-3. Raman spectra of clear square and opaque amorphous TATP crystals at (a) rings modes, (b) 200-450 cm⁻¹ range, (c) CCOO shearing. (d) ν_{O-O} vibrations and (e) at ν_{C-H} stretching spectral range. Laser line 785nm

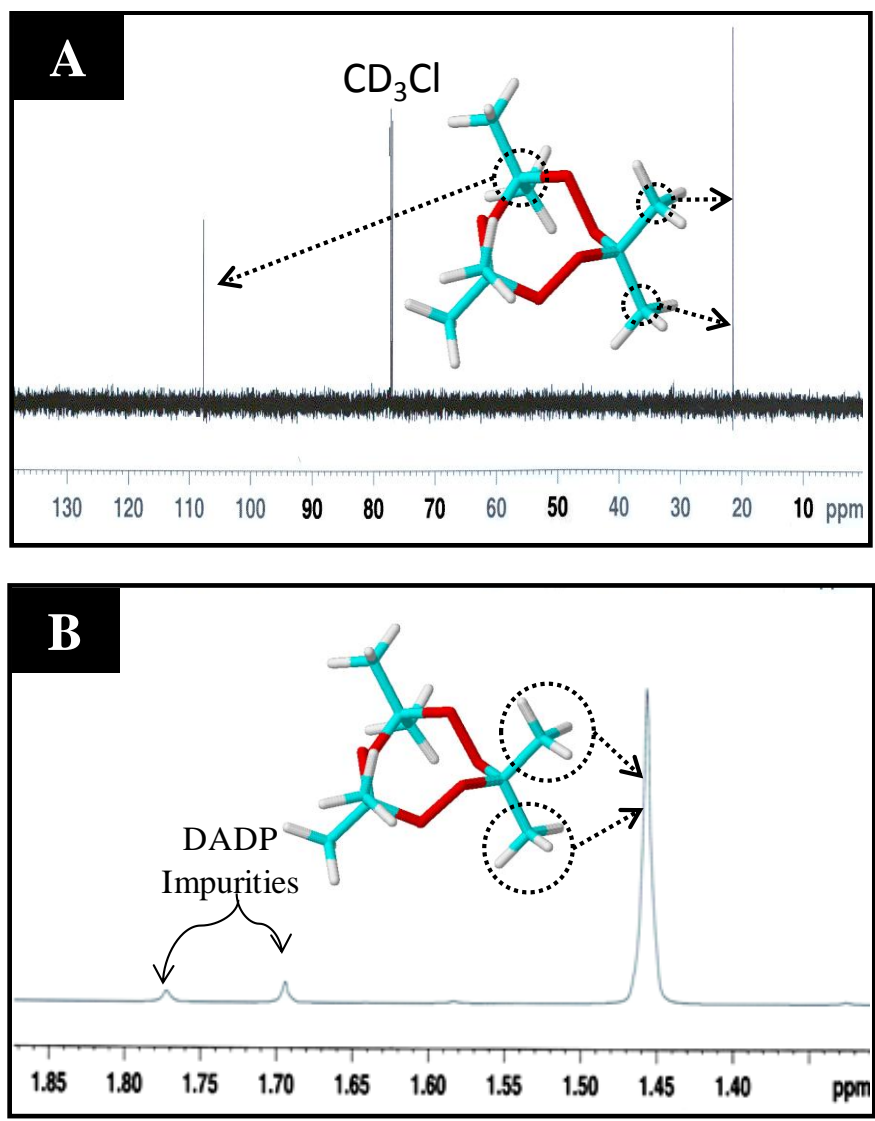


Figure 5-4. (a) ¹H-NMR and (b) ¹³C-NMR spectra of TATP solution of both conformers in CD₃Cl.

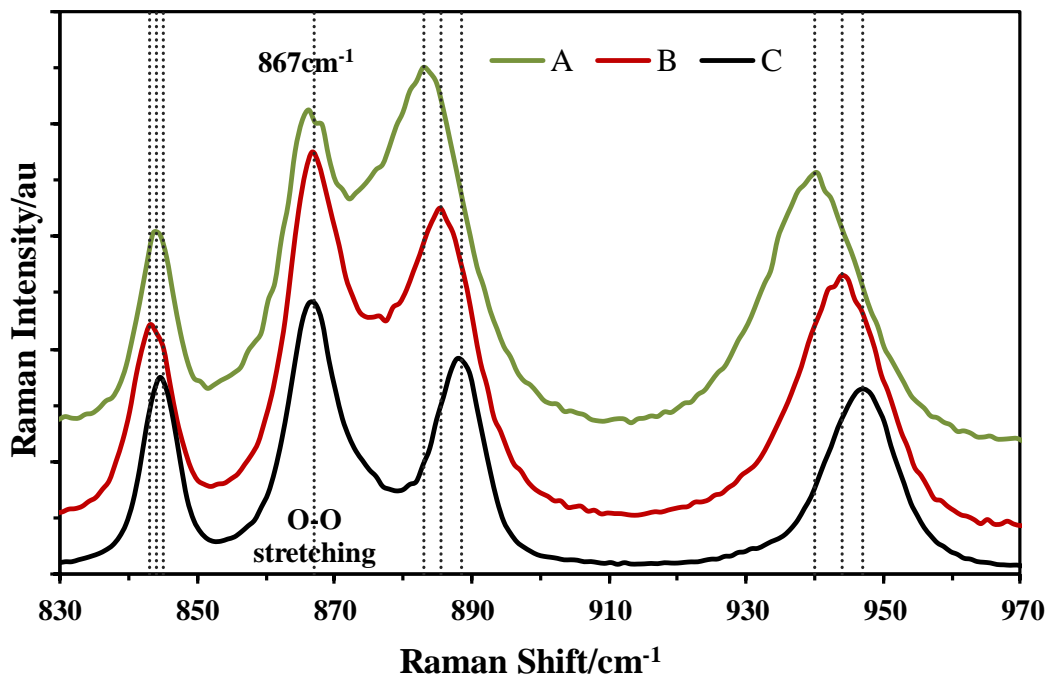


Figure 5-5. Raman spectra of: **A**-TATP-3, 6, 9- $^{13}\text{C}_3$, **B**-TATP-3', 3', 6', 6', 9', 9'- $^{13}\text{C}_6$ and **C**-TATP compounds. The only unshifted band at 867 cm^{-1} corresponds to the peroxide stretch, because the oxygen atoms were not isotopically labeled.

The theoretical analysis confirmed that the methyl environments are chemically equivalent in the D_3 -TATP conformer and slightly different in the C_2 -TATP conformer (Figure 5-2). In addition to this theoretical analysis, we could estimate an approximated experimental value of the transition energy ($\Delta E_{\text{transition}}$), which was -1.1 Kcal/mol . The $\Delta E_{\text{transition}}$ was calculated considering the Raman shifts of the implied bands and using the vibrational expression below (Eq. 5-1) [56]. This value agrees with the semiempirical method PM3 (see Table 5-1). The $\Delta E_{\text{transition}}$ does not represent the minimal energy required to carry out any reaction process. By contrast, it is the activation energy who predicts the energy requirements necessary for a chemical change, and this parameter could not be determined with the present experiment. Several researchers have reported interconversion between hetero and homo molecular rings of

nine atoms at lower room temperature, which supports the results reported here [54, 57]. Where, ν_e is the fundamental frequency and χ_e is the first anharmonicity constant.

$$\Delta E_{\text{Transition}} = \left(\frac{\Delta \nu_{\text{exp}}}{4\chi_e} \right) \quad 5 - 1$$

Table 5- 1. Energy values of the C₂-TATP to D₃-TATP Transition at Different Theoretical methods.

Theoretical Method	$\Delta E_{\text{Transition}}/\text{Kcal.mol}^{-1}$
AM1	-2.6
PM3	-1.5
HF/STO-3G*	-4.6
HF/6-311G++(d,p)	-3.5
B3LYP/STO-3G*	-2.8
B3LYP/6-311G++(d,p)	-2.1
B3PW91/STO-3G*	-3.0
B3PW91/6-311G++(d,p)	-2.2

5.2.2 X-Ray diffraction (XRD) Results

Each crystal lattice has a group of crystallographic planes or a diffraction pattern that characterizes it, in which each peak of the X-ray diffractogram is related to a family of Bragg planes. For example: a face center cubic lattice (FCC) has six families of planes, whose Miller index are: 111, 002, 220, 311, 222 and 400. The opaque and clear crystal presented different diffraction pattern or group of families of crystallographic planes. Hence the crystalline lattices are largely different (see Figure 5-6). XRD measurements are necessary but not sufficient to differentiate between D₃-TATP and C₂-TATP conformers, given that either crystal samples can have either solvent inclusions or not to be pure enough to give a real or representative XRD of the respective lattice. In order to corroborate the veracity of these results, other analysis such as:

FT-IR, Raman, constant physics, among others must be completed. Complementarily, the Raman spectra did not show bands related to solvents used in the recrystallization steps, and DSC thermogram did not show evidence of any contaminants. The melting point ranges reflected high purity in the crystals obtained. Analyses that involve dissolving of the solid sample do not serve to differentiate these conformers, because the sample identity can change by leading to erroneous assessment. With regards, to the possibility of interconversion and isolation of these structures at the temperatures reported above, Haroune and Widmer et al. reported interconversion between D_3 and C_2 -TATP at room temperature [54, 16]. Denekamp et al. showed theoretical and experimental evidence that both conformer are kinetically stable and separable at room temperature [14]; hence, it is possible to obtain neat crystals of both conformers through the method reported in this manuscript.

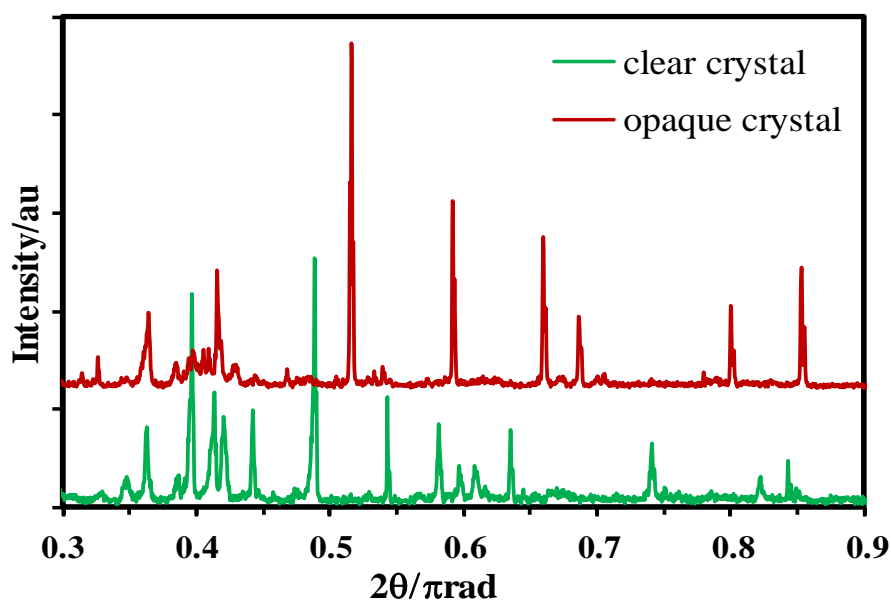


Figure 5-6. XRD diffractograms of both D_3 and C_2 -TATP conformers. In powder mode. X-ray source: $\text{CuK}\alpha$ at 44 kV/40 mA. Data was collected using a Goniometer Ultima θ - θ gonio.

5.2.3 Differential Scanning Calorimeter (DSC) Results

As was stated before, physical constants can corroborate that these crystal samples correspond to different conformations and different interaction pattern, because either it is a directed measure of the interaction forces that keep the molecules bonded in a crystal lattice, or an indirect measurement of molecular symmetry. For this, the melting point is a good parameter. The melting ranges were consistently 85 °C for opaque crystals and 90 °C for clear ones (Figure 5-7). It is proposed that the D₃-TATP conformer correspond to the crystal of higher melting point, because D₃-TATP is a structure of higher symmetry than C₂-TATP and its molecules can be organized in a more packed crystal arrangement. Hence the interaction forces and melting point value are higher. Also, the melting ranges reflect high purity in these crystals samples and none contaminant present, such as: DADP, solvents and others AP-cycles analogs. All reported melting points of TATP vary widely from 88 °C to 91 °C [16, 14, 46, 53, and 58] which indicates that they are melting point of mixtures of both conformers. On the other hand, a DSC analysis of conformer mixtures showed the two resolved peaks for each conformer (see Figure 5-7).

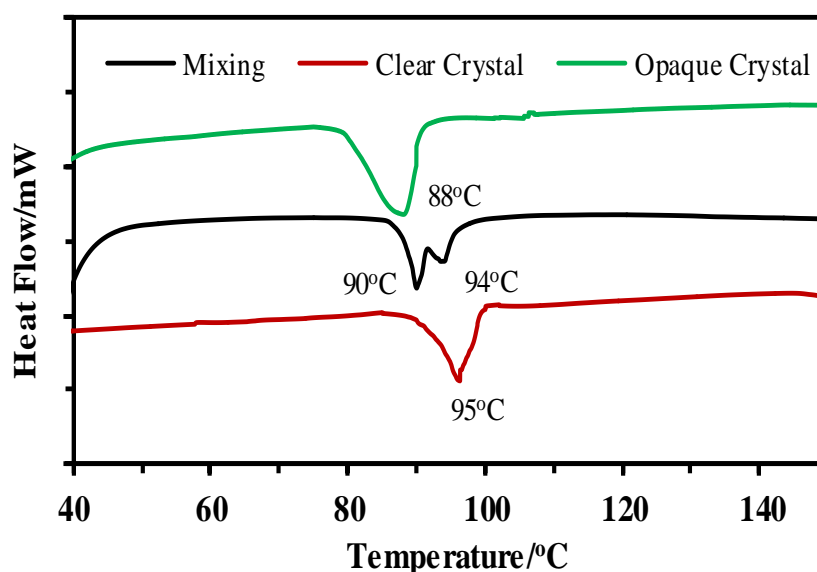


Figure 5-7. DSC thermogram of: crystal mix, clear and opaque crystals of TATP at 5 °C/min.

5.3 CONCLUSIONS

The experimental measurements show sufficient evidence that both crystals samples are different conformers of TATP. The melting point ranges confirmed that the clear crystal sample is a molecular structure of higher symmetry than the opaque crystal. Also both melting values reflected high purity of the crystals analyzed. The opaque and clear crystal presented different diffraction patterns, confirming that the crystalline lattices are largely different. It was also possible to estimate the energy change value for the interconversion process using the Raman shift of the implied bands.

Chapter VI

6. ANALYSIS OF TETRAMETHYLENE DIPEROXIDE DICARBAMIDE (TMDD) BY DIRECT ANALYSIS IN REAL TIME-MASS SPECTROMETRY

Tetramethylene diperoxide dicarbamide (TMDD) was characterized by mass spectrometry for the first time using Direct Analysis in Real Time-Time of Flight-MS (DART-TOF-MS) and ammonia vapor as DART gas dopant. The DART mass spectra of TMDD showed a strong ammonium adduct peak $[M-NH_4]^+$ at 254 m/z and a more intense protonated molecular mass $[M-H]^+$ at 237.084 m/z corroborating the identity of the sample analyzed. The DART-MS spectra of the TMDD isotopomer successfully corroborated the respective molecular tails. The principal fragmentation residues also showed coherence according to the number of isotopically labeled atoms on the TMDD structure. In contrast with other organic peroxides analyzed by this technique, TMDD exhibited substantial fragmentation. The theoretical modeling showed that the DART-MS fragmentation mechanism of the TMDD ion adducts is strongly dependent of the TMDD ring flexibility and the hydrogen bonding between the amine, methylene and atmospheric proton atoms and the different electrophilic centers.

6.1 EXPERIMENTAL SETUP

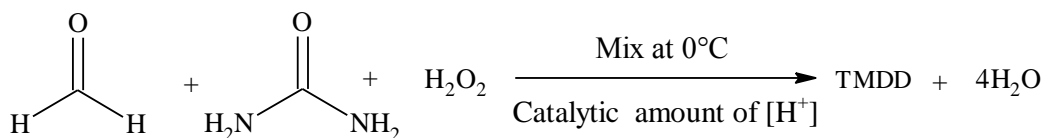
6.1.1 Reagents

The chemical reagents used in this research were: urea, urea- $^{15}N_2$, urea- ^{13}C at 98%, formaldehyde (CH_2O) at 37% and hydrogen peroxide (H_2O_2) at 50%. All of these reagents were

purchased from Aldrich-Sigma Chemical Co. (Milwaukee, WI). Sulfuric acid (H₂SO₄, conc.) were obtained from Fisher Scientific International.

6.1.2 Synthesis

TMDD, TMDD-¹³C₂ and TMDD-¹⁵N₄ isotopomer were synthesized using an improved synthesis of the initially proposed by Von Girssewald and Siegens (Figure 1) [59]. In detail, the precursors were mixed according to the connectivity order in the overall structure of the compound, specifically, carbonyl and amine groups came from urea structure, the methylene and peroxy tails from formaldehyde and hydrogen peroxide reagents respectively. In that vein, stoichiometric amounts of urea were added to formaldehyde solution, then catalytic amounts of sulfuric acid were added, the resultant reaction mixture was stirred for one hour, and finally the hydrogen peroxide was added dropwise. The reaction was finished by storing in a refrigerator for 3 to 5 days at 0 °C. The white precipitate was filtered and washed with water and acetone to remove the organic impurities. The solid samples had a powder like consistency. Similarly, the TMDD-¹⁵N₄ and TMDD-¹³C₂ isotopomers were synthesized from urea-¹⁵N₂ and urea-¹³C respectively.



Scheme 6-1. Synthetic pathway of TMDD compound. The TMDD-¹⁵N₄ and TMDD-¹³C₂ isotopomer were synthesized from urea-¹⁵N₂ and urea-¹³C₂ respectively.

6.1.3 Equipment and DART-MS Optimization

The direct probe MS analysis was performed on a JEOL GC-Mate II (JEOL-USA, Peabody, MA). A JEOL Accu-TOF-DART™ was used to characterize the sample at ambient conditions. The DART chemical ionization region used a helium flow rate set at 2 L/min, a

needle voltage of 3500 VDC, an electrode 1 setting of 150 VDC and an electrode 2 setting of 250 VDC.

As a starting point, unlabeled TMDD was used to optimize the DART temperature and ionization conditions. The DART gas temperature was tested at 250, 350, 450 and 500 °C. The 450 °C and 500 °C spectra showed the best results for producing an $[M-H]^+$ signal. Next, the sample was tested with the DART gas dopant NH_4OH at both 450 °C and 500 °C. For both temperatures, the overall $[M-H]^+$ signal improved when ammonium was added, with only a slightly better signal for the 500 °C experiment. Additionally, the $[M-NH_4]^+$ was also observed, which offered additional confirmation of the observed analyte. As a result of these experiments, all samples were analyzed at 500 °C using NH_4OH as a DART gas dopant.

6.2 RESULTS AND DISCUSSION

6.2.3 DART-MS Fragmentation Pattern

TMDD is a homemade explosive relatively stable to impact and heat, but it has an extremely low vapor pressure. The latter property is a problem for the analysis of this compound by vaporization methods such as GC-MS. In addition, it has a low solubility in many organic solvents, which limits it to be analyzed by separation techniques as LCMS and HPLCMS. The fact that TMDD is soluble in sulfuric acid is not a useful option for LC-MS analysis since most chromatographic and MS equipment can be severely damaged by contact with strong inorganic acids [59]. Fortunately, open air ionization techniques like DART-MS offer an option for mass spectral analysis given that, it does not require sample high volatility or solubility. Figure 6-1a shows a typical DART-mass spectrum of TMDD exhibiting large number of fragment peaks and the molecular adduct ions: $[TMDD-H]^+$ and $[TMDD-NH_4]^+$ by confirming the identity of the analyzed samples. The large numbers of peaks indicate that this compound is more unstable than

other organic peroxides such as HMTD which showed very little fragmentation by DART-MS analysis [17, 60]. On the other hand, The DART-MS spectra of the isotopomer successfully corroborated the respective molecular adducts; specifically, the $[\text{TMDD-}^{15}\text{N}_4\text{-NH}_4^+]$ and $[\text{TMDD-}^{13}\text{C}_2\text{-NH}_4^+]$ molecular ion adducts shifted four and two m/z-units more than the unlabeled adducts peak respectively; the principal fragmentation residues also showed coherence according to the number of isotopically labeled atoms on the TMDD structure. The principal m/z-shifts are summarized in the Table 6-1.

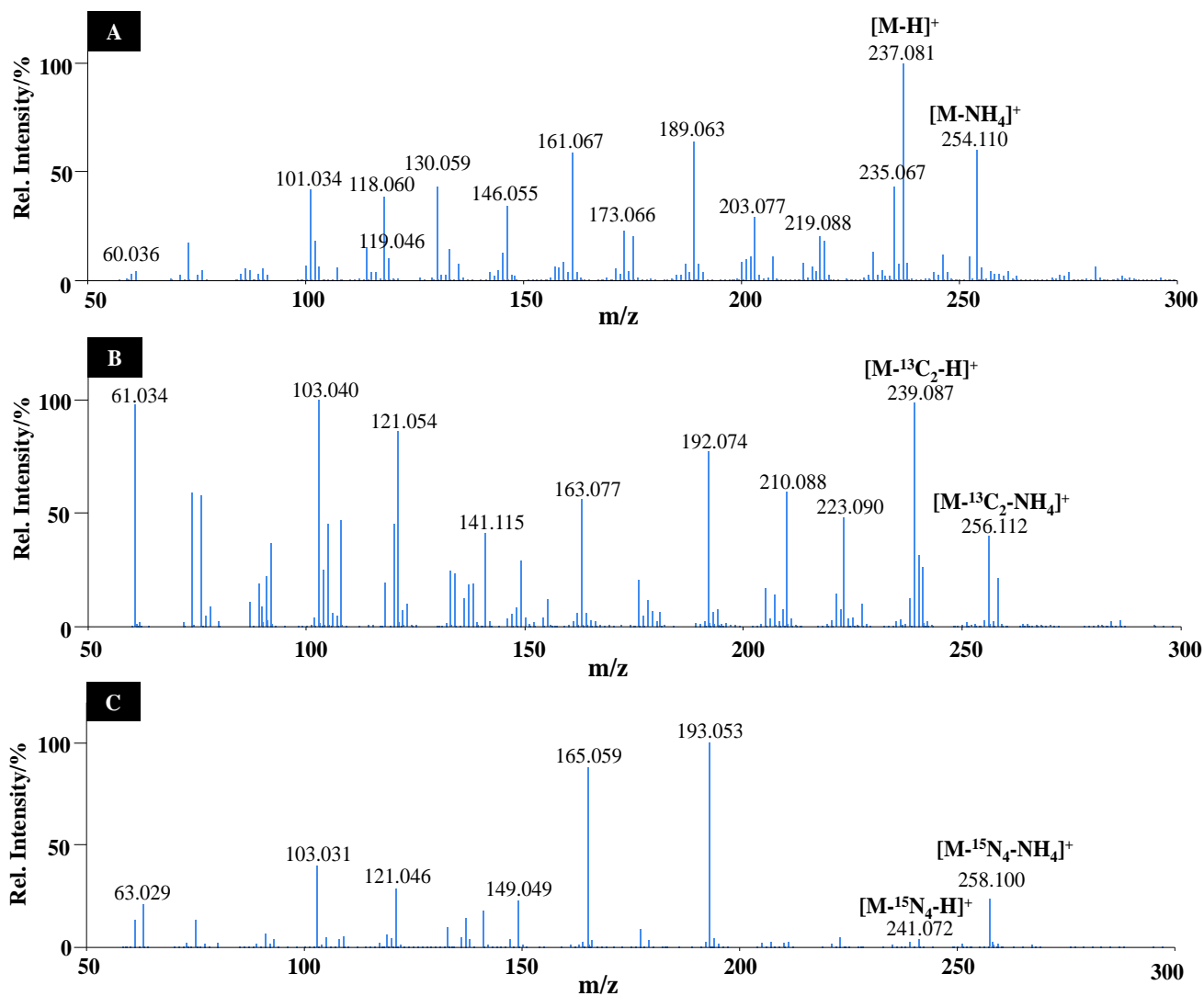


Figure 6-1. Positive-ion DARTTM mass spectrum of: (a) TMDD, (b) TMDD-¹³C₂ and (c) TMDD ¹⁵N₄ isotopomer. Ammonium hydroxide headspace vapor provided a source of NH₄⁺ to form ammonium adducts in a He gas stream used for open air chemical ionization MS. The DART gas temperature was tested at 250, 350, 450 and 500 °C. The 450 and 500 °C showed the best results for producing an [M-NH₄]⁺ signal.

Table 6-1. Fragments list of the [TMDD-¹⁵N₄-NH₄]⁺, [TMDD-¹³C₂-NH₄]⁺ and [TMDD-NH₄]⁺ adducts. --- Values not found.

TMDD		TMDD- ¹³ C ₂		TMDD- ¹⁵ N ₄	
Fragment ion	Shift/(m/z)	Expected shift/m/z	Shift/(m/z)	Expected shift/m/z	Shift/(m/z)
[TMDD-NH ₄] ⁺	254	256	256	258	258
[TMDD-H] ⁺	237	239	239	241	241
[C ₆ H ₁₁ O ₅ N ₄] ⁺	219	221	---	223	---
[C ₅ H ₉ O ₄ N ₄] ⁺	189	191	192	193	193
[C ₄ H ₉ O ₃ N ₄] ⁺	161	163	163	165	165
[C ₄ H ₈ O ₃ N ₃] ⁺	145	147	149	149	---
[C ₃ H ₇ O ₃ N ₂] ⁺	119	121	121	121	121
[C ₃ H ₅ O ₂ N ₂] ⁺	101	103	103	103	103
[C ₁ H ₄ O ₁ N ₂] ⁺	60	61	61	63	63

In order to explain the fragmentation pattern of this homemade explosive, the principal molecular adducts, possible residual tails and possible reaction with ammonium and proton ions were optimized and modeled at semiempirical and Hartree-Fock level of theory. In general, the theoretical results showed that the DART-MS fragmentation pattern of the [TMDD-NH₄]⁺ adduct is strongly dependent of: the interaction of the amine, methylene and atmospheric proton atoms with the different electrophilic centers (N-amine, O-peroxyl and O-carbonyl atoms), the TMDD ring flexibility and multiple ring configurations that this molecule can to adopt. Figure 6-2 shows the optimized structure of lower energy forming internal hydrogen bonding that may cause the ring deformation and possible fragmentation of the ring when minimal amount energy is provided. These atomic movements and hydrogen interactions may to vary depending on the ring conformation by giving rise to other possible fragments. Figure 6-3 shows the ring conformation flexibility and the possible hydrogen bonding with different electrophilic atoms, these models reveal how flexible the TMDD ring is. Some fragmentation steps were modeled

considering the possible transitions state and IRC calculation at Hartree-Fock level of theory in order to propose a well-decomposition mechanism in agreement to the experimental results. Some energy diagrams showing the formation the most important peaks are included (Figures 6-4a to 6-4c). The $[\text{TMDD-NH}_4]^+$ adduct (254 m/z) is formed by the interaction between the ammonium hydrogen atoms with the different electrophilic atoms forming multiple hydrogen bonding (Figures 6-2, 6-3 and 6-4a). Among all possible interactions, the stronger one is formed when the ammonium hydrogen atoms interact with the carbonyl oxygen atom leading to the formation of the molecular fragment at 237 m/z (See energy diagram in the Figure 6-4a). On the other hand, the DART ionization commonly produces protonated molecular ion $[\text{M-H}]^+$ as result of the protons transfer from the atmospheric molecules [61-65].

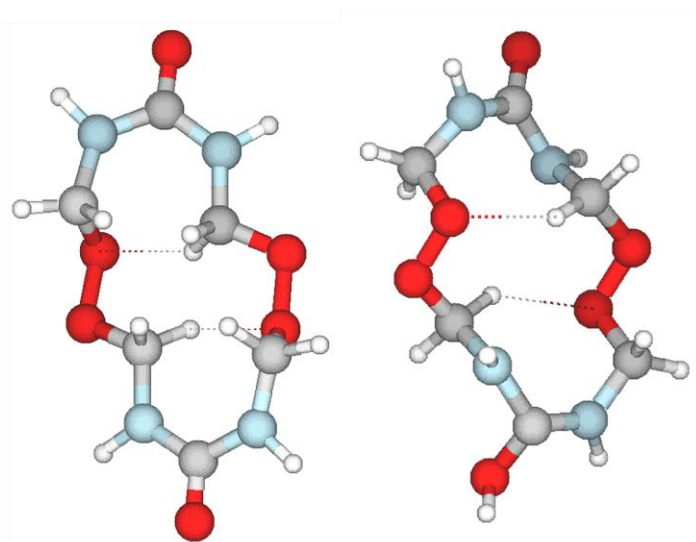


Figure 6-2. Higher symmetry structures of TMDD exhibiting the possible intra-hydrogen bonding that may cause the ring breaking to form the residues at 118 and 119 m/z.

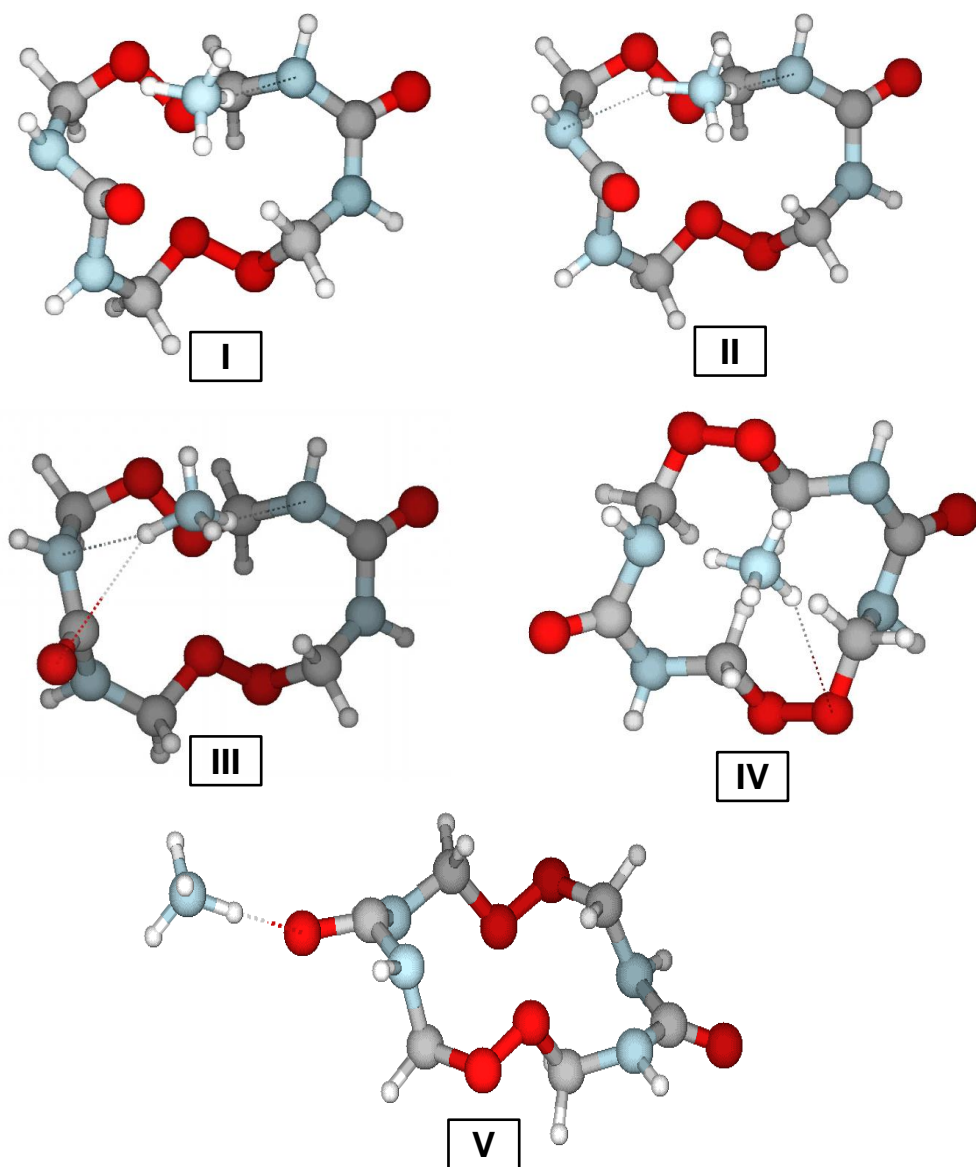


Figure 6-3. TMDD structure forming multiple hydrogen bonding with ammonium ion. These atomic movements also show the high flexibility of the ring. Several form of the $[\text{TMDD-NH}_4]^+$ adduct. **I**-Hydrogen bonding with nitrogen atom, **II**-two simultaneous hydrogen bonding, **III**-Three simultaneous hydrogen bonding, **IV**- Hydrogen bonding with peroxy oxygen atom and **V**-Hydrogen bonding with the oxygen carbonyl atom.

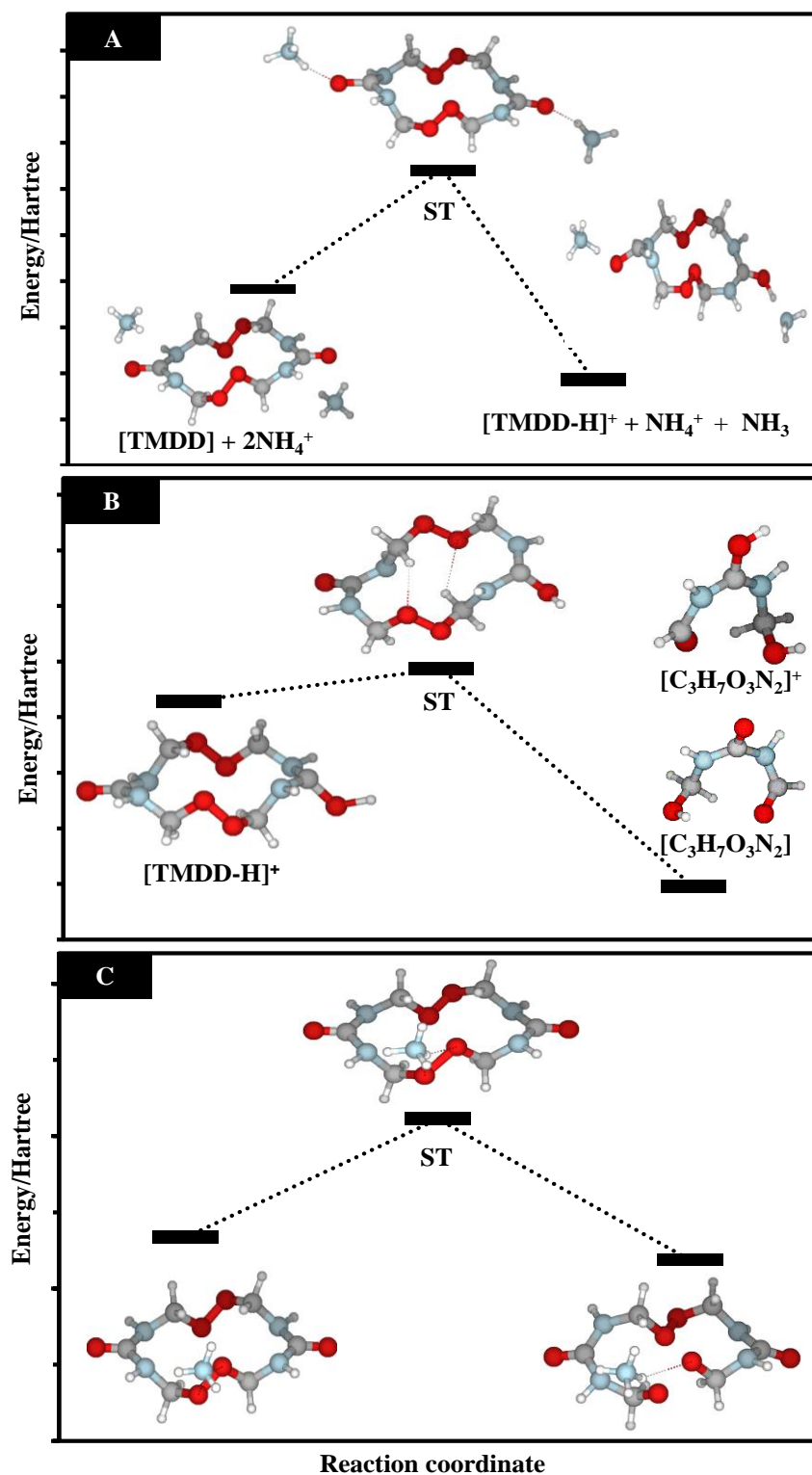
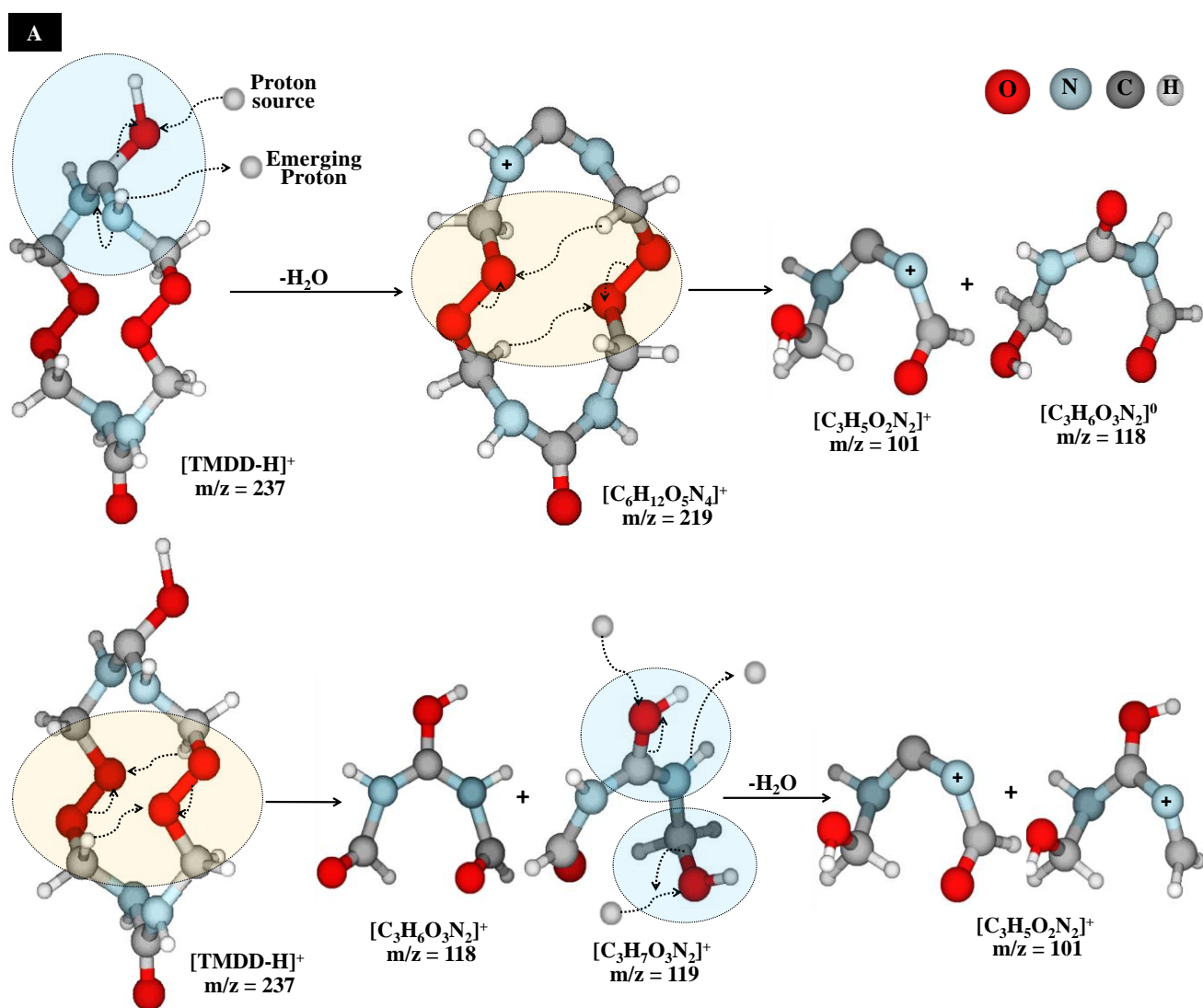
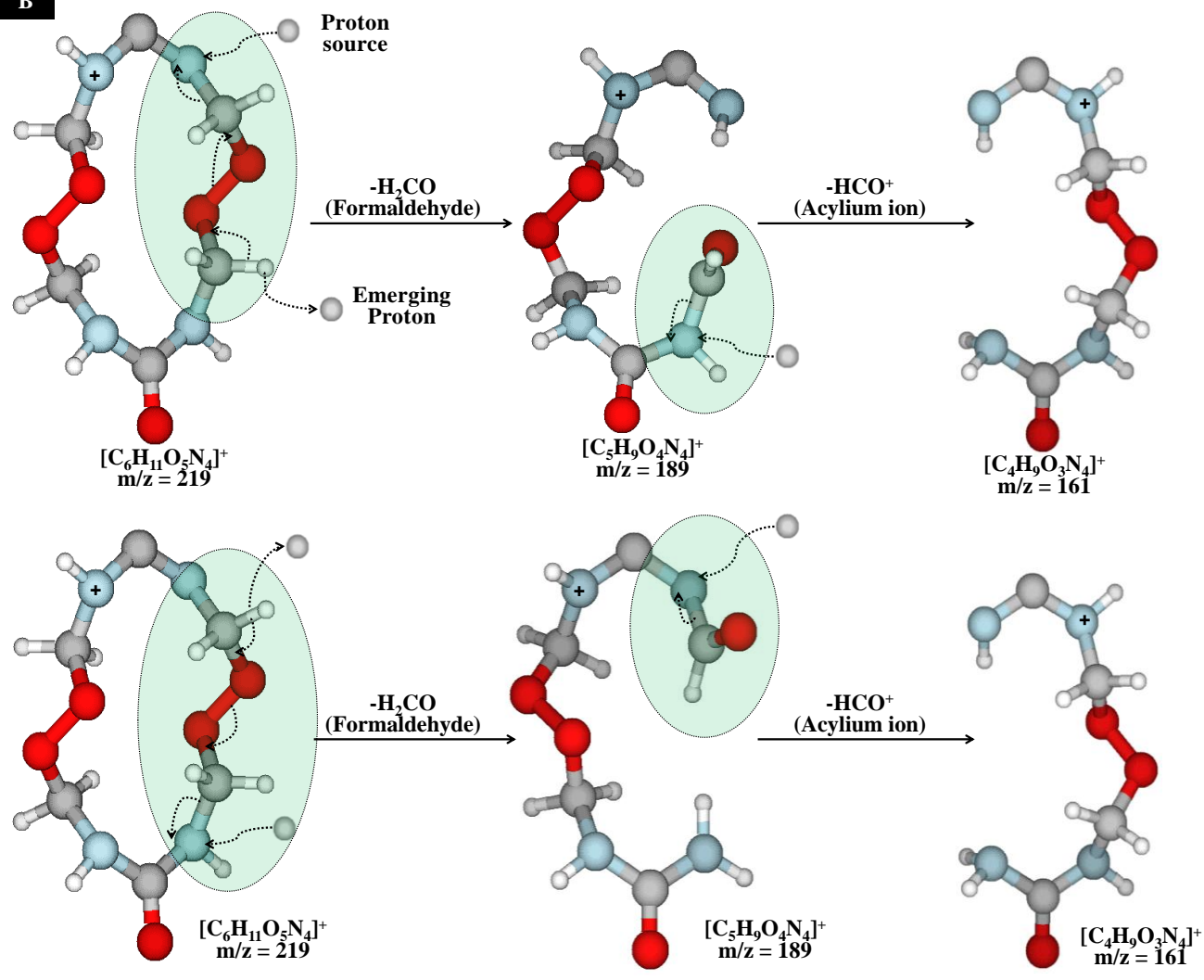


Figure 6-4. Energy diagram and sequence of atomic movements in the: (a) $[\text{TMDD-H}]^+$ adduct formation reaction, (b) $[\text{C}_3\text{H}_7\text{O}_3\text{N}_2]^+$ adduct formation and (c) breaking of O-O bond catalyzed by ammonium ion at Hartree-Fock level of theory and B3LYP/6-311++g (d, p) basis set. First, it were calculated the transitions states, if a TS is found. Then an intrinsic reaction coordinate (IRC) calculation is carried out in order to connect both states: reagents and probable products. The IRC was followed in forward mode only.

The most likely fragmentation mechanism is schematized in Figures 6-5a to 6-5c. In general, the cleavages of the heteroatomic bonds and molecular rearrangements are promoted by hydrogen bonding and the bond energy order of the implied bonds. As is shown in the above figure there is a group of fragments formed by breaking O-O bond, another by breaking C-O and still another by C-N bond breaking. Specifically, the fragment ion at 219 m/z is formed by water loss of the fragment 237 m/z. In this step, the proposed atomic movements are as follow: first, a proton source (ammonium hydrogen or atmospheric molecules) interacts with the previously protonated oxygen atom of the carbonyl tail ($\sim\text{C}=\text{O}\cdots\text{H}^+$) simultaneously releasing a water molecule. This process is promoted by the lone electronic pair of the adjacent nitrogen atom, while compensating the electron-deficient of the carbonyl carbon atom. The fragment ion at 189 m/z is formed by acylium ion loss ($\text{H}-\text{C}\equiv\text{O}^+$) from the fragment at 219 m/z, which is a characteristic residual loss of the carbonyl structures fragmentation [66]. Figure 6-5a shows the sequence of atomic movements for this process. The fragment ion at 161 m/z is formed from the peak 189 m/z by loss of an acylium ion moiety, following the same decomposition pattern of the peak 219 m/z. In this process, an internal or external proton atom can to interact with a nitrogen atom by causing a C-N bond rupture and then a molecular rearrangement according to electron densities requirements. The formation of the fragments ions at 118 and 119 m/z occurs through an O-O breaking promoted by the either external or internal proton atoms forming bifunctional structures containing hydroxyl and carbonyl groups or two carbonyl tails (Figures 6-4b and 6-5b). Figures 6-4c and 6-5b show the O-O rupture process catalyzed by ammonium protons and intramolecular hydrogen atoms. The fragment ion at 101 m/z can be explained from two pathways: first, by water loss of the fragment at 119 m/z, and second from O-O breaking of the fragment 219 m/z following a decomposition pattern similar to the peak 237 m/z above explained. The fragment ion at 60 m/z corresponds to a residue similar to the protonated urea,

which can be formed from symmetrical rupture of the C-N bonds catalyzed by external protons or from the residue at 119 m/z as schematized in Figure 6-5c. The fragment ions at 130, 173 and 203 m/z are formed by loss of an oxygen atom from the peaks at 146, 189 and 219 m/z respectively, which can be explained by the water loss after two successive protonations on the same oxygen atom of the precursor ion.



B

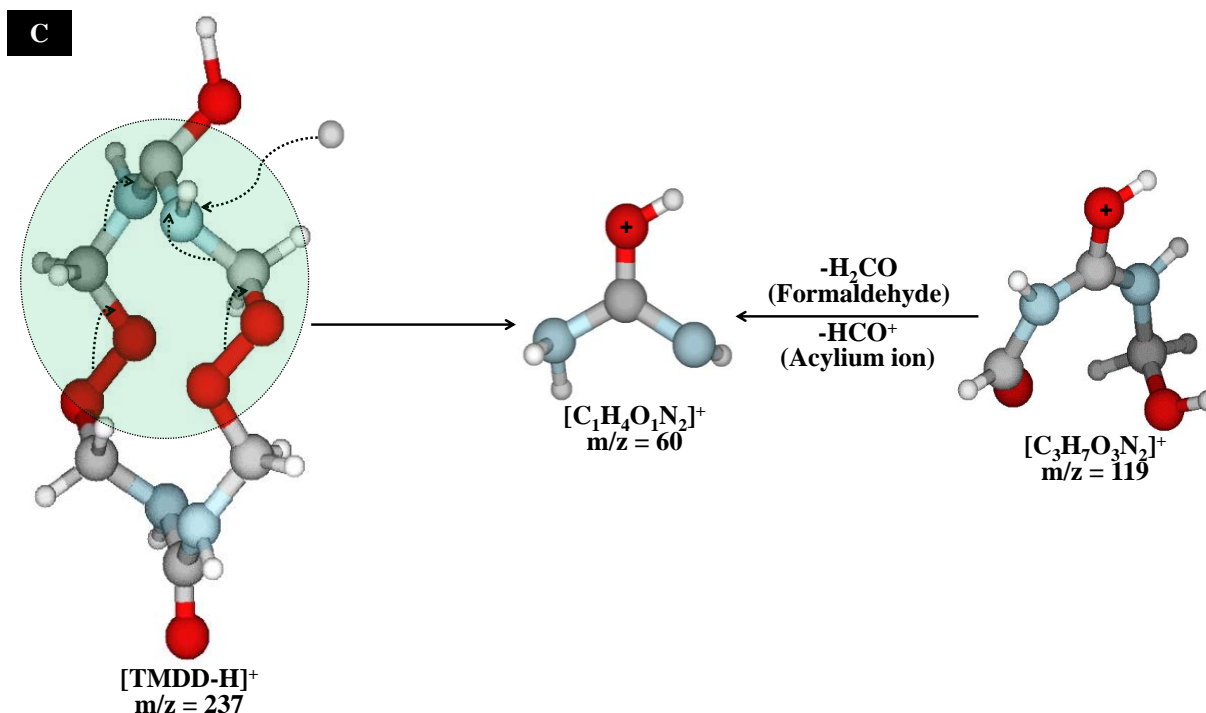


Figure 6-5. (a) Overall fragmentation pattern of [TMDD-H]⁺ adduct considering breaking of C-N and O-O bonds. The electronic pair of the C-H and O-O bonds breaking is used to form the new C=N and N-H bonds. (b) Fragmentation pattern of [TMDD-H]⁺ adduct considering breaking of C-O and O-O bonds. The electronic deficiency of carbonyl and methylene carbon atom is balanced by the electronic pair of the nitrogen atoms. The proton atoms are provided by ammonium ion molecule or atmospheric molecules. In general, the cleavages of the heteroatomic bonds are promoted by hydrogen bonding. The electronic pair of the C-H and O-O bonds breaking is used to form the new carbonyl (C=O) and C-O bonds. The blue, green and yellow shaded areas correspond to the water loss, C-N and O-O break respectively.

The DART-MS spectra of TMDD isotomer corroborated the vast majority of the fragments proposed. Some peaks showed one m/z-unit above or below the expected value, specifically, the [C₅H₉O₄N₄-¹³C₂]⁺ residue of the TMDD-¹³C₂ DART spectrum showed a shift of 192 m/z rather than 191 m/z with respect to the number of isotopically labeled carbon. This may be due to that the implied structures are constitutionally different by a hydrogen atom or the presence of natural isotopes. In general, the principal fragments ions of the DART mass spectrum could be assigned using theoretical modeling and the DART-MS spectra of the TMDD-¹⁵N₄ and TMDD-¹³C₂ isotomers. The statements proposed here for the fragmentation

mechanism of the TMDD compound is one of the many others possible and it is strongly dependent of the ring conformations.

6.3 CONCLUSIONS

Each peak of the DART-mass spectrum was successful related to a structural residue of the [TMDD-H]⁺ adduct. The global fragmentation was explained taking into account hydrogen movements and heterolytic breaking of the C-N, C-O and O-O bonds. The DART-MS spectra of TMDD isotopomer helped to corroborate the vast majority of the fragments proposed here. Some peaks showed one m/z-unit above or below the expected value due to that the implied structures may be constitutionally different by a hydrogen atom or the presence of natural isotopes.

Chapter VII

7. ACOMPLISHMENTS AND SCIENTIFIC CONTRIBUTIONS

Research efforts should be focused in acquiring the necessary knowledge to advance the state of science and to solve the main problems affecting the proper functioning of society. Another important aspect of research is to provide scientific support to misconceptions and scientific ambiguities previously reported or established. This research was aimed at contributing, directly or indirectly, to stop the use and abuse of homemade explosive substances as mass destruction weapons, among others positive aspects listed below.

Specifically, the elucidation of the formation mechanism of TATP helps to find substances that can inhibit or prevent the formation of these compounds. Also, it is possible to improve the reaction yield so that fewer amounts of reagents are required in the formation of the desired products so they may be used in characterization and detection experiments to further enhance terrorist prevention programs.

The success obtained in the uncatalyzed synthesis of DADP is a result of the elucidation of the formation mechanism of cyclic acetone-peroxides products. The high yield-high purity synthesis discovered offers promising result to advance the field of analytical standards for GC, HPLC and MS calibrations. Characterization studies will also benefit from the high purity crystals obtained in the synthetic scheme.

A new thermal approach fitted in a wide range of temperature allows report highly reliable enthalpies values. The main contribution in this area of research is that it helps establishing better standards for related research. The thermal trends showed consistent data with high R^2 values. Even, linear trends could be fitted according to the reported equation leading to higher R^2 values than linear fits.

Evidence of two different crystal structures of TATP formed through two slightly different conformers was important in explaining the variation in the reported melting points, which is an additional criterion for its identification. These results solve a long standing controversy in the area of characterization of the important homemade explosive.

The isotopically corroborated atmospheric pressure ionization MS pattern of TMDD provides firmer grounds in confirming the relatively low stability of the cyclic amino-peroxide homemade explosive. This is the first report in this important area of characterization of this type of compounds. Also, it provides important information for developing detection schemes for the HME.

In general, the improvements in HME synthesis can serve as basis for further research such as: synthesis of isotopomers for assignment of the vibrational and MS spectra with experimental support; increasing the purity and efficiency of formation reactions; reporting reliable physical data; among others. As future work, we will continue working on the vibrational assignment of HME-compounds using their respective isotopomers and DFT theory.

REFERENCES

- [1] Pena-Quevedo, A. J.; Pacheco-Londoño, L. C.; Figueroa, J.; Rivera-Montalvo, L. A.; Roman-Velázquez, F.R.; Hernández-Rivera, S. P. *Proc. SPIE Int. Soc. Opt. Eng.* **2005**, 5778, 347.
- [2] Wolffenstein, R. *Chem. Ber.* **1985**, 28, 2265-2269.
- [3] White, G. M. *J. Forensic Sci.* **1992**, 37, (2), 652-656.
- [4] Yinon, J.; Zitrin, S. *Modern methods and applications in analysis of explosives*. Wiley: Chichester: New York, 1993, pp; 305.
- [5] Dubnikova, F.; Kosloff, R.; Almog, J.; Zeiri, Y.; Boese, R.; Itzhaky, H.; Alt, A.; Keinan, E. *J. Am. Chem Soc.* **2005**, 127, 1146-1159.
- [6] Bellamy, A. J. *J. Forensic Sci.* 1999, 44, 603.
- [7] Hiyoshi, R. I.; Nakamura, J. *Propellants, Explosives, Pyrotechnics.* **2007**, 32 (2), 127-134.
- [8] Milas, N.; Golubovic, A. *J. Am. Chem. Soc.* **1959**, 81(24), 6461-6472.
- [9] Matyas, R.; Pachman, J.; Ang, H. Study of TATP: Spontaneous Transformation of TATP to DADP Propellants *Explosives Pyrotechnics.* **2008**, 33(2), 89-91.
- [10] Jensen, L. P.; Mortensen, M.; Trane, R.; Harris, P.; Berg, R. W. *Applied Spectroscopy.* **2008**, 63, 92-97.
- [11] Oxley, J.; Smith, J.; Brady, J.; Dubnikova, F.; Kosloff, R.; Zeiri, L.; Zeiri, Y. *Applied Spectroscopy.* **2008**, 62(8), 906-915.
- [12] Armitt, D.; Zimmermann, P.; Ellis, S. *Rapid Commun. Mass Spectrum.* **2008**, 22, 950-958.
- [13] Terent'ev, A. O.; Platonov, M. M.; Sonneveld, E. J.; Peschar, R.; Chernyshev, V. V.; Starikova, Z. A.; Nikishin, G. I. *J. Org. Chem.* **2007**, 72 (19), 7237-7243.
- [14] Denekamp, C.; Gottlieb, L.; Tamiri, T.; Tsoglin, A.; Shilav, R.; Kapon, M. *Org Lett.* **2005**, 7(12), 2461-2464.

- [15] Muller, D.; Levy, A.; Shelef, R.; Abramovich-Bar, S.; Sonenfeld, D.; Tamiri, T. *J. Forensic Sci.* **2004**, *49*, 935-938.
- [16] Widmer, L.; Watson, S. Schlatter, K.; Crowson, A. *Analyst.* **2002**, *127*, 1627-1632.
- [17] Peña-Quevedo, A.J.; Cody, R.; Mina-Camilde, N.; Ramos M.; Hernández-Rivera, S.P. *Proc. SPIE* **2007**, *6538*, 653828-653839.
- [18] Oxley, J.; Zhang, J.; Smith, J. *Propellants, Explosives, Pyrotechnics.* **2000**, *25*, 284-287.
- [19] Becke, A. D. *J. Chem. Phys.* **1993**, *98*, 5648-5649.
- [20] Lee, C.; Yang, W.; Parr, R. G. *Phys. Re.* **1988**, *B37*, 785-789.
- [21] Hehre, W.J.; Radom, L.; Schleyer, P.V.R.; Pople, J.A. *Ab Initio Molecular Orbital Theory* Wiley: New York, **1986**.
- [22] Frisch, M.; Schlegel, H.; Scuseria, G.; Robb, M.; Cheeseman, J.; Montgomery, J.; Vreven, T.; Kudin, K.; Burant, J.; Millam, J.; Iyengar, S.; Tomasi, J.; Barone, V.; Mennucci, B.; Cossi, M.; Scalmani, G.; Rega, N.; Petersson, G.; Nakatsuji, H.; Hada, M.; . Ehara, M.; Toyota, K.; Fukuda, R.; Hasegawa, J.; Ishida, M.; Nakajima, T.; Honda, Y.; Kitao, O.; Nakai, H.; Klene, M.; Li, X.; Knox, J.; Hratchian, H.; Cross, J.; Adamo, C.; Jaramillo, J.; Gomperts, R.; Stratmann, R.; Yazyev, O.; Austin, A.; Cammi, R.; Pomelli, C.; Ochterski, J.; Ayala, P.; Morokuma, K.; Voth, G.; Salvador, P.; Dannenberg, J.; Zakrzewski, V.; Dapprich, S.; Daniels, A.; Strain, M.; Farkas, O.; Malick, D.; Rabuck, A.; Raghavachari, K.; Foresman, J.; Ortiz, J.; Cui, Q.; Baboul, A., Clifford, S.; Cioslowski, J.; Stefanov, B.; Liu, G.; Liashenko, A.; Piskorz, P.; Komaromi, I.; Martin, R.; Fox, D.; Keith, T.; Al-Laham, M.; Peng, C.; Nanayakkara, A.; Challacombe, M.; Gill, P.; Johnson, B.; Chen, W.; Wong, M.; Gonzalez, C. Pople, J. *Gaussian 03W*: Revision B.04 Gaussian, Inc., Pittsburgh, PA, **2003**.

- [23] Sigman, M. E.; Clark, C. D.; Caiano, T.; Mullen, R. *Rapid Commun. Mass Spectrum.* **2008**, 22, 84-90
- [24] Espenson, J. H. *Chemical Kinetics and Reaction Mechanisms*; Speer, J.; Morriss, J. M., Eds.; Series in Advanced Chemistry McGraw-Hill Inc: New York, **1995**; pp 32.
- [25] Oxley, J. C.; Smith, J. L.; Steinkamp, L.; Zhang, G. Factors Influencing Triacetone Triperoxide (TATP) and Diacetone Diperoxide (DADP) Formation: Part 2. Propellants Explos. Pyrotech. 2013, 38, 1-11.
- [26] Oxley, J. C.; Smith, J. L.; Bowden, P. R.; Rettinger, R. C. Factors Influencing Triacetone Triperoxide (TATP) and Diacetone Diperoxide (DADP) Formation: Part I. Propellants Explos. Pyrotech. 2013, 38, 244-254.
- [27] Sauer, M. C. V.; Edwards, J. O. The reactions of Acetone Hydrogen Peroxide. I. Higher Adducts. *J. Phys. Chem.*, 1972, 76 (9), 1283–1288.
- [28] Sauer, M. C. V.; Edwards, J. O. The Reactions of Acetone Hydrogen Peroxide. I. Primary Adducts. *J. Phys. Chem.*, 1971, 75 (19), 3004–3011
- [29] Story, P. R.; Lee, B.; Bishop, C. E. Denson, D. D.; Busch, P. Macrocyclic Synthesis. II. Cyclohexanone Peroxides. *J. Org. Chem.* 1970, 35 (9), 3059–3062.
- [30] Sutthasupa, S.; Shiotsuki, M.; Sanda, F. Recent Advances in Ring-Opening Metathesis Polymerization, and Application to Synthesis of Functional Materials. *Polymer Journal.* 2010, 42, 905–915.
- [31] Paudler, W. W. *Nuclear Magnetic Resonance*; Bush, D. H., Shull, H., Eds.; Allyn and Bacon Chemistry Series University of Alabama: Boston, **1971**; pp 17-32, 220-237.
- [32] Espinosa-Fuentes, E. A.; Pacheco-Londoño, L. C.; Barreto-Cabán, M. A.; Hernández-Rivera, S. P. *Propellants, Explosives, Pyrotechnics.* **2012**, 37, 413-421.

- [33] Pacheco-Londoño, L.C.; Pena-Quevedo, A.J.; Primera-Pedrozo, O.M.; Hernández-Rivera, S.P.; Mina-Camilde, N.; García, R.; Chamberlain, R.T.; Lareau, R.T. *Proc. SPIE*, **2004**, 5403, 279-287.
- [34] D. Swern, M. Schulz, K. Kirschke, *Organic Peroxides, Volume III: Cyclic Peroxides*, John Wiley & Sons, New York, **1972**, p. 67, 114.
- [35] Espinosa-Fuentes, E.A.; Pacheco-Londoño, L.C.; Hidalgo-Santiago, M.; Hernández-Rivera, S.P.; *J. Phys. Chem.C. In Process*.
- [36] Kim, S.; Ng, W. K.; Shen, S.; Dong, Y.; Tan, R.B.H. *Colloids and Surfaces A: Physicochem. Eng. Aspects*. **2009**, 348, 289.
- [37] Peña, A.J.; Mina-Camilde, N.; Rodríguez, N.; Nieves, D.; Cody, R.B.; Hernández-Rivera, S.P. *Proc. SPIE Int. Soc. Opt. Eng.* **2006**, 6201, 62012E.
- [38] Cody, R.B.; Laramée, J.A.; Durst, H.D. *Anal Chem.* **2005**, 77(8), 2297.
- [39] *Hyperchem for Windows, Release 5.0*: Hypercube, Inc., Ontario, Canada, **1996**.
- [40] Evans, H.K. Tulleners, F.A.J.; Sánchez, B.L.; Rasmussen, C.A. *J. Forensic Sci.* **1986**, 31(3), 1190-1199.
- [41] Acree WE, Chickos JJS. *J. Phys. Chem. Ref. Data.* **2002**; 31(2), 537-41.
- [42] Griffiths PR, De Haseth JA. *Fourier Transform Infrared Spectrometry*. New York: John Wiley and Sons; **1986**.
- [43] Chatterjee K, Hazra A, Dollimore D, Alexander KS. *Eur. J. Pharm. Biopharm.* **2002**, 54, 171-180.
- [44] Chatterjee K, Dollimore D, Alexander KS. *Thermochim. Acta.* **2002**, 392, 107-117.
- [45] Gupta PK, Ganesan K, Gutch PK, Manral L, Dubey DK. Vapor Pressure and Enthalpy of Vaporization of Fentanyl. *J. Chem. Eng. Data.* **2008**; 53:841-5.

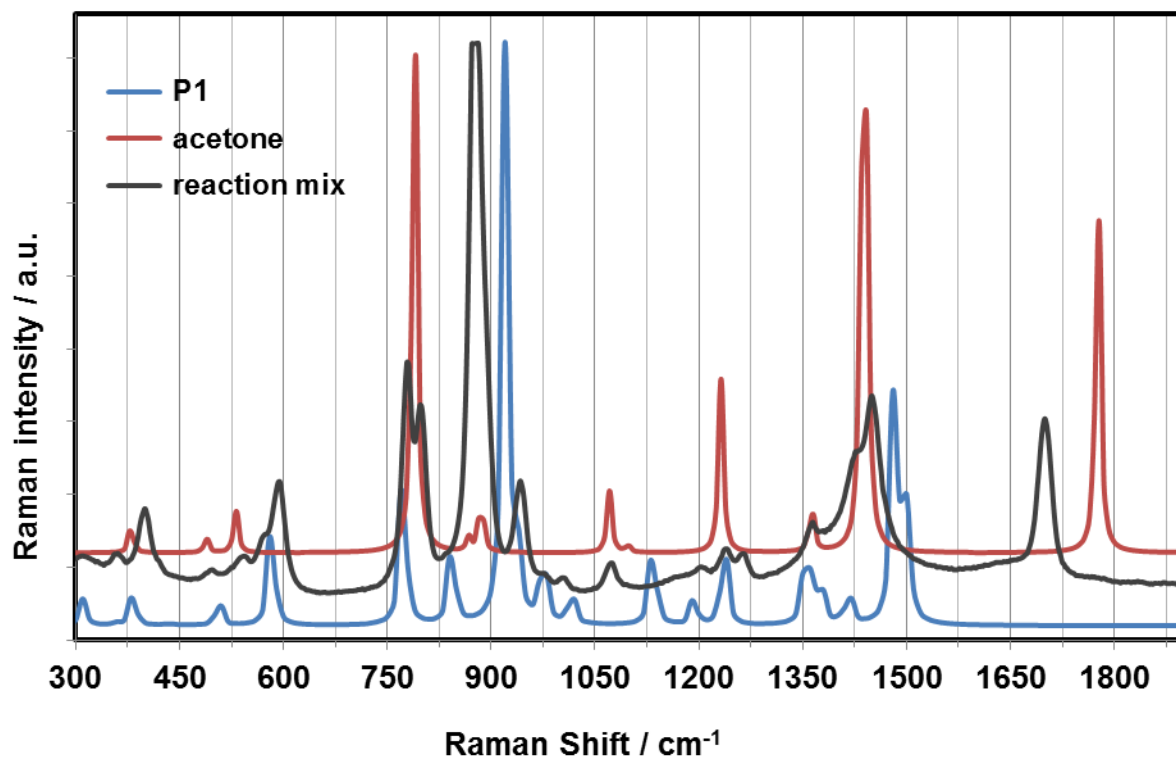
- [46] Félix-Rivera, H.; Ramírez-Cedeño, M.L.; Sánchez-Cuprill, R.A.; Hernández-Rivera, S.P. *Thermochimica Acta*. **2011**; 514, 37–43.
- [47] Acree WE, Chickos JJS. *J. Phys. Chem. Ref. Data*. **2002**, 31(2), 537-541.
- [48] Rojas-Aguilar, A.; Orozco-Guareno, E.; Martinez-Herrera, M. *J. Chem. Thermodynamics*. **2001**, 33, 1405-1418.
- [49] Monte, M.J.S, Santos, L.M.N.B.F. Fulem, M.; Fonseca, J.M.S.; Sousa, C.A.D. *J. Chem. Eng. Data*. **2006**, 51, 757-766.
- [50] Santos, L.M.N.B.F.; Schröder, B.; Fernández, O.O.P.; Ribeiro da Silva, M.A.V. *Thermochimica Acta*. **2004**, 415, 15-20.
- [51] Chatterjee, K.; Dollimore, D.; Alexander, K.S. *J. Therm. Anal. Calorim.* **2001**; 63:629-39.
- [52] Oxley, J.C.; Smith, J.L.; Luo, W.; Brady, J. *Propellants, Explosives, Pyrotechnics*. **2009**, 34, 539–543.
- [53] Reany, O.; Kapon, M.; Botoshansky, M.; Keinan, E. *Crystal Growth Design*. **2009**, 9(8), 3661-3670.
- [54] Haroune, N.; Crowson, A.; Campbell, B. *Science and Justice*. **2011**, 51(2), 50-56.
- [55] McQuarrie, D.A.; Simon J. D. *Physical Chemistry: A Molecular Approach*. University Science Books: Sausalito, CA **1997**; pp 504.
- [56] Oxley, J.; Smith, J.; Brady, J.; Duhnikova, F.; Kosloff, R.; Zeiri, Y. *Applied Spectroscopy*. **2008**, 62, 906-915.
- [57] Wiberg, K. *J. Org. Chem.* **2003**, 68, 9322-9329.
- [58] Ramírez-Cedeño, M.L.; Félix-Rivera, H.; Sánchez-Cuprill, R.A.; Hernández-Rivera, S.P. *J. Thermal Analysis and Calorimetry*. **Article in press**
- [59] Von Girssewald, C.; Siegens. H. *Chem. Ber.* **1914**, 47, 2464-2469.

- [60] Peña-Quevedo, A. J., Mina-Calmide, N., Rodríguez, N., Nieves, D., Cody, R. B. and Hernández-Rivera, S. P. *Proc. SPIE* **2006**, 6201, 62012E-620111E.
- [61] Cody, R. B.; Laramée, J. A.; Durst, H. D. *Anal. Chem.* **2005**, 77, 2297-2302.
- [62] Cody, R. B. *Anal. Chem.* **2009**, 81, 1101-1107.
- [63] Fernandez, F. M.; Cody, R. B.; Green, M. D.; Hampton, C. Y.; McGready, R.; Sengaloundeth, S.; White, N. J.; Newton, P. N. *ChemMedChem* **2006**, 1, 702-705.
- [64] Jones, R. W.; Cody, R. B.; McClelland, J. F. *J Forensic Sci.* **2006**, 51, 915-918.
- [65] Laramée, J. A.; Cody, R. B.; Nilles, J. M.; Durst, H. D. Forensic Applications of DART™ Mass Spectrometry, In *Forensic Analysis on the Cutting Edge: New Methods for Trace Evidence Analysis*, R.D. Blackledge, Eds.; Wiley-Interscience Hoboken: NJ, **2007**.
- [66] Pavia, D.L.; Lampman, G.M.; Kriz, G.S.; Vyvyan, J. A. *Introduction to Spectroscopy*; Lockwood, L.; Kirksey, B.; Woods, E. Eds.; Brooks Cole 4 ed.: Belmont, CA, **1995**; pp 32.

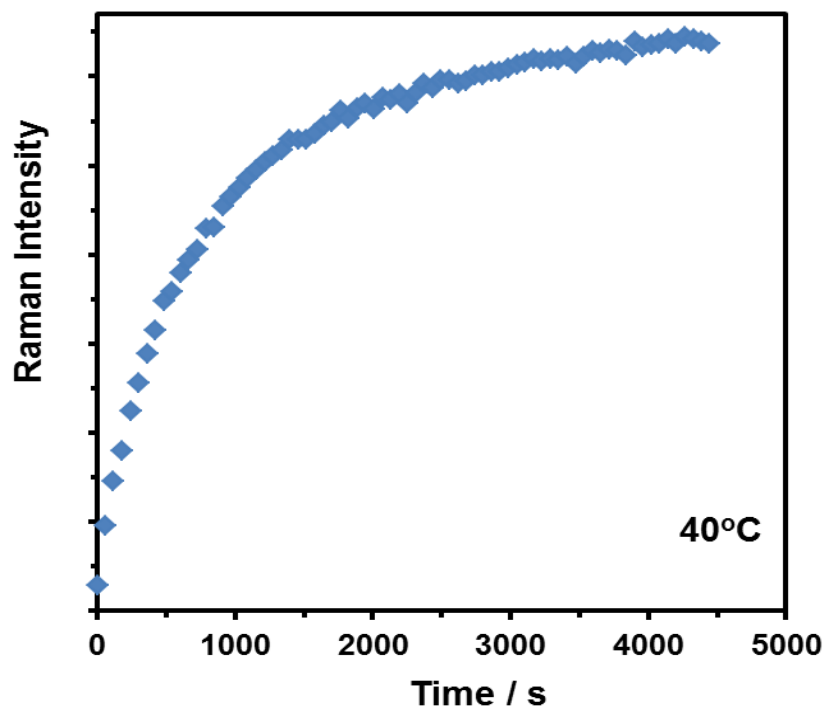
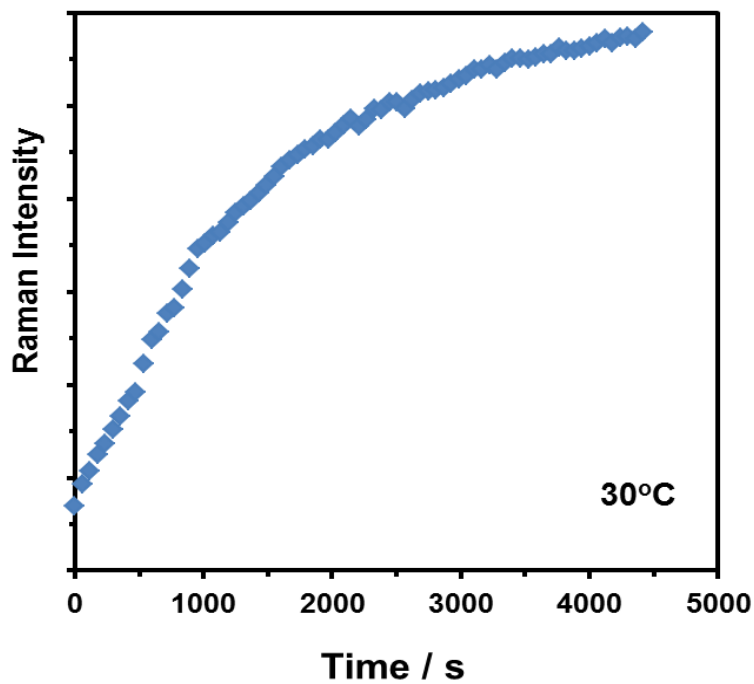
APPENDIX-A

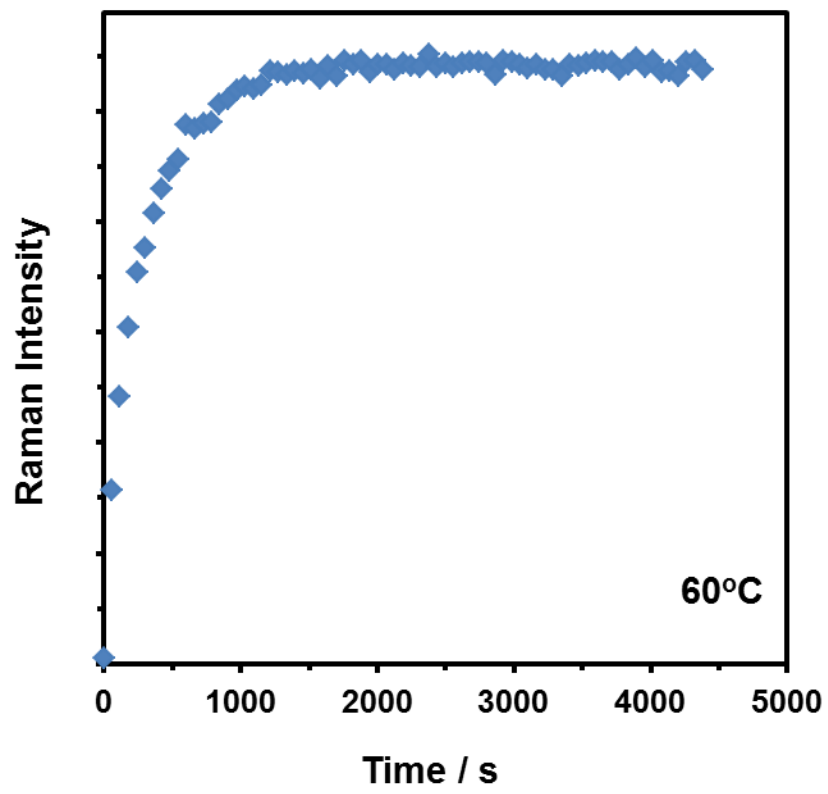
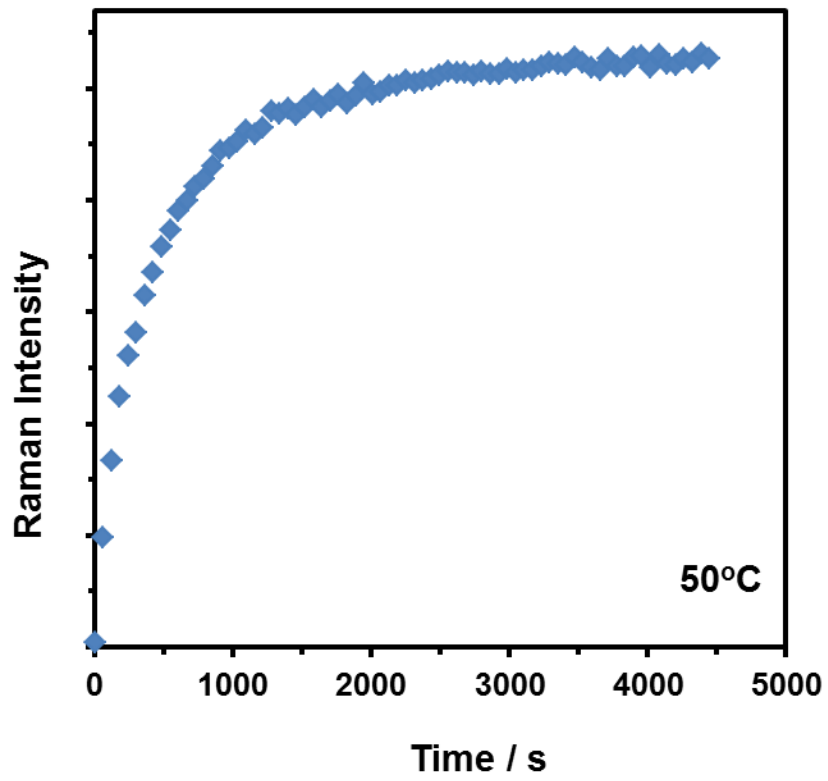
A Mechanism for the Uncatalyzed Cyclic Acetone-Peroxide Formation Reaction: An Experimental and Computational Study

Figure A-1. Theoretically calculated Raman spectra of P1 and acetone and measured Raman spectrum of reaction mix.

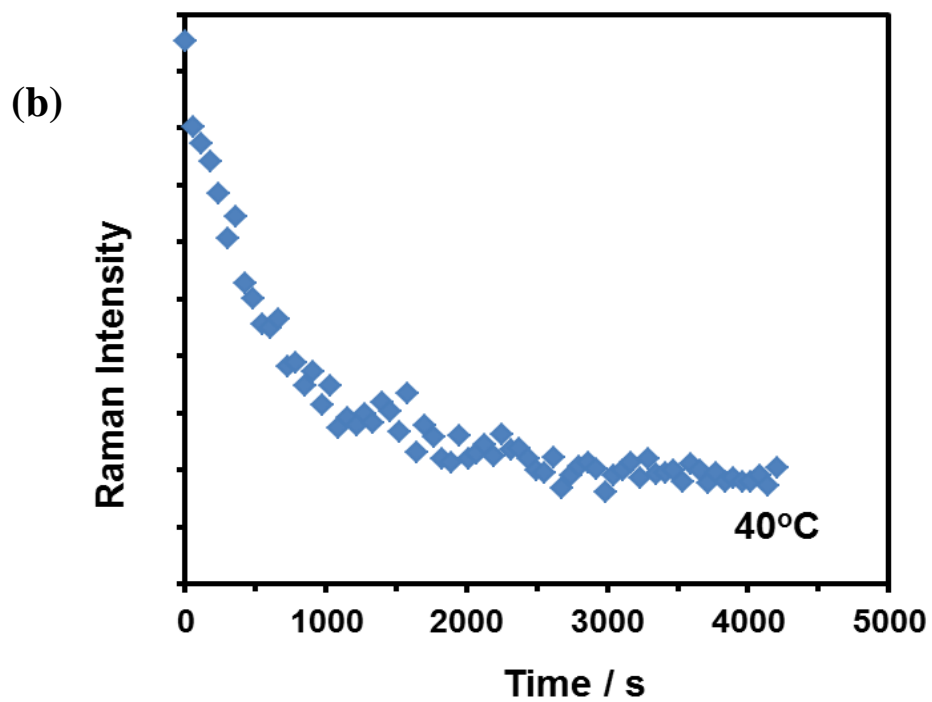
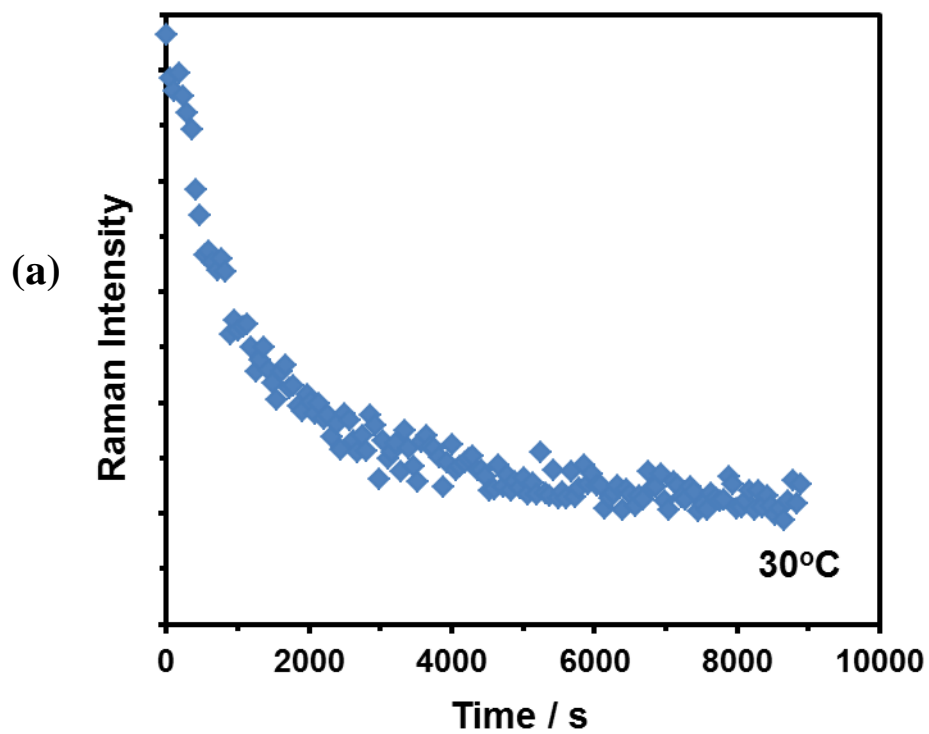


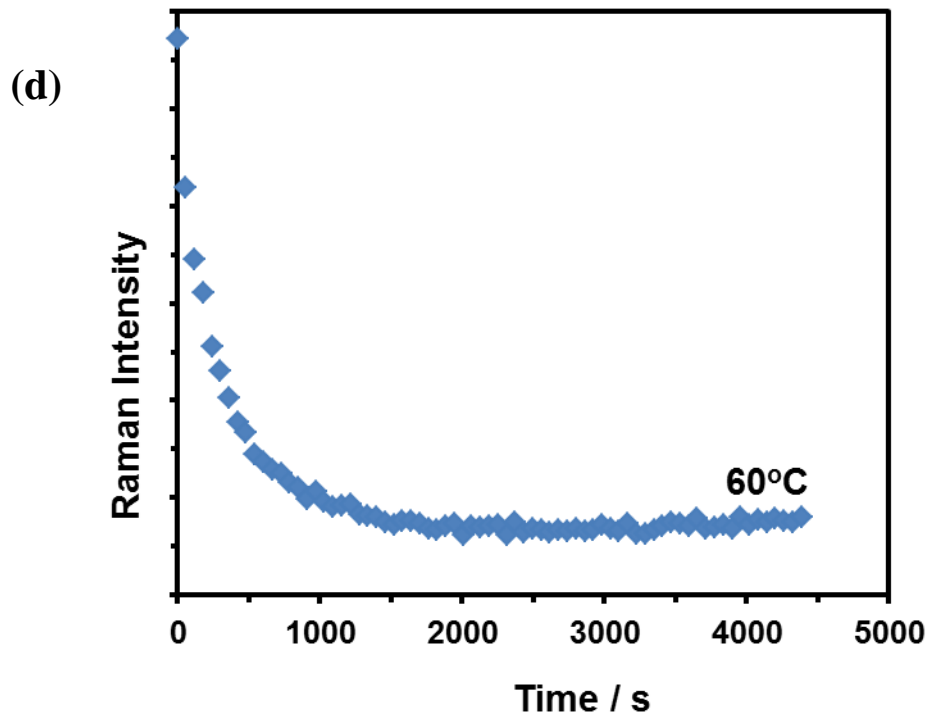
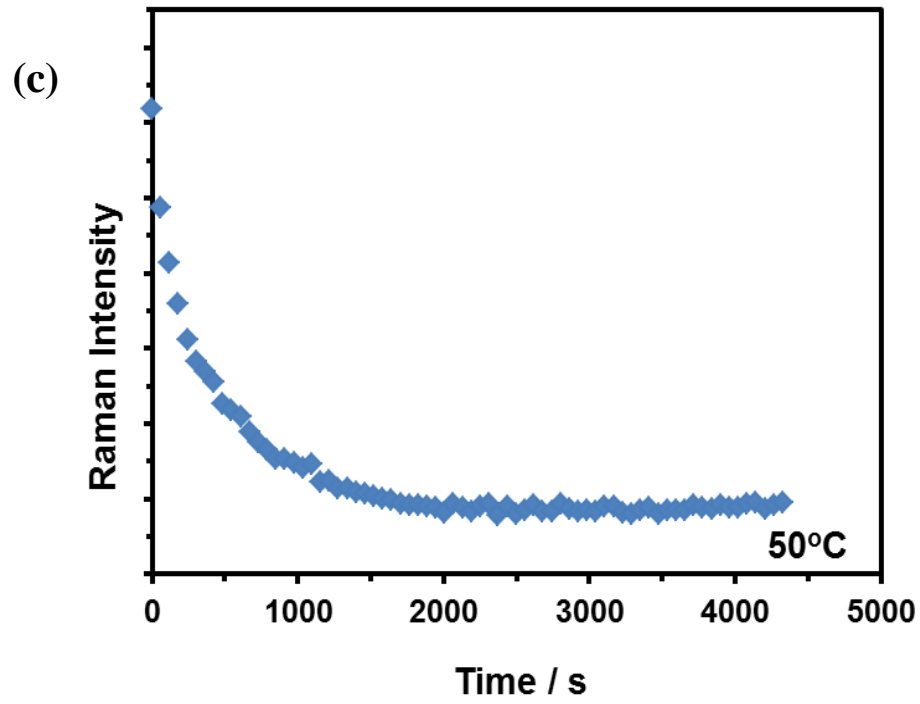
Figures A-2. Integrated Raman intensities of TATP band at 940 cm^{-1} : (a) 30°C ; (b) 40°C (c) 50°C ; (d) 60°C .



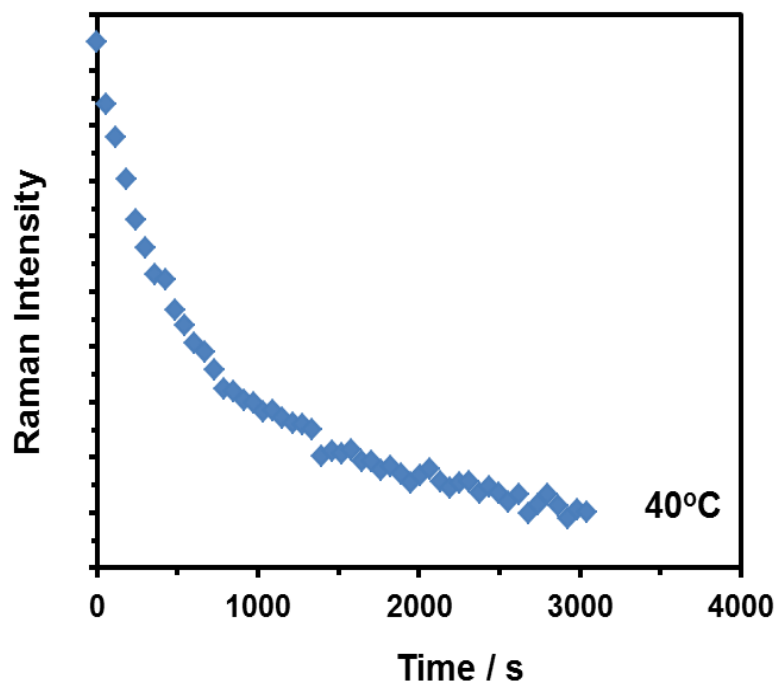
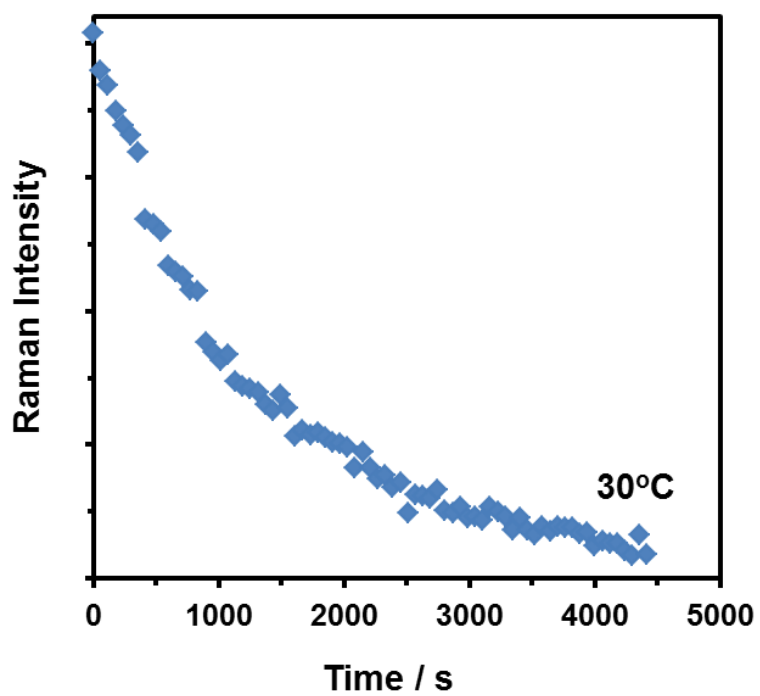


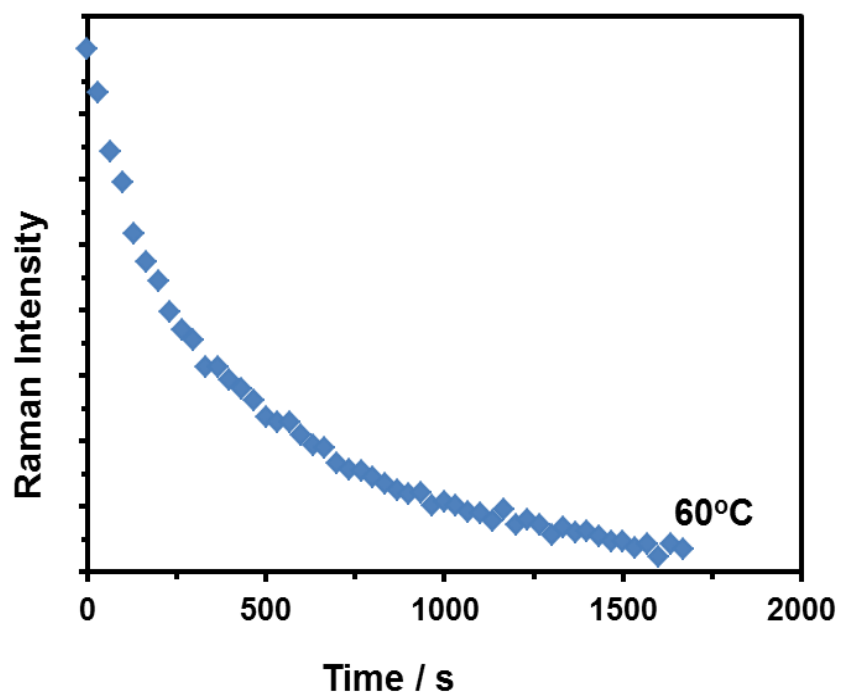
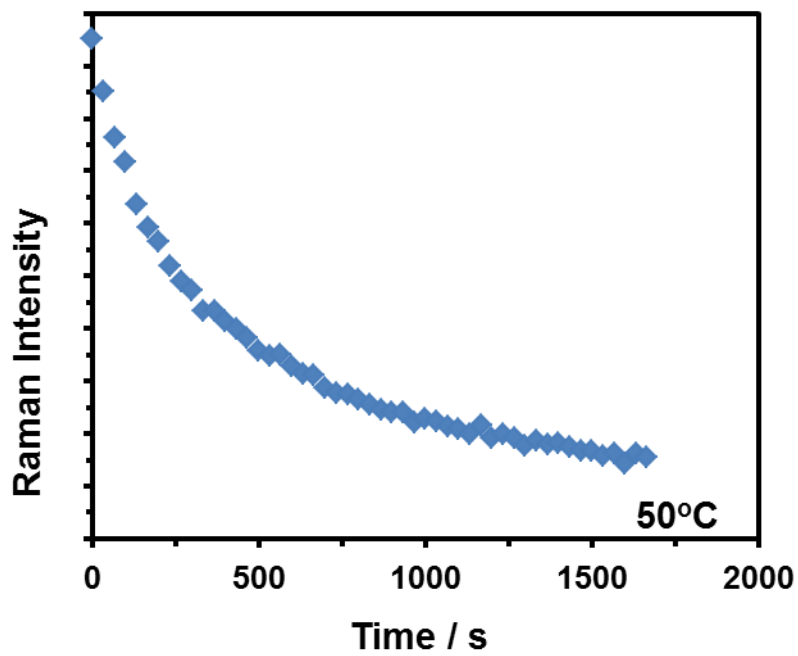
Figures A-3. Examples of first-order decay at several temperatures: (a) 30°C; (b) 40°C (c) 50°C; (d) 60°C.





Figures A-4. Examples of second-order decay at various temperatures.





Figures A-4. Arrhenius plots to determine the activation energies of: (a) first and (b) second step of proposed mechanism. The propagated errors of the activation energies were calculated taking account the errors of the ANOVA tests of the regressions.

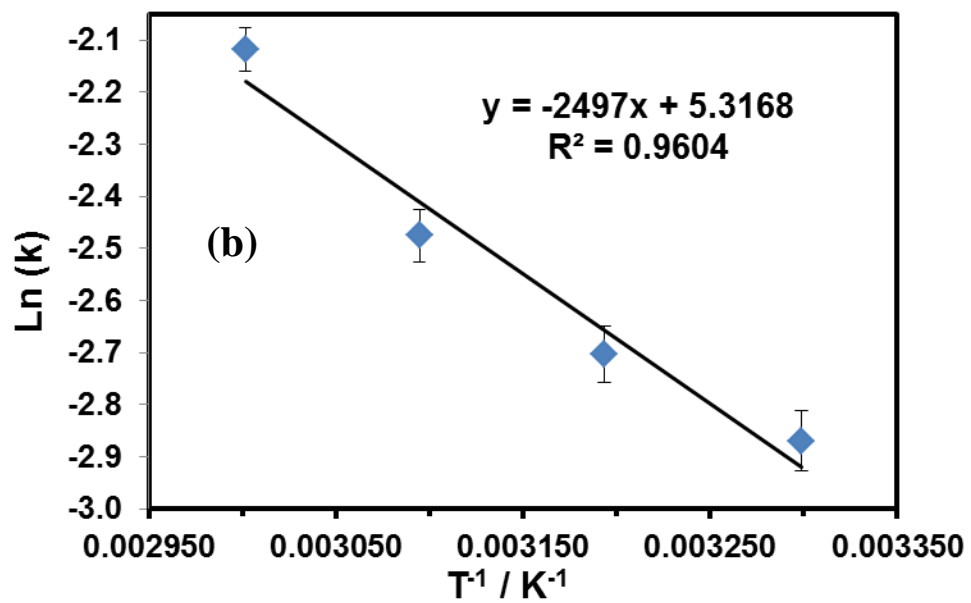
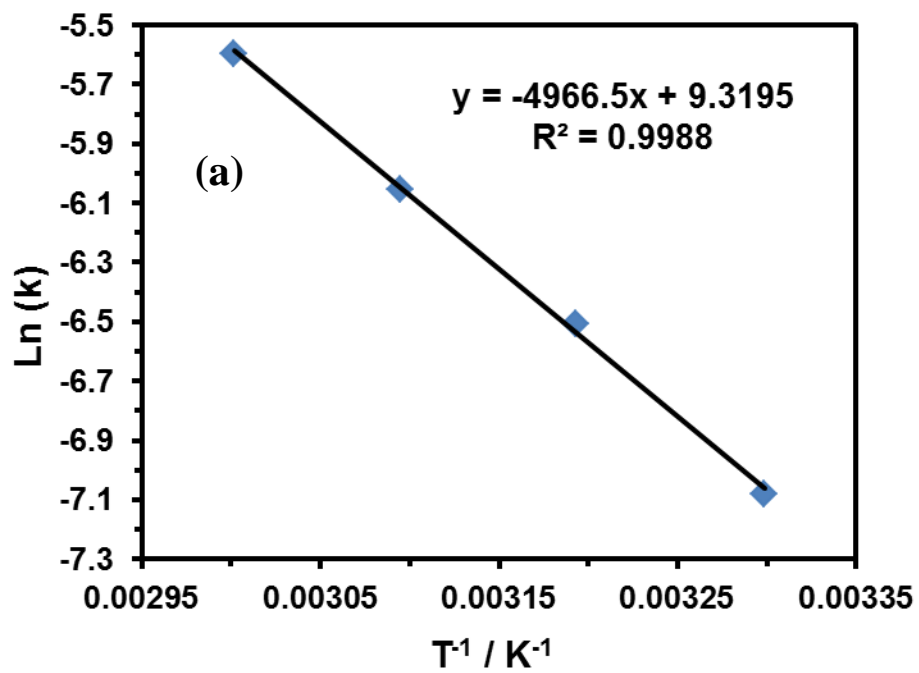


Table A-1. Tentative band assignments for theoretically calculated Raman spectra for acetone and P1 monomer.

Acetone			P1 Monomer		
Band	DFT/cm ⁻¹	Exp./cm ⁻¹	Band	DFT/cm ⁻¹	Exp./cm ⁻¹
α_{C-C-C}	380	384	α_{C-C-O}	382	412
δ_{C-C-C}	488	485	α_{O-C-O}	510	554
$\alpha_{C-C=O}$	531	528	ω_{C-C-C}	582	574
$\nu_s C-C-C$	789	789	$\nu_s C-C + \nu_s O-C$	772	777
$\delta_{CH_3} + \nu_{as} C-C-C$	885	893	$\nu_s C-C + \nu_{as} O-C$	842	800
$\delta_{CH_3} + \delta_{C-C-C}$	1070	1065	ν_{O-O}	920	880
$\omega_{CH_3} + \nu_{as} C-C-C$	1231	1221	$\delta_{CH_3} + \nu_{as} C-C-C$	937	----
$\alpha_{CH_3} + \gamma_{C-C-C}$	1431	1421	$\nu_{O-C} + \nu_s C-C-C$	975	939
$\nu_{C=O}$	1776	1709	$\nu_{as} C-C-C + \alpha_{C-O-H}$	1114	1069
			$\nu_{as} O-C-O + \delta_{C-C-C}$	1192	1250
			$\omega_{CH_3} + \nu_s C-C-C$	1236	1231
			$\alpha_{C-O-H} + \alpha_{O-O-H}$	1355	1346
			$\alpha_{C-O-H} + \alpha_{O-O-}$	1375	---
			γ_{CH_3}	1481	1419
			α_{CH_3}	1496	1447

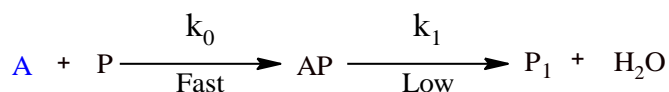
Table A-2. Rate constants at several temperatures: (a) first order decay; (b) second order decay.

First order decay							
T(°C)	k ₁			k ₁ (average)	Δk ₁	1/T(K)	Ln(k ₁)
30	0.00088144	0.00080300	0.00083431	0.00083958	0.00003948	0.003299	-7.08261
40	0.00158581	0.00125000	0.00163629	0.00149070	0.00020997	0.003193	-6.50851
50	0.00249633	0.00157300	0.00298150	0.00235028	0.00071552	0.003095	-6.05322
60	0.00345549	0.00370270	0.00397215	0.00371011	0.00025841	0.003002	-5.59669

Second order decay							
T(°C)	k ₂			k ₂ (average)	Δk ₂	1/T(K)	Ln(k ₂)
30	0.05479826	0.05814326	0.05714326	0.05669493	0.00171698	0.003299	-2.87007
40	0.06509754	0.06844354	0.06744354	0.06699487	0.00171753	0.003193	-2.70314
50	0.08256065	0.08590765	0.08390765	0.08412532	0.00168408	0.003095	-2.47545
60	0.11878642	0.12213442	0.12013442	0.12035175	0.00168455	0.003002	-2.11734

Mathematical details of the TATP kinetic expression

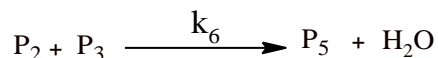
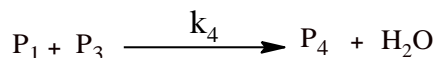
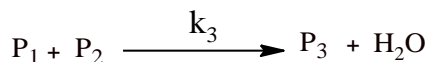
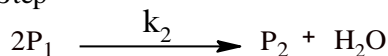
Monomer Formation Step



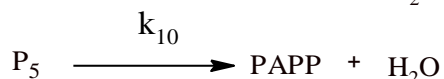
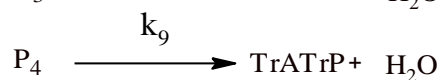
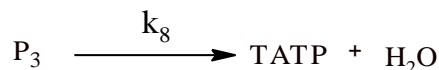
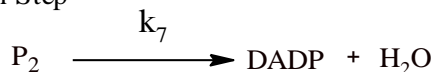
P (Hydrogen peroxide)

A (acetone)

Polymerization Step



Cyclization Step



$$\frac{d[P_1]}{dt} = k_1[AP] - 2k_2[P_1]^2 - k_3[P_1][P_2] - k_4[P_1][P_3]$$

$$\frac{d[P_2]}{dt} = k_2[P_1]^2 - k_3[P_1][P_2] - 2k_5[P_2]^2 - k_6[P_2][P_3] - k_7[P_2]$$

$$\frac{d[P_3]}{dt} = k_3[P_1][P_2] - k_4[P_1][P_3] - k_6[P_2][P_3] - k_8[P_3]$$

$$\frac{d[P_4]}{dt} = k_4[P_1][P_3] + 2k_5[P_2]^2 - k_9[P_4]$$

$$\frac{d[P_5]}{dt} = k_6[P_2][P_3] - k_{10}[P_5]$$

Considering the TATP rate as the rate determining step (RDS) and the structures P₁, P₂, P₃, P₄ and P₅ as intermediates.

$$\frac{d[TATP]}{dt} = k_8[P_3]$$

$$1. k_1[AP] - 2k_2[P_1]^2 - k_3[P_1][P_2] - k_4[P_1][P_3] = 0$$

$$2. k_2[P_1]^2 - k_3[P_1][P_2] - 2k_5[P_2]^2 - k_6[P_2][P_3] - k_7[P_2] = 0$$

$$3. k_3[P_1][P_2] - k_4[P_1][P_3] - k_6[P_2][P_3] - k_8[P_3] = 0$$

$$4. k_4[P_1][P_3] + 2k_5[P_2]^2 - k_9[P_4] = 0$$

$$5. k_6[P_2][P_3] - k_{10}[P_5] = 0$$

Considering the experimental fact that TATP is the major product (over 90% purity), the other terms of the cyclizations are close to zero; consequently the term $k_6[P_2][P_3]$ also reduces to zero.

With this approach the five-equation system is reduced to a four-equation one.

$$6. k_1[AP] - 2k_2[P_1]^2 - k_3[P_1][P_2] - k_4[P_1][P_3] = 0$$

$$7. 2k_2[P_1]^2 - k_3[P_1][P_2] - 2k_5[P_2]^2 = 0$$

$$8. k_3[P_1][P_2] - k_4[P_1][P_3] - k_8[P_3] = 0$$

$$9. k_4[P_1][P_3] + 2k_5[P_2]^2 = 0$$

Using this equality $k_4[P_1][P_3] = k_5[P_2]^2$ From equation 9, we get the following three-equation system:

$$10. k_1[AP] - 2k_2[P_1]^2 - k_3[P_1][P_2] + 2k_5[P_2]^2 = 0$$

$$11. 2k_2[P_1]^2 - k_3[P_1][P_2] - 2k_5[P_2]^2 = 0$$

$$12. k_3[P_1][P_2] + 2k_5[P_2]^2 - k_8[P_3] = 0$$

Reducing the equations 11 and 12:

$$13. k_1[AP] - 2k_3[P_1][P_2] = 0$$

$$13. k_1[AP] = 2k_3[P_1][P_2]$$

Replacing the above equality in the equation 12, we get:

$$14. k_1[AP] - 2k_5[P_2]^2 - k_8[P_3] = 0$$

Finally, considering the dimmer dimerization ($2k_5[P_2]^2$) with lowest probability than monomer and TATP formation process, we get:

$$[P_3] = \frac{k_1}{k_8} AP$$

Replacing the $[P_3]$ expression and having into account this experimental fact (monitored with the decay of the vibrational band $\square_{C=O...H}$): $[AP] = [AP_0]e^{-k_1 t}$, finally integrating the resulting expression, we obtain:

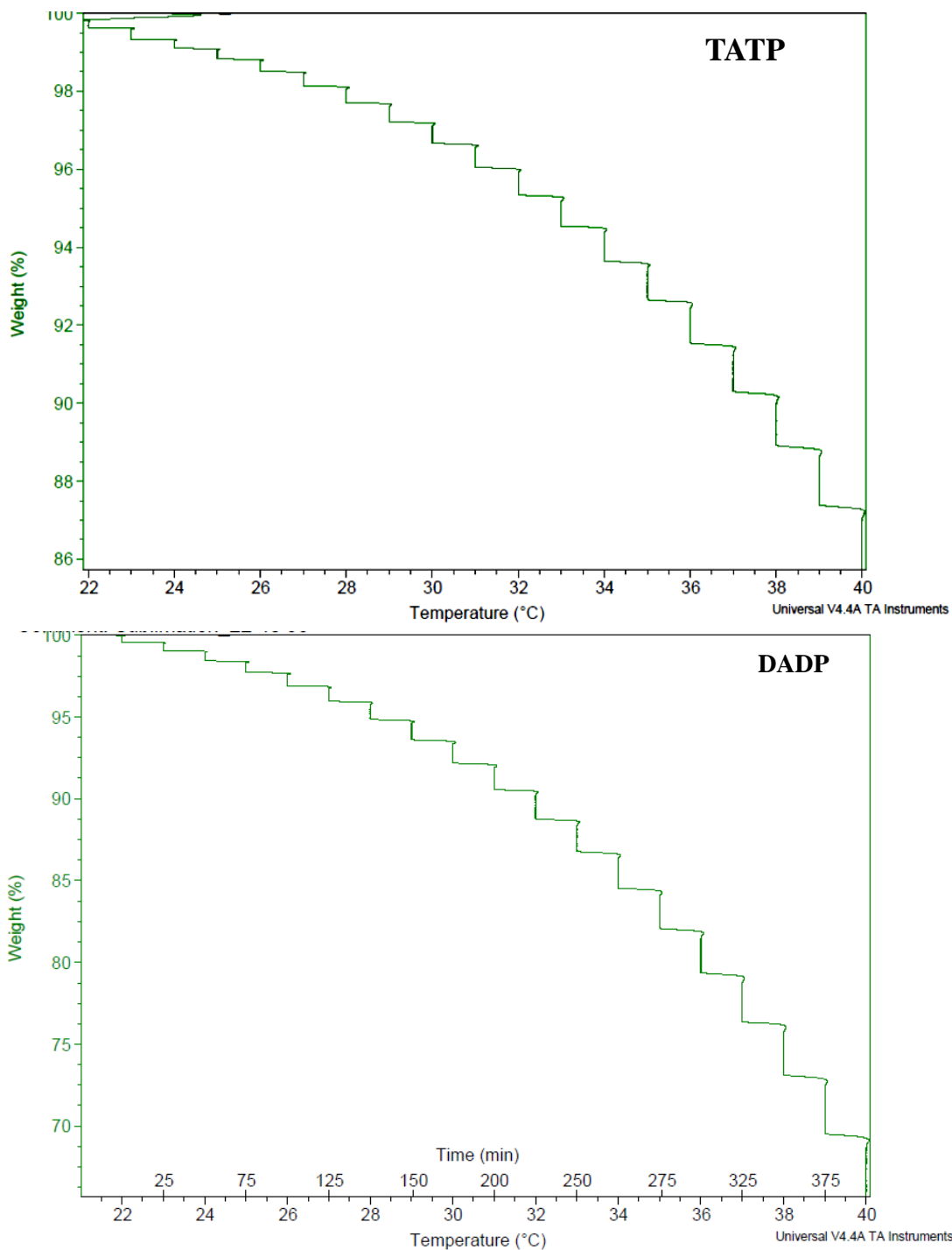
$$\int_{[TATP]_0}^{[TATP]_t} d[TATP] = \int_0^t -\frac{k_1}{k_8} AP_0 e^{-2k_1 t} dt$$

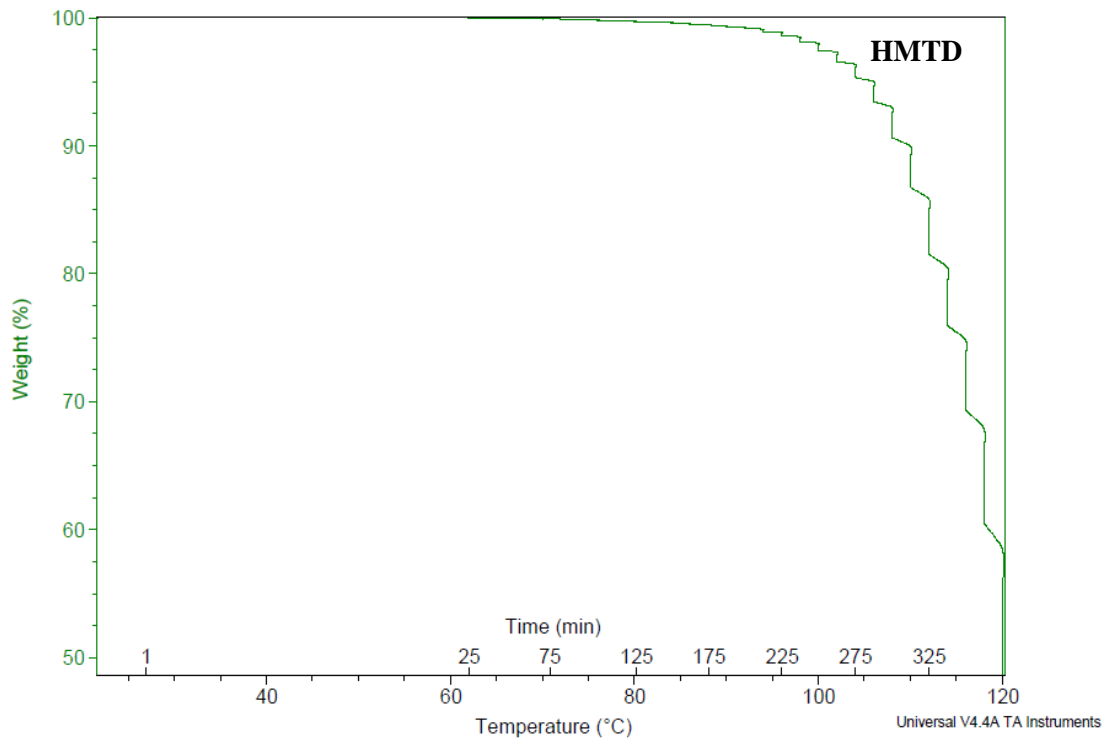
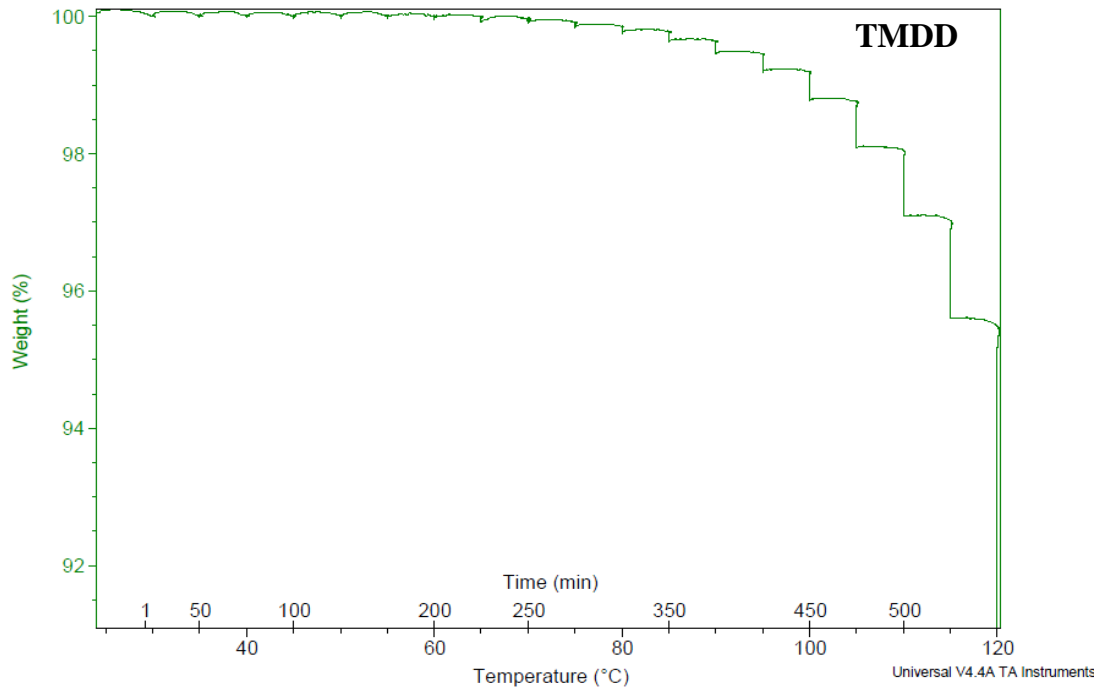
$$[TATP] = \frac{1}{2k_8} AP_0 - \frac{1}{2k_8} AP_0 e^{-2k_1 t}$$

APPENDIX-B

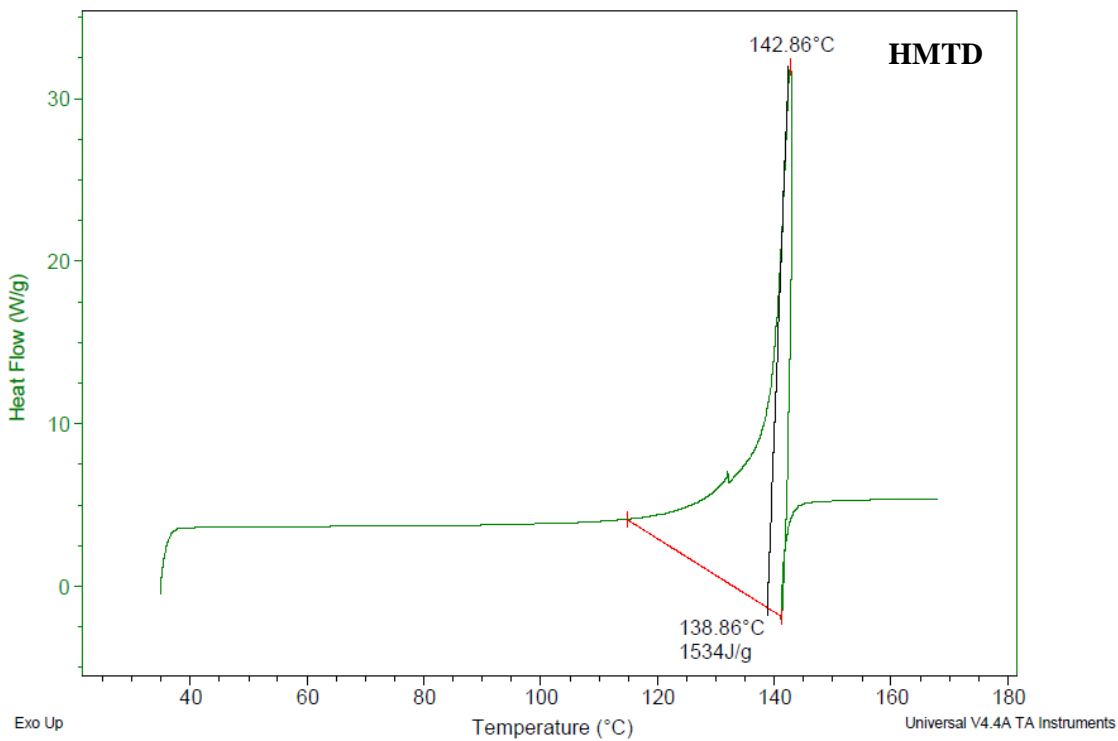
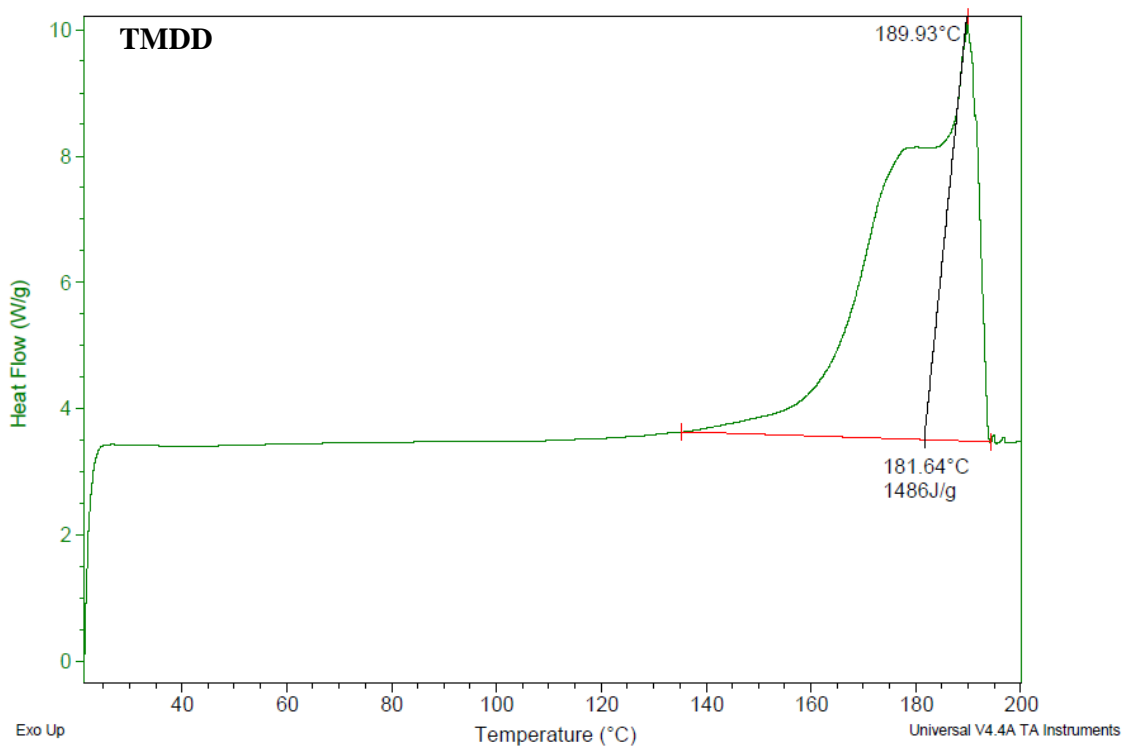
Thermal Profile of Homemade Peroxide Explosives

Figures B-1. View of a TGA-thermogram of the different homemade explosives in the TGA Q500 software. Each vertical line corresponds to an isothermal weight loss.





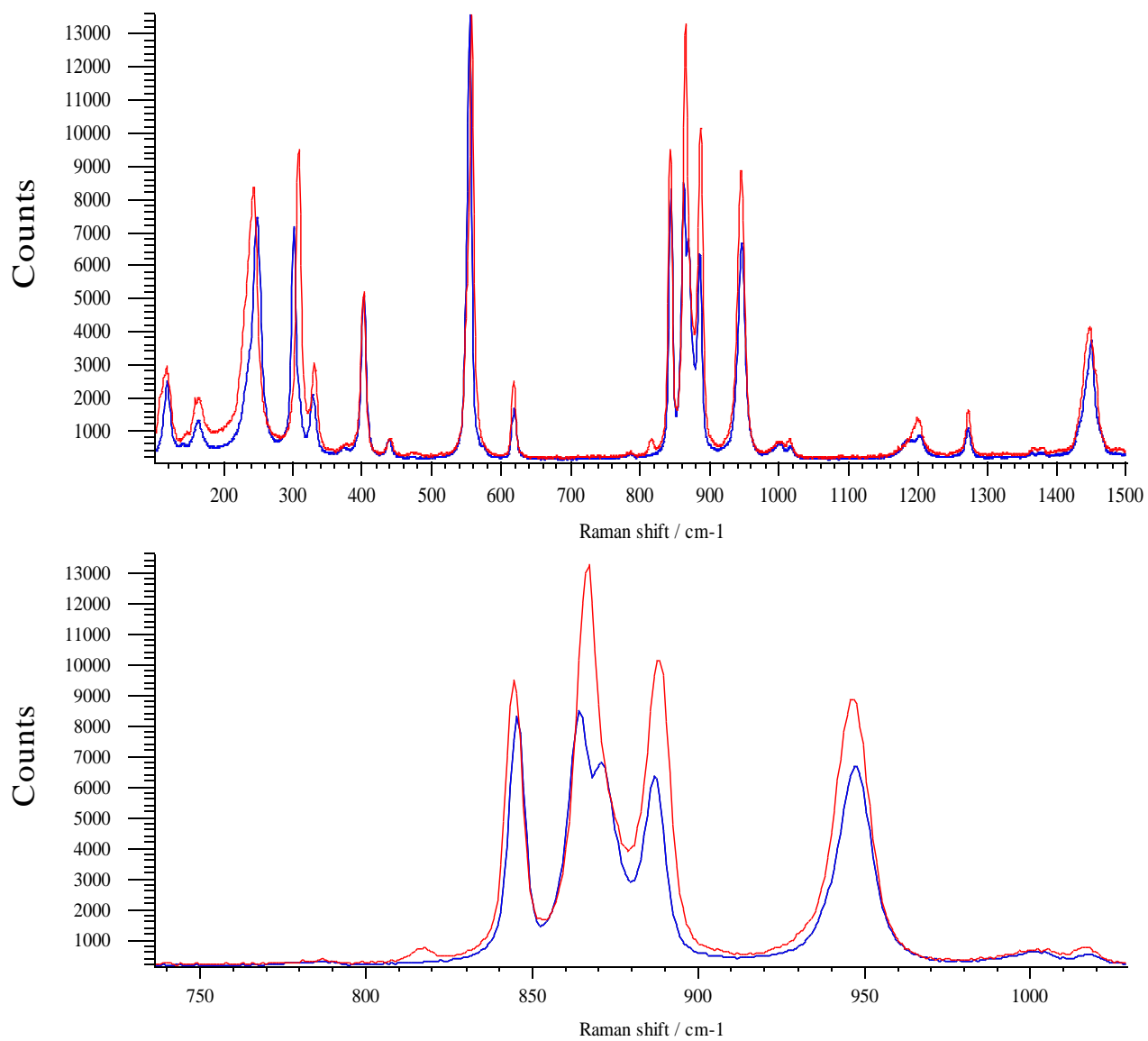
Figures B-2. View of a DSC-thermogram of the different homemade explosives in the DSC Q10 software.



APPENDIX-C

Spectroscopic and Physical Evidence of Isolated D₃-TATP and C₂-TATP Conformers

Figures C-1. View of a Raman spectrum of the Renishaw spectrometer software at different spectral ranges.



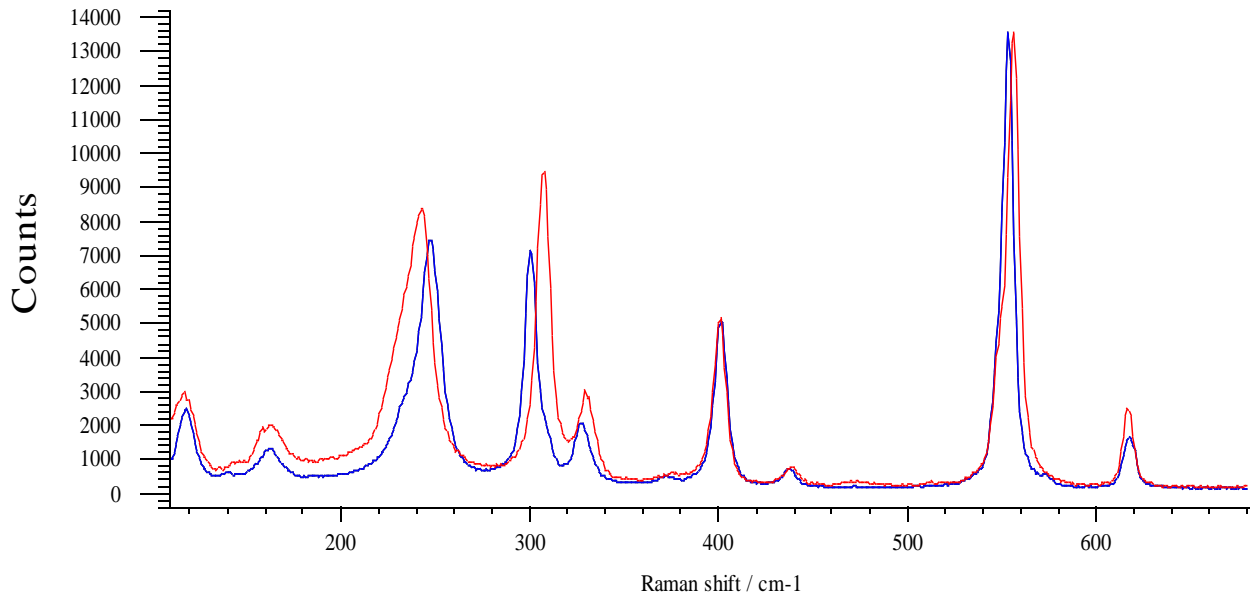
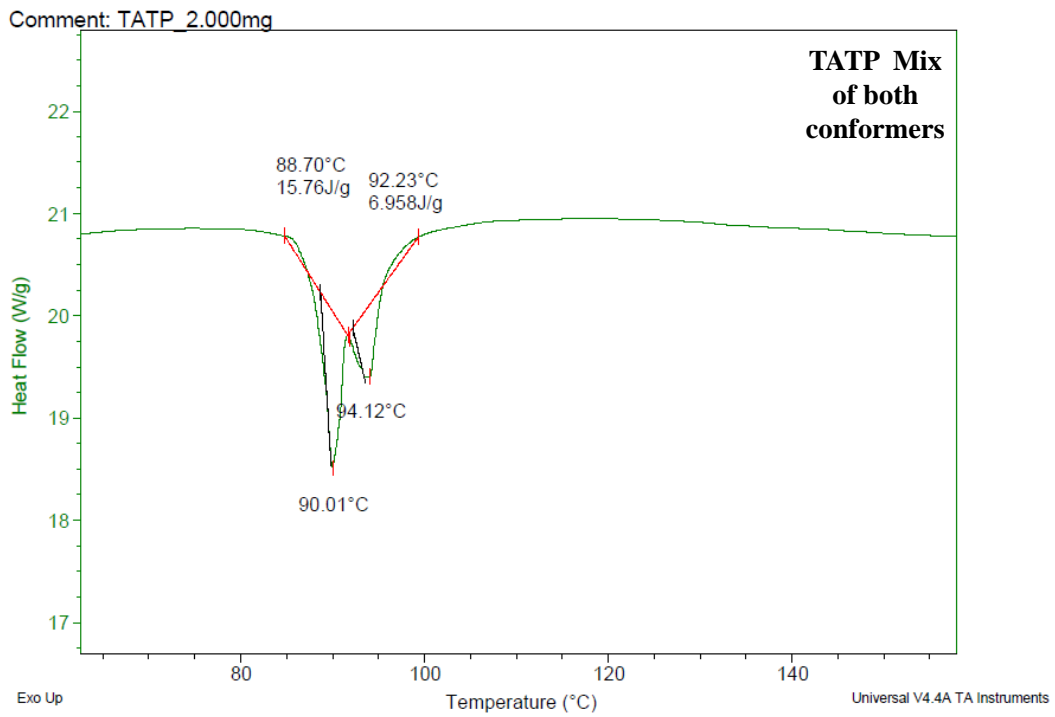
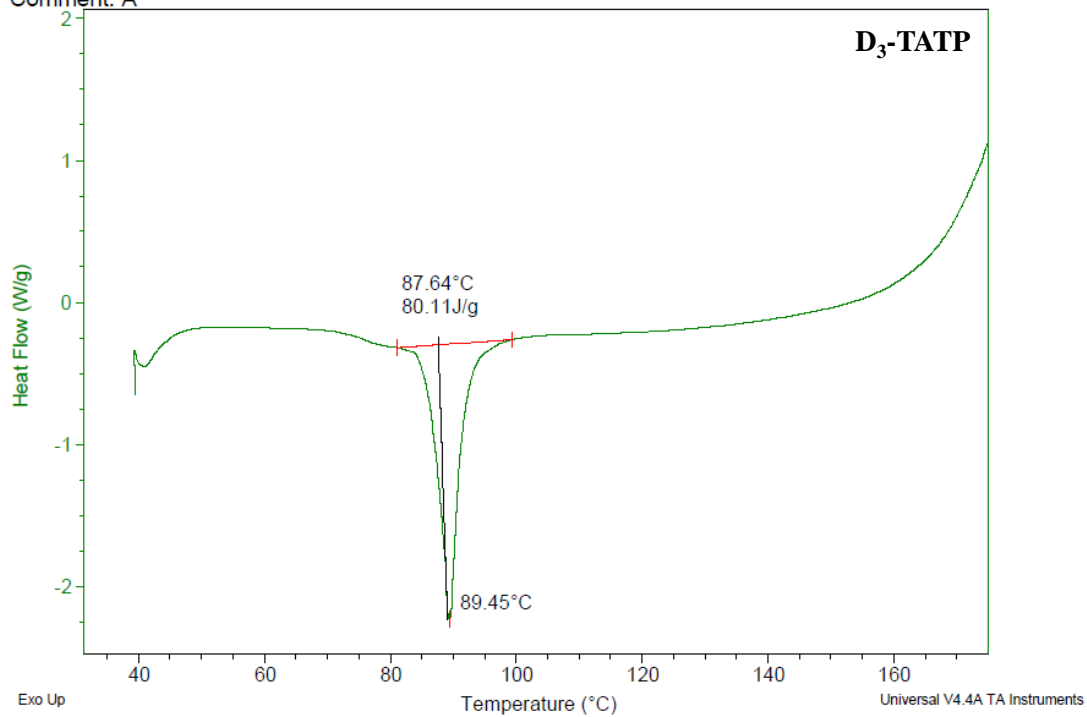


Figure C-2. View a DSC-thermogram of TATP conformers of the DSC Q10 software



Comment: A



Comment: From CH₂Cl₂

